

# Regularised B-splines projected Gaussian Process priors to estimate the age profile of COVID-19 deaths before and after vaccine roll-out

Mérodie Monod<sup>†,§,\*</sup>, Alexandra Blenkinsop<sup>§</sup>, Andrea Brizzi<sup>§</sup>, Yu Chen<sup>§</sup>, Vidoushee Jogarah<sup>§</sup>, Yuanrong Wang<sup>§</sup>, Seth Flaxman<sup>‡,||</sup>, Samir Bhatt<sup>‡,||</sup> and Oliver Ratmann<sup>‡,§,\*</sup>

**Abstract.** The COVID-19 pandemic has caused severe public health consequences in the United States. The United States began a vaccination campaign at the end of 2020 targeting primarily elderly residents before extending access to younger individuals. With both COVID-19 infection fatality ratios and vaccine uptake being heterogeneous across ages, an important consideration is whether the age contribution to deaths shifted over time towards younger age groups. In this study, we use a Bayesian non-parametric spatial approach to estimate the age-specific contribution to COVID-19 attributable deaths over time. The proposed spatial approach is a low-rank Gaussian Process projected by regularised B-splines. Simulation analyses and benchmark results show that the spatial approach performs better than a standard B-splines approach and equivalently well as a standard Gaussian Process, for considerably lower runtimes. We find that COVID-19 has been especially deadly in the United States. The mortality rates among individuals aged 85+ ranged from 1% to 5% across the US states. Since the beginning of the vaccination campaign, the number of weekly deaths reduced in every US state with a faster decrease among individuals aged 75+ than individuals aged 0 – 74. Simultaneously to this reduction, the contribution of individuals age 75+ to deaths decreased, with important disparities in the timing and rapidity of this decrease across the country.

**MSC2020 subject classifications:** Primary 62F15, 60G15, 65D07; secondary 62P10.

**Keywords:** Bayesian Inference, Gaussian Processes, Splines, Non-parametric estimation, COVID-19.

---

\*Corresponding authors [melodie.monod18@imperial.ac.uk](mailto:melodie.monod18@imperial.ac.uk) [oliver.ratmann@imperial.ac.uk](mailto:oliver.ratmann@imperial.ac.uk)

<sup>†</sup>First supporter of the project

<sup>‡</sup>Second supporter of the project

<sup>§</sup>Department of Mathematics, Imperial College London

<sup>¶</sup>MRC Centre for Global Infectious Disease Analysis; and the Abdul Latif Jameel Institute for Disease and Emergency Analytics (J-IDEA), School of Public Health, Imperial College London

<sup>||</sup>Section of Epidemiology, Department of Public Health, University of Copenhagen

# 1 Introduction

A new pathogen, Severe Acute Respiratory Syndrome Coronavirus 2 (SARS-CoV-2), emerged in the Wuhan region of China in December 2019 and subsequently spread worldwide. The resulting disease has been named COVID-19. COVID-19 is severe, with overall infection fatality rates (IFRs) between 0.5% and 1% ([Meyerowitz-Katz and Merone, 2020](#); [Brazeau et al., 2020](#)), which increase exponentially with age ([Levin et al., 2020](#)), similar to other pathogens such as pandemic influenza ([Baguelin et al., 2013](#)). As a result, available vaccine doses are currently being prioritised to older age groups and the progress in improving health outcomes can thus be measured directly in terms of declining trends in COVID-19 attributable deaths, especially among older age groups.

Here, we present a fully Bayesian, computationally scalable approach for estimating the age composition of COVID-19 attributable deaths from partially observed data, as well as longitudinal trends in the age composition of COVID-19 attributable deaths. The primary aim of the method is to document shifts in the age composition of deaths since vaccine rollout, which began in the US on December 14, 2020, and to identify geographic areas in which these shifts are occurring faster or slower than expected relative to vaccine coverage. Further, we provide estimates into the cumulative loss of life due to COVID-19, stratified by age. Finally, it has been suggested that COVID-19 transmission dynamics may have shifted over time to younger age groups, which should result in fewer deaths in older age groups ([Cortis, 2020](#); [Boehmer et al., 2020](#)), and we here aim to identify such longitudinal signal prior to vaccine rollout in the death data. This is an important consideration, since testing strategies and testing uptake changed over time, and so it is unclear how to interpret observed changes in the age profile of reported cases. We illustrate our approach to addressing these objectives on publicly available, age-specific COVID-19 death data from 50 US states that are reported by the Centers for Disease Control and Prevention (CDC) ([2021c](#)).

Our model estimates a two-dimensional (2D) surface over ages and weeks to define the age-specific contribution to deaths over time. To impute missing entries on the surface and estimate global trends over ages and weeks, we borrow information across neighboring entries by using a non-parametric smoothing method. A natural starting point for modelling a surface is a 2D Gaussian process (GP) ([Rasmussen and Williams, 2005](#)). However, their computational complexity makes the use of 2D GPs in a fully Bayesian framework difficult when the surface dimension becomes large, even after using a Kronecker decomposition of the kernel function ([Saatçi, 2011](#); [Wilson et al., 2014](#)). Here we adopt a low-rank approximation via a tensor product of B-splines for which the parameters follow a 2D GP. The resulting approach is equivalent to a 2D GP defined by a low-rank covariance matrix projected by B-splines. B-splines are a popular choice for non-parametric modelling, due to their continuity properties, ensuring smoothness of the fitted surface, and their easy implementation. But choosing the optimal number and position of knots—the defining grid segments where the surface is expected to change its behavior—on the space of ages and weeks is a complex task. Some approaches have focused on adding a penalty to restrict the flexibility of the fitted surface ([O’Sullivan, 1986,9](#); [Eilers and Marx, 1996](#); [Eilers et al., 2006](#)). Here, we regularise the fitted surface

by defining the GP prior on the B-splines tensor product’s parameters by a kernel function with a free complexity parameter. We compare the penalty induced by this choice to that of related regularisation methods. Furthermore, we show how our approach results in computational gains over a standard 2D GP for similar estimation accuracy.

Considering the CDC data set, additional complications arise because available data (1) are censored in the sense that cumulative deaths are not reported if the cumulative deaths are between 1 and 9, (2) suffer from reporting delays and (3) are thought to be under-reported in direct comparison to excess deaths (Islam et al., 2021). Considering (1), we derive and include bounds on the cumulative deaths corresponding to censored data in the likelihood. Considering (2) and (3), we explicitly allow for a rescaling of the sum of deaths across age groups in the model according to other data sets, such as the Johns Hopkins University (JHU) COVID-19 death trajectories (John Hopkins University of Medicine, 2020), or all-age excess deaths.

This paper is structured as follows. Section 2 introduces the data and their limitations. Section 3 describes the proposed methodology to model trends in the age-composition of COVID-19 deaths. Section 4 presents a comparison of the proposed method to related estimation approaches on simulated data and Section 5 on real world data used for benchmarking. Section 6 characterises the trends of the age-specific contribution to COVID-19 deaths over time across the United States. We estimate age-specific mortality trends, examine the heterogeneity in the age composition of COVID-19 attributable deaths across states, and characterize time trends in the age profile of COVID-19 attributable deaths since vaccination roll-out. Lastly, Section 7 closes with a discussion. The code to use our methods and to reproduce our results is available at <https://github.com/melodiemonod/covid19Vaccination>.

## 2 COVID-19 deaths and vaccination data

The Center for Disease Control (CDC) and National Center for Health Statistics (NCHS) report each week on the total number of deaths involving COVID-19 that have been received and tabulated through the National Vital Statistics database (Centers for Disease Control and Prevention, 2021c) for every US state  $m$  across the age groups

$$\mathcal{B} = \left\{ [0 - 0], [1 - 4], [5 - 14], [15 - 24], [25 - 34], [35 - 44], [45 - 54], \right. \\ \left. [55 - 64], [65 - 74], [75 - 84], [85+] \right\}, \quad (2.1)$$

which we refer to as cumulative reported COVID-19 attributable deaths,  $D_{m,b,w}$ , for state  $m$ , on week  $w$  and in age group  $b$ . To simplify the longitudinal dependence and create a stationary time series from the cumulative counts (King et al., 2015), we use historical records from Rearc (2021) and obtain the weekly COVID-19 attributable deaths by first differencing,

$$d_{m,b,w} = D_{m,b,w+1} - D_{m,b,w}, \quad (2.2)$$

in each location and age group for all but the last available week (daily deaths,  $d$ , for state  $m$ , on week  $w$  and in age group  $b$ ). We index the weekly deaths by  $w = 1, \dots, W$ , and for simplicity we suppress the state index in what follows, with all equations being analogous. Reflecting the reporting nature of the age-stratified CDC data, the weekly COVID-19 attributable  $d_{m,b,w}$  are subject to reporting delays and do not necessarily correspond to the number of individuals who died of COVID-19 in week  $w$ .

The CDC does not report the cumulative deaths count if the count is between 1 and 9. Thus, it is not possible to retrieve all weekly deaths  $d_{b,w}$ , and we refer to the set of weeks that are retrievable for age group  $b$  through first order differencing by  $\mathcal{W}_b^{\text{WR}}$ , and to the set of weeks that were non-retrievable because of censoring by  $\mathcal{W}_b^{\text{WNR}}$ . The censored cumulative deaths are bounded, such that the sum of non-retrievable weekly deaths is also bounded. The exact computations are described in Appendix S2.1. In addition, there was no update on July 4, 2020 resulting in missing cumulative deaths in that week. The weekly deaths of that week and the preceding week are missing. Note that the missing weekly deaths are not equivalent to the non-retrievable weekly deaths because we cannot bound their sums. Here, we analyze data reported from May 2, 2020 to May 15, 2021, shown in Figure 1. In Figure 1, a colored entry indicates retrievable weekly deaths, a grey entry indicates non-retrievable weekly deaths and an orange entry indicates missing weekly deaths. We thus have  $W = 54$ .

We use four additional data sets. Firstly, we retrieved the weekly COVID-19 attributable deaths regardless of age from John Hopkins University (JHU) for all US states from May 2, 2020 to May 15, 2021 (John Hopkins University of Medicine, 2020), which we denote by  $d_{m,w}^{\text{JHU}}$  for state  $m$  and week  $w$ . In these data, reporting-delayed deaths are back-distributed where possible, and for this reason we use the overall deaths as a reference to mitigate the reporting delays in the age-stratified CDC data (2.2). Secondly, age-specific weekly COVID-19 attributable deaths are also directly reported by state Departments of Health (DoH) on their websites, or data repositories. For 42 US states, data records are available up to April 1, 2021 at <https://github.com/ImperialCollegeLondon/US-covid19-agespecific-mortality-data>. In most cases the DoH data corresponds well to JHU data, prompting us to use the DoH data to assess the accuracy in our model estimates based on the CDC data for the same 42 states and the same time period. Thirdly, the CDC reports the proportion of state populations vaccinated with at least one dose (Centers for Disease Control and Prevention, 2021a), and we use historic records available at <https://github.com/owid/covid-19-data/tree/master/public/data/vaccinations> to assess vaccination coverage in each US state. Lastly, pre-pandemic age-specific population counts were drawn from the U.S. Census Bureau in 2018 (United States Census Bureau, 2018).

### 3 Methods

#### 3.1 Modelling weekly COVID-19 attributable deaths by age

Our aim is to estimate the weekly deaths by 1-year age bands,  $a \in \mathcal{A} = \{0, 1, \dots, 104, 105\}$  in week  $w \in \mathcal{W} = \{1, \dots, W\}$ , and we denote their expectation



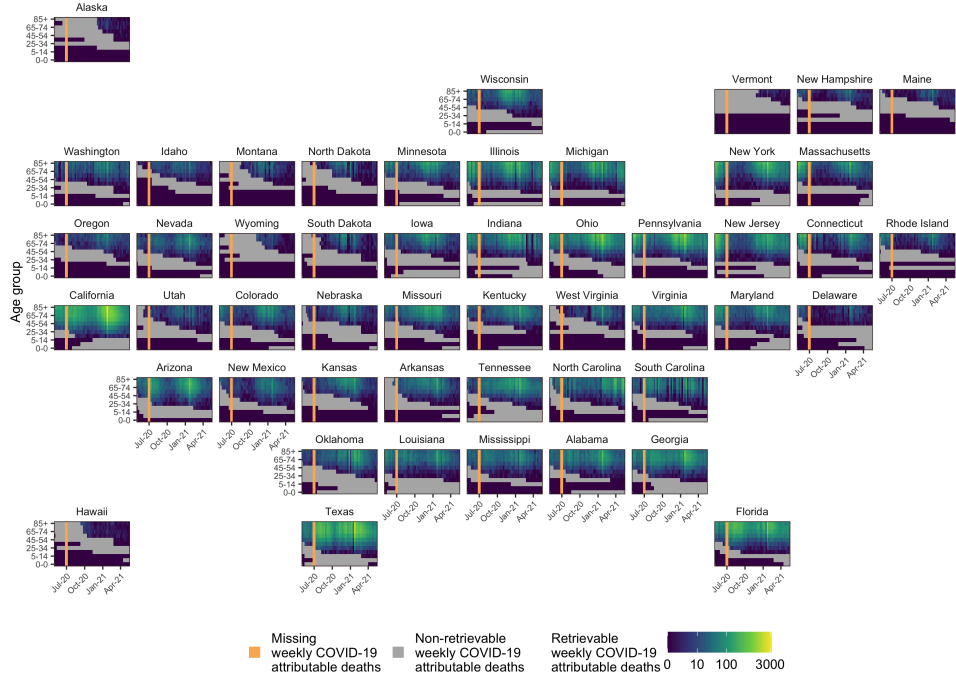


Figure 1: **Retrievable weekly COVID-19 attributable deaths in the United States.** The retrievable weekly deaths are computed using the first order difference of reported cumulative deaths by the CDC ([Centers for Disease Control and Prevention, 2021c](#)). Grey cells indicate non-retrievable weekly death counts due to the censoring of cumulative deaths. Orange bars show the missing weekly deaths due to non-reported cumulative deaths.

by  $\mu_{a,w}$ . We first decompose  $\mu_{a,w}$  as the product of the weekly deaths for all ages  $\lambda_w$  with the relative contribution  $\pi_{a,w}$  of age  $a$  to weekly deaths, where  $\sum_a \pi_{a,w} = 1$  for all  $w$ . Second, we model the longitudinal age composition of deaths  $\pi_{a,w}$  as a bivariate random function  $(a, w) \rightarrow f(a, w) \in \mathbb{R}$ , that is exponentiated, normalised, and evaluated on the 2D grid  $\mathcal{A} \times \mathcal{W}$ . Our basic latent model structure is thus

$$\mu_{a,w} = \lambda_w \pi_{a,w} \quad (3.1a)$$

$$\pi_{a,w} = \text{softmax}([f(a, w)]_{a \in \mathcal{A}}) \quad (3.1b)$$

$$= \left( \frac{\exp f(a, w)}{\sum_{\tilde{a} \in \mathcal{A}} \exp f(\tilde{a}, w)} \right). \quad (3.1c)$$

To link the expected weekly deaths by 1-year age band,  $\mu_{a,w}$ , to the data (2.2), we aggregate them over the age groups specified by the CDC,  $\mu_{b,w} = \sum_{a \in b} \mu_{a,w}$ , for all  $b \in \mathcal{B}$ . Then, we model the observed, retrievable weekly deaths in age  $b$  and week

$w$  for all ages and weeks through Negative Binomial distributions in the shape-scale parameterisation,

$$d_{b,w} \mid \alpha_{b,w}, \theta \sim \text{NegBin}(\alpha_{b,w}, \theta) \quad (3.2a)$$

$$\mu_{b,w} = \alpha_{b,w} \frac{\theta}{1 - \theta} \quad (3.2b)$$

$$\sigma_{b,w}^2 = \alpha_{b,w} \frac{\theta}{(1 - \theta)^2} = \mu_{b,w} (1 - \theta)^{-1} = \mu_{b,w} (1 + \nu), \quad (3.2c)$$

with mean  $\mu_{b,w}$  and variance  $\sigma_{b,w}^2$ , and where  $\nu > 0$  is interpreted as an overdispersion parameter. The purpose of the shape-scale parameterisation with identical  $\theta$  (3.2a) is that then, the weekly deaths conditional on their total follow a Dirichlet-Multinomial distribution with parameters  $\alpha_{b,w}$ , resulting in the succinct identity  $\alpha_{b,w} = \sum_{a \in \mathcal{B}} \alpha_{a,w}$  (Townes, 2020). For implementation, notice that the shape and scale parameters can be rewritten as  $\alpha_{b,w} = \mu_{b,w}/\nu$  and  $\theta = \nu/(1 + \nu)$ .

Our Bayesian model comprises as log likelihood the sum of the log Negative Binomial densities (3.2a) over retrievable weekly deaths parameterised by  $\mu_{b,w}$  and  $\nu$ , and similar terms involving log cumulative density functions of the Negative Binomial that bound sums of the non-retrievable weekly deaths. We further place a default Exponential prior on the overdispersion parameter and an informative prior on  $\lambda_w$  that we discuss below. Our specification is completed with a prior on the random function  $f(a, w)$  specified by hyperparameters  $\phi$ , which we investigate in detail in the next section. Taken together, for the collection of weekly deaths  $\mathbf{d} = (d_{b,w}, b \in \mathcal{B}, w \in \{\mathcal{W}_b^{\text{WR}}, \mathcal{W}_b^{\text{WNR}}\})$ , our log posterior density is

$$\log p(\boldsymbol{\lambda}, \nu, \mathbf{f}, \phi \mid \mathbf{d}) \propto \sum_{b \in \mathcal{B}, w \in \mathcal{W}_b^{\text{WR}}} \log \text{NegBin}(d_{b,w} ; \mu_{b,w}/\nu, \frac{\nu}{1 + \nu}) \quad (3.3a)$$

$$+ \sum_{b \in \mathcal{B}} \log p(\{d_{b,w}\}_{w \in \mathcal{W}_b^{\text{WNR}}} \mid \dots) \quad (3.3b)$$

$$+ \sum_{w \in \mathcal{W}} \log \text{Gamma}(\lambda_w ; T_w, T_w/(2\mathfrak{Q})) \quad (3.3c)$$

$$+ \log \text{Exponential}(\nu ; 1) + \log p(\mathbf{f} ; \phi) + \log p(\phi), \quad (3.3d)$$

where for brevity the terms  $p(\{d_{b,w}\}_{w \in \mathcal{W}_b^{\text{WNR}}} \mid \dots)$  in (3.3b) are detailed in Appendix S2.2. The prior on the total number of weekly deaths  $\lambda_w$ , in (3.3c), is specified in the mean-standard deviation parameterisation. The prior expectation on the total deaths is found by summing the retrievable deaths and adding 5 counts as “best-guess” for the non-retrievable ones, such that  $T_w = \sum_{b \in \mathcal{B}, w \in \mathcal{W}_b^{\text{WR}}} d_{b,w} + \sum_{b \in \mathcal{B}, w \in \mathcal{W}_b^{\text{WNR}}} 5$ . Next, we assume that the first order difference in the total deaths is 2 times a standard deviation. We find the empirical ratio of the total death relative to their first order difference  $\mathfrak{Q}$ , with a linear regression without intercept, and specify the standard deviation accordingly.

To mitigate reporting delays, we make use of external information, the overall, weekly COVID-19 attributable deaths reported by JHU that are where possible adjusted for

reporting delays. Specifically, we require that our posterior predictions of the COVID-19 attributable deaths in age group  $a$  and week  $w$ ,  $d_{aw}^*$ , sum to  $\sum_a d_{aw}^* = d_w^{\text{JHU}}$ . We achieve this by exploiting the probabilistic relationship between Negative Binomial distributions in the shape-scale parameterisation and the Dirichlet-Multinomial, through

$$p(d_{\cdot,w}^* \mid \mathbf{d}, d_w^{\text{JHU}}) = \int \text{DirMult}(d_{\cdot,w}^*; d_w^{\text{JHU}}, (\alpha_{a,w})_{a \in \mathcal{A}}) p(\boldsymbol{\lambda}, \nu, \mathbf{f}, \phi \mid \mathbf{d}) d(\boldsymbol{\lambda}, \nu, \mathbf{f}, \phi), \quad (3.4)$$

where as before  $\alpha_{a,w} = \mu_{a,w}/\nu = \lambda_w \text{softmax}(f(a, w))/\nu$ .

### 3.2 Modelling age-specific contributions to COVID-19 weekly deaths

In (3.1), we introduced a 2D function  $f(a, w)$ , for which we shall find a prior in this section. Let the number of points of the age axis be  $n = |\mathcal{A}|$  and on the week axis be  $m = |\mathcal{W}|$ . The total number of points on the grid is  $N = n \times m$ . The ensemble of pairs of points is  $\mathbf{X} = (\mathbf{x}^1, \dots, \mathbf{x}^N) = ((a^1, w^1), \dots, (a^n, w^m))$ . We now investigate different modelling approaches for the function  $f(a, w)$ .

#### Two-dimensional Gaussian Process

Given observations  $(\mathbf{X}, \mathbf{f}) = \{(\mathbf{x}^1, f(\mathbf{x}^1)), \dots, (\mathbf{x}^N, f(\mathbf{x}^N))\}$ , we define  $\mathbf{K} = \mathbf{K}(\mathbf{X}, \mathbf{X})$ , the covariance matrix evaluated at all pairs of points in  $\mathbf{X}$ .  $\mathbf{f}$  is a realization of a zero-mean 2D GP,

$$\mathbf{f} \mid \phi \sim \mathcal{GP}(\mathbf{0}, \mathbf{K}). \quad (3.5)$$

The covariance matrix has entries  $\mathbf{K}_{\mathbf{x}, \mathbf{x}'} = \text{Cov}(f(\mathbf{x}), f(\mathbf{x}')) = k(\mathbf{x}, \mathbf{x}')$  with  $\mathbf{x}, \mathbf{x}' \in \mathbf{X}$ , where  $k(\cdot, \cdot)$  is a kernel function depending on unknown hyperparameters  $\phi$ . For computational efficiency and because our output is on a multidimensional grid, we decompose the kernel function,

$$k((a, w), (a', w')) = k^1(a, a') k^2(w, w') \quad (3.6)$$

where  $k^1(\cdot, \cdot)$  and  $k^2(\cdot, \cdot)$  are kernel functions over ages and weeks, respectively. The corresponding covariance matrix  $\mathbf{K}$  is calculated with the Kronecker product  $\mathbf{K} = \mathbf{K}^2 \otimes \mathbf{K}^1$ , and the number of operations to evaluate the covariance matrix reduces from  $\mathcal{O}(N^3)$  to  $\mathcal{O}(2N^{3/2})$  (Gönen and Alpaydin, 2011; Saatçi, 2011). For implementation, we note that the order of the product follows from the fact that the matrix's entries are stacked columnwise, and rely on the efficient Kronecker product implementation via matrix-vector products proposed in the Supplementary Material, section 4 of Wilson et al. (2014).

### B-splines surface

B-splines<sup>1</sup> are constructed from polynomial pieces that are joined at certain values over the input space, called knots, and defined by a polynomial degree,  $d$ , and a non-decreasing sequence of knots,  $(t_1, t_2, \dots, t_K)$ , where  $K$  is the number of knots. Given those, the total number of B-splines is  $P = K + d - 1$ . We show how a B-spline is constructed in Appendix S3.1. In this paper, we use cubic B-splines, with  $d = 3$ , and denote by  $B_p(\cdot)$  the  $p$ th cubic B-spline. Moreover, we use equally spaced knots on both dimensions, such that the only tuning parameter is the number of knots. A fundamental property of B-splines, that constitutes most of their attractiveness, is that they are smooth. More rigorously, a cubic B-spline defined on strictly increasing knots is piecewise infinitely differentiable between the knots, and of continuity  $C^2$  on the knots (Goldman (2002), chap. 7).  $\mathbf{f}$  can be modelled with a tensor product of B-splines given by

$$f(a, w) = \sum_{p_1=1}^{P_1} \sum_{p_2=1}^{P_2} \beta_{p_1, p_2} B_{p_1}^1(a) B_{p_2}^2(w), \quad (3.7)$$

where  $B_{p_1}^1(\cdot)$  is the  $p_1$ th B-spline over the space  $\mathcal{A}$ , with  $p_1 \in \{1, \dots, P_1\}$  and  $P_1 = K_1 + 2$ , defined by a knot vector  $\mathbf{t}_1 = (t_{1,1}, t_{1,2}, \dots, t_{1,K_1})$ . Similarly for  $B_{p_2}^2(\cdot)$ . The ensemble of B-splines on the space  $\mathcal{A}$  and  $\mathcal{W}$  form a matrix basis denoted by  $\mathbf{B}^1$  and  $\mathbf{B}^2$  of size  $P_1 \times n$  and  $P_2 \times m$ , respectively, and  $[\beta_{p_1, p_2}]_{p_1=1, \dots, P_1; p_2=1, \dots, P_2}$  is a rectangular set of parameters.

### Regularised B-splines projected Gaussian Process

Given the B-splines indices and corresponding parameters  $\{(p_1, p_2), \beta_{p_1, p_2}\}_{p_1 \in \{1, \dots, P_1\}, p_2 \in \{1, \dots, P_2\}}$ , we place a 2D GP on the parameters,

$$\boldsymbol{\beta} \mid \boldsymbol{\phi} \sim \mathcal{GP}(0, \mathbf{K}_\beta). \quad (3.8)$$

The covariance matrix has entries  $(\mathbf{K}_\beta)_{(p_1, p_2), (p'_1, p'_2)} = \text{Cov}(\beta_{p_1, p_2}, \beta_{p'_1, p'_2}) = k_\beta((p_1, p_2), (p'_1, p'_2))$  where  $k_\beta(\cdot, \cdot)$  is a kernel function depending on unknown hyperparameters  $\boldsymbol{\phi}$ . This approach is equivalent to directly placing a GP on  $\mathbf{f}$  with a kernel function projected by B-splines. To show this, we rewrite (3.7) as a matrix calculation,  $\mathbf{f} = (\mathbf{B}^1)^T \boldsymbol{\beta} \mathbf{B}^2$ , and find its vectorized form

$$\text{vec}(\mathbf{f}) = \text{vec}\left((\mathbf{B}^1)^T \boldsymbol{\beta} \mathbf{B}^2\right) = (\mathbf{B}^2 \otimes \mathbf{B}^1)^T \text{vec}(\boldsymbol{\beta}). \quad (3.9)$$

The linear operator produces functions from  $\mathbb{R}^{P_1 P_2}$  to  $\mathbb{R}^{nm}$ . GPs are closed under linear operations (Papoulis and Pillai (2002), chap.10), and so  $\mathbf{f}$  specified by (3.7-3.8) is the GP

$$\mathbf{f} \mid \boldsymbol{\phi} \sim \mathcal{GP}\left(0, (\mathbf{B}^2 \otimes \mathbf{B}^1)^T \mathbf{K}_\beta (\mathbf{B}^2 \otimes \mathbf{B}^1)\right). \quad (3.10)$$

---

<sup>1</sup>“B-spline” refers to “B-spline basis function”.

### Properties of regularised B-splines projected Gaussian process

The kernel function obtained by composing a base kernel function with cubic B-splines is  $C^2$  as it can be represented as a linear combination of  $C^2$  functions (proof in Appendix S3.2). Therefore the surface obtained when modelling a surface  $\mathbf{f}$  with (3.10) is always smoother than with (3.5), when the same base kernel function  $k$  and  $k_\beta$  are used.

We can also interpret (3.10) as a regularised spline model. Indeed, existing regularised spline methods such as smoothing splines (O'Sullivan, 1986,9) and P-splines (Eilers and Marx, 1996; Eilers et al., 2006) aim to minimise within a frequentist setting the empirical loss function

$$\underbrace{\sum_{x_1 \in \mathcal{A}} \sum_{x_2 \in \mathcal{W}} \left( f(x_1, x_2) - \sum_{p_1=1}^{P_1} \sum_{p_2=1}^{P_2} \hat{\beta}_{p_1, p_2} B_{p_1}^1(x_1) B_{p_2}^2(x_2) \right)^2}_{\text{data fit}} + \underbrace{P}_{\text{penalty}}, \quad (3.11)$$

where  $\hat{\beta}$  are the estimated parameters and  $P$  is a penalty, which for smoothing splines is of the form

$$P = \sum_{x_1 \in \mathcal{A}} \sum_{x_2 \in \mathcal{W}} \left( \lambda_1 \left( \sum_{p_1=1}^{P_1} \sum_{p_2=1}^{P_2} \hat{\beta}_{p_1, p_2} (B_{p_1}^1(x_1))'' \right)^2 + \lambda_2 \left( \sum_{p_1=1}^{P_1} \sum_{p_2=1}^{P_2} \hat{\beta}_{p_1, p_2} (B_{p_2}^2(x_2))'' \right)^2 \right), \quad (3.12)$$

and for P-splines is of the form

$$P = \lambda_1 \sum_{p_2=1}^{P_2} \left( \mathbf{D}^d \hat{\beta}_{\cdot, p_2} \right)^2 + \lambda_2 \sum_{p_1=1}^{P_1} \left( \hat{\beta}_{p_1, \cdot} \mathbf{D}^d \right)^2. \quad (3.13)$$

The positive parameters  $\lambda_1$  and  $\lambda_2$  determine the amount of penalty applied. Here,  $\mathbf{D}_d$  is a matrix that forms differences of order  $d$ , i.e.,  $\mathbf{D}^d \hat{\beta}_{\cdot, p_2} = \Delta^d \hat{\beta}_{\cdot, p_2} = \sum_{p_1=d+1}^{P_1} (\hat{\beta}_{p_1, p_2} - \hat{\beta}_{(p_1-d), p_2})^2$ , such that for example  $\Delta^1 \hat{\beta}_{\cdot, p_2} = \sum_{p_1=2}^{P_1} (\hat{\beta}_{p_1, p_2} - \hat{\beta}_{(p_1-1), p_2})^2$ . Similarly,  $\hat{\beta}_{p_1, \cdot} \mathbf{D}^d = \Delta^d \hat{\beta}_{p_1, \cdot}$ . Now adopting a Bayesian approach, our aim is to maximise the probability of the posterior parameter conditional upon the data, which is proportional to the likelihood multiplied by the prior. We show that, by placing a GP on the parameters, the prior of  $\mathbf{f}$  modelled with a B-spline tensor product (3.10) can be decomposed in the same way as (3.11),

$$\log p(\text{vec}(\mathbf{f}) | \phi) \propto -\frac{1}{2} \left( \text{vec}(\mathbf{f})^T (\mathbf{B}^2 \otimes \mathbf{B}^1)^T \mathbf{K}_\beta (\mathbf{B}^2 \otimes \mathbf{B}^1) \text{vec}(\mathbf{f}) + \log \left| (\mathbf{B}^2 \otimes \mathbf{B}^1)^T \mathbf{K}_\beta (\mathbf{B}^2 \otimes \mathbf{B}^1) \right| \right) \quad (3.14a)$$

$$\propto -\frac{1}{2} \left( \underbrace{\text{vec}(\mathbf{f})^T (\mathbf{B}^2 \otimes \mathbf{B}^1)^T \mathbf{K}_\beta (\mathbf{B}^2 \otimes \mathbf{B}^1) \text{vec}(\mathbf{f})}_{\text{data fit}} + \underbrace{\log |\mathbf{K}_\beta|}_{\text{penalty}} \right), \quad (3.14b)$$

where  $|\mathbf{A}|$  denotes the determinant of matrix  $\mathbf{A}$ . Thus, the log determinant of the covariance matrix in (3.8) can be interpreted as a complexity penalty, or regulariser, which comes into play if the kernel has a free parameter to control the model complexity.

### 3.3 Numerical inference

All inferences using model (3.1-3.2) coupled with different priors on the random surface  $\mathbf{f}$  were fitted for each US state independently with RStan version 2.21.0, using an adaptive Hamiltonian Monte Carlo (HMC) sampler (Stan Development Team, 2020). 8 HMC chains were run in parallel for 2,500 iterations, of which the first 500 iterations were specified as warm-up. There were no divergent transitions throughout. Inferences in simulation analyses were performed similarly.

## 4 Simulation results

Prior to application to the CDC data, we compared the performance of three spatial models on simulation analyses. First, we considered a standard 2D GP as presented in (3.5) with a squared exponential kernel function with variance scale  $\zeta^2$  and specific lengthscales for the rows and the columns,  $\gamma_1$  and  $\gamma_2$ , such that  $\boldsymbol{\psi} = \{\zeta, \gamma_1, \gamma_2\}$ . The length scale priors were independent  $\gamma_i \sim \text{Inv-Gamma}(5, 5)$  for  $i = 1, 2$ , and  $\zeta \sim \text{Cauchy}(0, 1)$ .

Second, we considered a standard B-splines surface obtained via the tensor product (3.7), and by placing independent normal priors with common variance  $\zeta^2$  on all B-splines parameters, such that  $\boldsymbol{\psi} = \{\zeta\}$ . A Cauchy prior was placed on  $\zeta$ ,  $\zeta \sim \text{Cauchy}(0, 1)$ .

Third, we considered our regularised B-splines projected 2D GP presented in (3.10), where  $k_\beta$  was set to a squared exponential kernel function with variance scale  $\zeta^2$  and specific lengthscales for the rows and the columns,  $\gamma_1$  and  $\gamma_2$ , such that  $\boldsymbol{\psi} = \{\zeta, \gamma_1, \gamma_2\}$ . The length scale priors were independent  $\gamma_i \sim \text{Inv-Gamma}(5, 5)$  for  $i = 1, 2$ , and  $\zeta \sim \text{Cauchy}(0, 1)$ .

In the simulations, we considered observations on a 2D grid  $\{0, 0.2, \dots, 0.98, 1\} \times \{0, 0.2, \dots, 0.98, 1\}$ , such that there are  $50 \times 50$  entries. The observations are generated through a Gaussian model using as mean a 2D GP with a squared exponential kernel, which is perturbed using additional observation noise. The variance scale of the 2D GP is fixed to 1 and, to create three simulation scenarios, the length scale is varied ( $\gamma \in \{0.01, 0.1, 1\}$ ) to generate weakly, mildly and strongly correlated observations.

To fit the simulated observations we use as a likelihood a normal distribution with a mean specified by a spatial model and a free variance parameter. For the methods using B-splines, equidistant and similar knots are placed along the two axes.

Figure 2A shows the simulated mean of the observations and Figure 2B the observations obtained by perturbing the mean with observation noise, in the mildly correlation scenario,  $\gamma = 0.1$ . The estimated means of the predicted surface by the three methods are presented in Figures 2C-E. The standard 2D GP and the regularised B-splines

projected 2D GP recover the underlying smooth patterns has been perturbed by the observation noise (Figures 2C and E). Moreover, the regularised B-splines projected 2D GP obtains the same predictive performance as the standard 2D GP for a shorter running time, 73.66% faster on average (Table 1). In contrast, the standard B-splines approach overfits the data when the number of knots are greater than necessary (Figures 2D). Similar results were obtained for the other correlation scenarios (Figures S1 and S2 and Table 1).

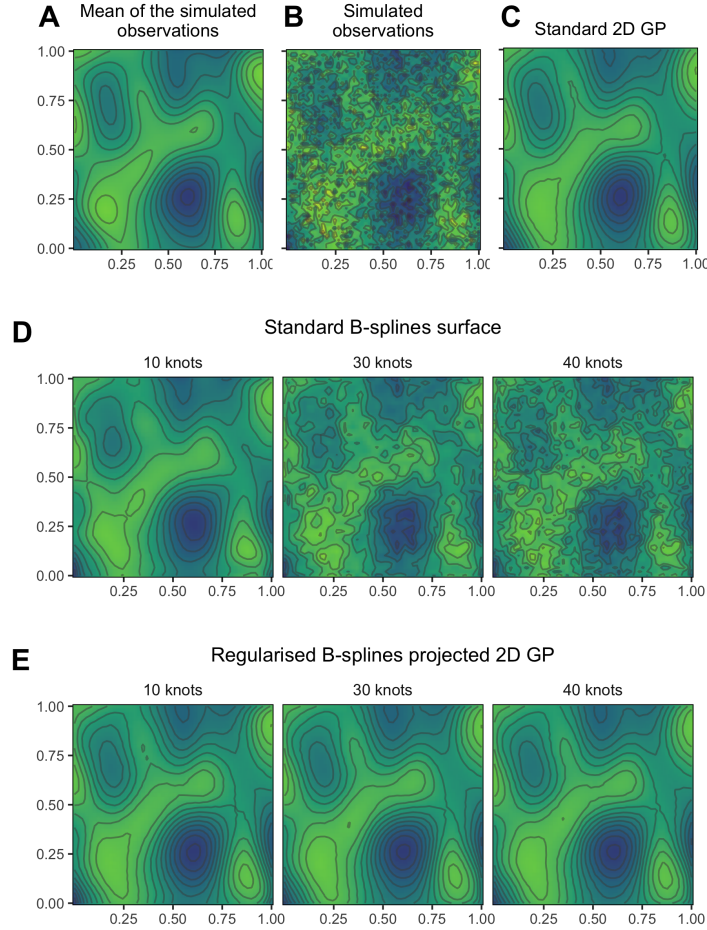


Figure 2: **Simulated data and posterior mean estimated by three spatial models.** (A) The mean of the simulated observation was obtained using a 2D GP with a squared exponential kernel implying a mild correlation ( $\gamma = 0.1$ ) (B) The simulated mean was perturbed with observation noise. The remaining subfigures show the estimated posterior mean surface, obtained by three models, (C) a standard 2D GP, (D) a standard B-splines surface, and (E) a regularised B-splines projected 2D GP.



| Model  | Simulation scenarios                       |  |  |
|--|--|--|--|
|  | Weakly correlated                          | Mildly correlated                          | Strongly correlated                        |
|  | $\Delta$ ELPD (SE)                         | $\Delta$ ELPD (SE)                         | $\Delta$ ELPD (SE)                         |
| <b>Standard 2D GP</b>                        | 0.00 (0.00)*                               | 0.00 (0.00)*                               | 0.00 (0.00)*                               |
| <b>Standard B-splines surface</b>            |  |  |  |
| Number of knots                              |  |  |  |
| 10   | -677.61 (31.31)                            | -22.75 (7.26)                              | -58.87 (11.35)                             |
| 30   | -93.82 (17.27)                             | -186.95 (19.60)                            | -446.93 (29.31)                            |
| 40   | -207.29 (22.73)                            | -288.27 (23.20)                            | -737.79 (33.69)                            |
| <b>Regularised B-splines projected 2D GP</b> |  |  |  |
| Number of knots                              |  |  |  |
| 10   | -678.31 (31.32)                            | -5.88 (3.12)*                              | -3.15 (4.02)*                              |
| 30   | -3.62 (6.28)*                              | -1.71 (2.87)*                              | -8.27 (5.11)*                              |
| 40   | -4.57 (6.25)*                              | -1.29 (2.83)*                              | -8.54 (4.38)*                              |
| Standard 2D GP                               | run time in minute<br>(-%longest run time) | run time in minute<br>(-%longest run time) | run time in minute<br>(-%longest run time) |
|  | 25 (-0.00%)                                | 26 (-0.00%)                                | 141 (-0.00%)                               |
| <b>Standard B-splines surface</b>            |  |  |  |
| Number of knots                              |  |  |  |
| 10   | 2 (-92.70%)                                | 2 (-91.98%)                                | 4 (-97.04%)                                |
| 30   | 6 (-76.98%)                                | 4 (-84.68%)                                | 8 (-94.11%)                                |
| 40   | 9 (-64.52%)                                | 8 (-70.98%)                                | 11 (-91.87%)                               |
| <b>Regularised B-splines projected 2D GP</b> |  |  |  |
| Number of knots                              |  |  |  |
| 10   | 2 (-91.91%)                                | 4 (-83.81%)                                | 22 (-84.39%)                               |
| 30   | 12 (-52.78%)                               | 13 (-52.58%)                               | 78 (-45.21%)                               |
| 40   | 17 (-32.47%)                               | 16 (-39.93%)                               | 79 (-44.22%)                               |

\* Equivalent best predictive performance.

Table 1: **Predictive performances and running times obtained by three spatial models on simulated data. (Top)** The differences in the expected log pointwise predictive density (ELPD) (Vehtari et al., 2016), and standard error of the difference, of each model compared to the best performing model (for which the difference is null) are presented. A higher expected log pointwise predictive density suggests a better predictive capacity. **(Bottom)** The proportional decrease in running time compared to the slowest model (for which the proportional decrease is null).

## 5 Benchmark results

We next benchmarked the performance of the spatial models on predicting deviations in land surface temperatures in East Africa (Ton et al., 2018). The data, shown in Supplementary Figure S3A, consist of more than 83,000 locations across East Africa with measured deviations in land surface temperatures, and has been used previously to evaluate spatial models. We use the same training data as in Mishra et al. (2020), consisting of 6,000 uniformly sampled locations (Supplementary Figure S3B), and fit them using as likelihood a normal distribution with a mean specified by a spatial model, and a free variance parameter. Supplementary Figures S3C-D exemplify the results we obtained with a standard 2D B-splines prior, and the regularised B-splines projected 2D GP prior. The regularised B-splines projected 2D GP obtained significantly better predictive performance than the standard B-splines surface model (testing MSE respectively 2.96 and 4.34), and similar or better predictive performance than a standard 2D GP approach (testing MSE: 2.47), a low rank Gaussian Markov random field (testing MSE: 4.36), and a neural network model (testing MSE: 14.94) (Mishra et al., 2020). It had worse predictive performance than the  $\pi$ VAE model (testing MSE: 0.38), but training  $\pi$ VAE is not trivial and requires considerably large computational runtimes, even if inference time is not large.

## 6 Age profile of COVID-19 deaths in the United States

### 6.1 Comparison of random surface priors for one US state

We next used the non-parametric model (3.1-3.2) to fit weekly COVID-19 attributable deaths by age from the CDC data for one state, Florida. We compare results for the three prior specifications on the random surface which specifies the age composition of deaths over time, a standard 2D GP, a standard B-splines surface and our regularised B-splines projected GP (see in Section 4). For the models involving B-splines, we placed 12 equidistant knots over the age axis and 4 over the week axis. This choice was determined such that the predictive performance did not significantly increase with more knots.

Figure 3A shows the CDC data for Florida, illustrating the end of the first wave and the complete second and third epidemic waves of COVID-19 that occurred in Florida. Weekly deaths are missing for two weeks, and for multiple age-week combinations. For the week starting January 23, 2021, the reported deaths are unrealistically high. We combined the CDC data with the age-aggregated, weekly COVID-19 attributable deaths reported by JHU, shown as a black line, to predict weekly deaths by 1-year age bands from May 2, 2020 to May 15, 2021 in order to adjust predictions for the reporting delays in the CDC data. Figure 3B presents the posterior mean predictions of weekly, COVID-19 attributable deaths by age that were obtained using the regularised B-splines projected GP prior. The figure illustrates how the reporting delays apparent in the CDC data are adjusted for using the JHU data as external calibration, and how the discretized CDC data informs our estimates of the age composition of deaths.

Figure 3C shows the estimated age-specific composition of weekly COVID-19 attributable deaths in three weeks for the three prior specifications. The posterior distri-

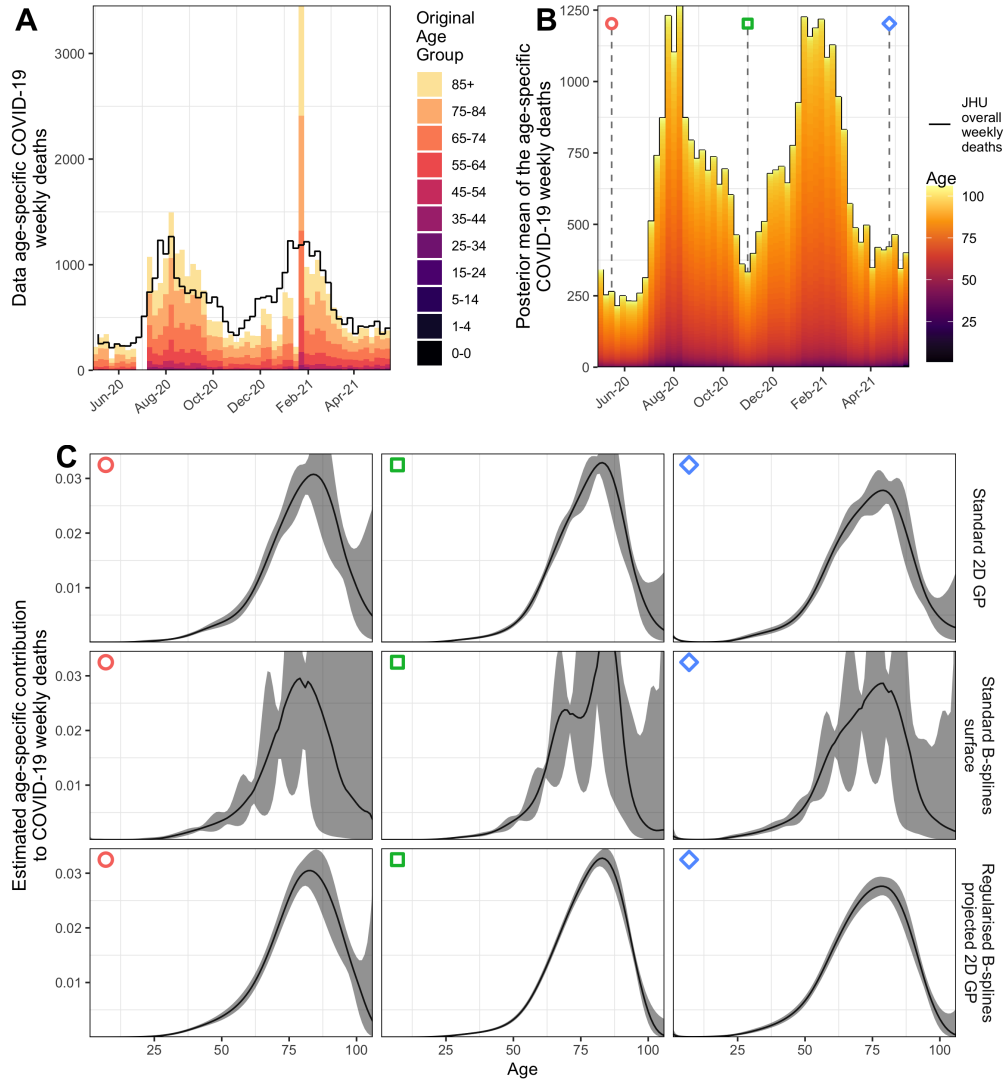
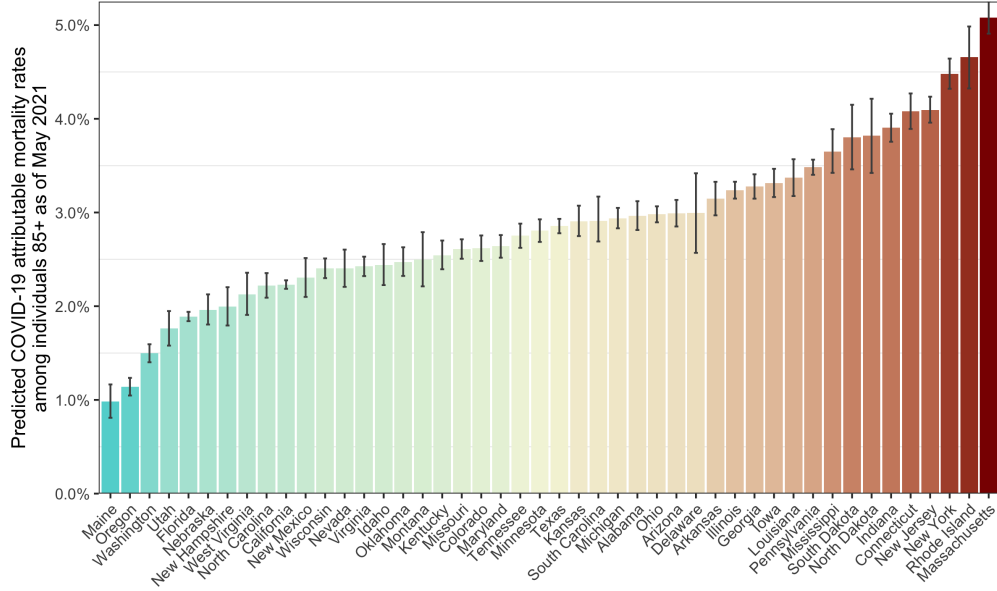


Figure 3: **Estimated age-specific contribution to weekly COVID-19 attributable deaths by three priors.** (A) Weekly COVID-19 attributable deaths reported by the CDC stacked by age groups (color) (B) Posterior mean of the weekly COVID-19 attributable deaths stacked by age, estimated with a regularised B-splines projected GP prior. Three weeks in the observation period are selected and designated by a shape. The black line shows the all-age weekly COVID-19 attributable deaths reported by JHU, that were used to adjust the CDC data for reporting delays (3.4). (C) Posterior median (black line) and 95% credible interval (ribbon) of the age-specific contribution to COVID-19 attributable deaths in three weeks.



## 6.2 Age-specific COVID-19 attributable mortality rates as of May 2021

Using our Bayesian non-parametric approach, we are able to predict COVID-19 attributable mortality rates by arbitrary age bands for all US states. Given our performance evaluation in Section 6.1, we fitted model (3.1-3.2) with the regularised B-splines projected GP prior to the CDC data to characterise the age profile of deaths over time. As before we used the weekly, all-age COVID-19 attributable deaths reported by JHU to adjust for reporting delays in the CDC data. Four states, Alaska, Hawaii, Vermont and Wyoming had few retrievable weekly deaths (Figure 1), and were excluded. Detailed model fits for all states are shown in Appendix S4. Figure 4 shows the posterior median predictions of COVID-19 attributable mortality rates among individuals aged 85+, along with 95% credible intervals. By May 15, 2021, more than a staggering 2.5% of the entire population aged 85+ were lost to COVID-19 in more than half of all states, with the top 5 states being Massachusetts, Rhode Island, New York, New Jersey and Connecticut. For the younger age groups, mortality rates decrease rapidly (Supplementary Figures S5-S8). In more than half the states, at least 1% of the population aged 75-84, and 0.23% of the population aged 55-74 lost their lives from COVID-19.

## 6.3 Differences in the age profile of COVID-19 attributable deaths across states

The variation in predicted mortality rates across states clearly reflects the scale of the epidemic in each state, with states that were hit hardest in the first wave experiencing the highest mortality rates per capita. Yet, Figure 4 prompts the question if the age composition of COVID-19 attributable deaths differs across states. To address this question, we focus on the baseline period of the first 3 months after the 10th cumulated death in each state, and aggregate the predictions of the share of 1-year age bands from our non-parametric model into the age strata 0-24, 25-54, 55-74, 75-84, 85+ years for each state during the baseline period. In these calculations, we adjusted for age differences in state populations by calculating mortality rates per 1-year age band, and multiplying these rates with the age composition of the US population. Strikingly, the resulting posterior estimates of the share of age groups among COVID-19 attributable deaths were statistically significantly different across states even after standardising the age composition of state populations (Figure 5). For example, the contributions of individuals aged 85+ to COVID-19 attributable deaths ranged from 22.53% (18.73%- 26.53%) in Nevada to 50.52% (44.41%- 56.54%) in New Hampshire. High heterogeneity was also found in the contributions from individuals age 55-74, which varied from 14.1% (9.93%- 19.33%) in Maine to 40.44% (35.97%- 45.03%) in Oklahoma. These discrepancies across states are clearly supported in the empirical data, albeit without an assessment of their statistical significance (Supplementary Figure S4).

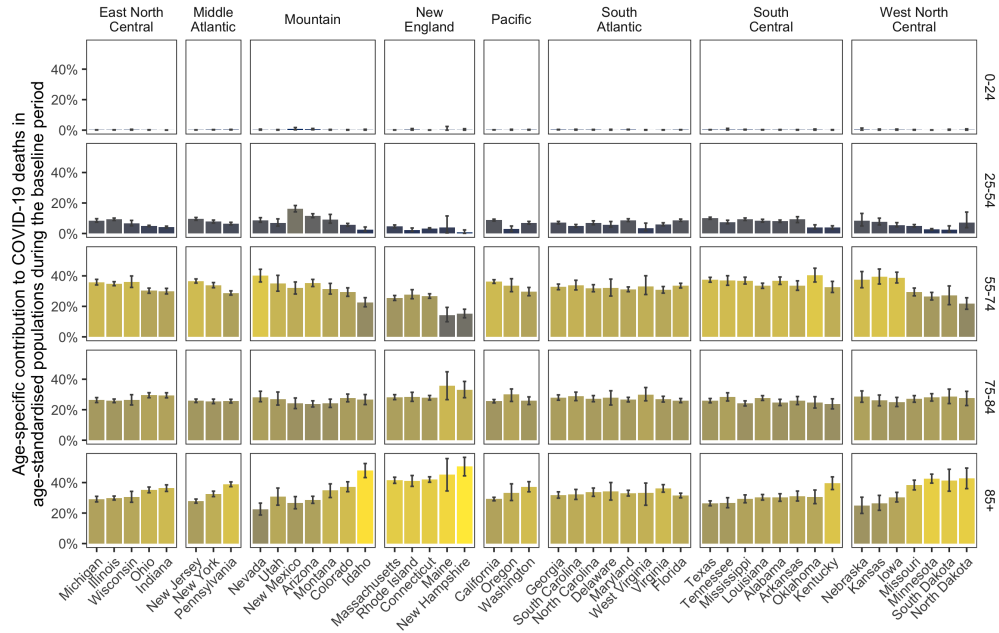


Figure 5: **Estimated contribution of age groups to COVID-19 attributable deaths in the first 3 months of state epidemics.** Posterior median estimates of each age group to COVID-19 attributable deaths are shown for each state (barplot), along with 95% credible intervals (error bars). Estimates are for the 3 months after the 10th cumulative death in each state, and are adjusted for differences in the age composition of state populations (see text).

#### 6.4 Time trends in the age profile of COVID-19 attributable deaths

With high levels of protection from fatal outcomes post vaccination (Haas et al., 2021; Baden et al., 2021), parts of the world are beginning to see significant reductions in COVID-19 attributable deaths. Here, we estimate and report the scale at which shifts in the age profile of COVID-19 attributable deaths are occurring across the US, as vaccines are being prioritised to older age groups to minimize overall fatal outcomes. Figures 6-7 illustrate the predicted, weekly COVID-19 attributable deaths in the three age groups 0-54, 55-74 and 75+ across the US, that we obtained with model (3.1-3.2), and using the regularised B-splines projected GP prior. The empirical data, shown as dots, and our posterior median predictions with 95% credible intervals, shown as lines and ribbons, clearly reflect the second and third waves across the US, and illustrate substantial reductions in deaths since vaccination roll-out in every US state since January 16, 2021, the earliest date for which vaccine coverage are reported. Within 16 weeks and until May 15, 2021, the predicted, weekly COVID-19 attributable deaths among 75+ in the US dropped from 13,113 (12,914-13,307) to 1,518 (1,445-1,592), cor-

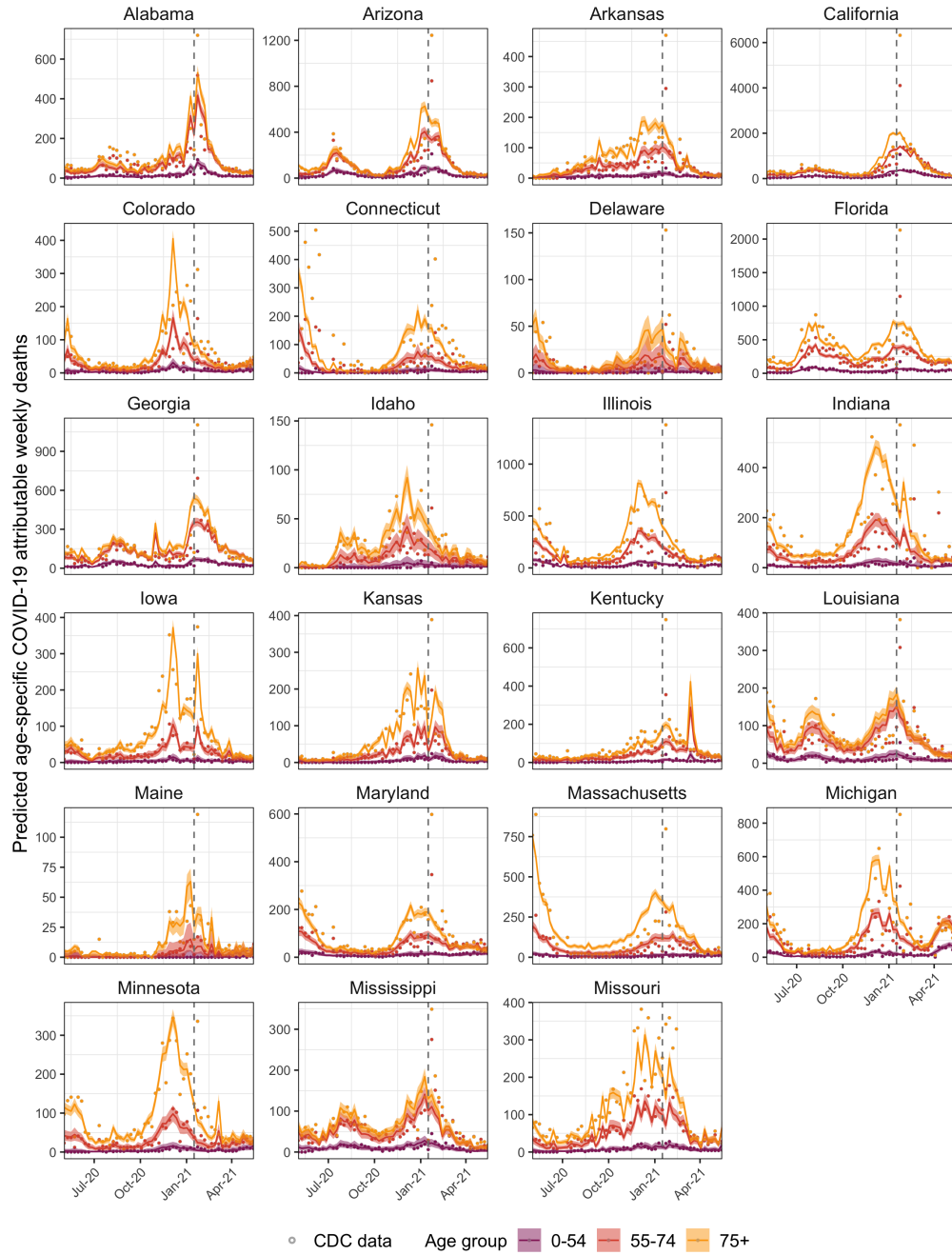


Figure 6: **Predicted weekly, COVID-19 attributable deaths by three age groups (part 1).** Shown are the posterior median (line) and 95% credible intervals (ribbon) of the predicted weekly COVID-19 attributable deaths of the non-parametric age model with regularised B-splines projected GP prior. The CDC data are shown as round dots. Darker colors indicate younger age groups and lighter colors indicate older age groups. The earliest date at which vaccine coverage are report by the CDC is shown as a dashed vertical line.



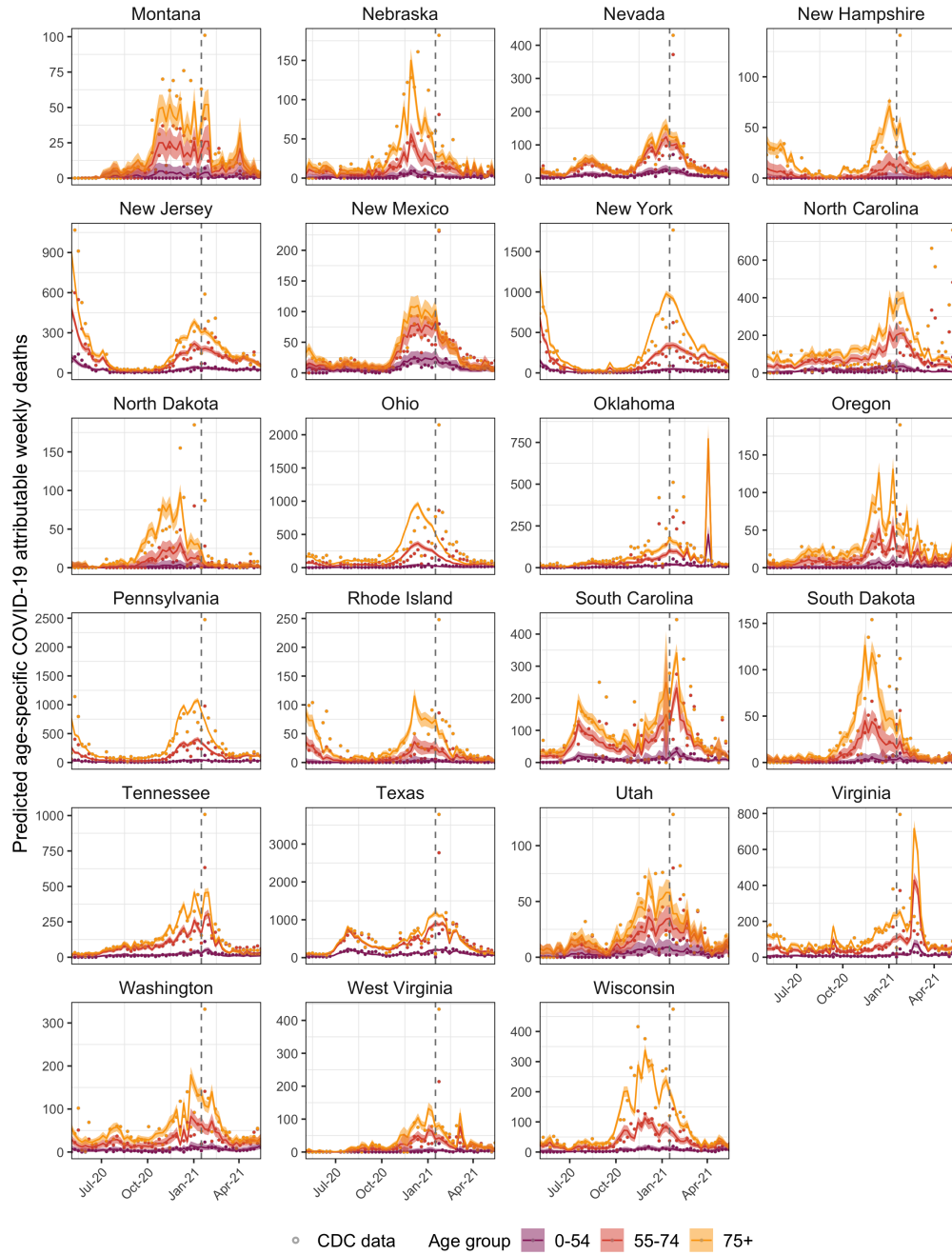


Figure 7: **Predicted weekly, COVID-19 attributable deaths by three age groups (part 2).** Shown are the posterior median (line) and 95% credible intervals (ribbon) of the predicted weekly COVID-19 attributable deaths of the non-parametric age model with regularised B-splines projected GP prior. The CDC data are shown as round dots. Darker colors indicate younger age groups and lighter colors indicate older age groups. The earliest date at which vaccine coverage are report by the CDC is shown as a dashed vertical line.

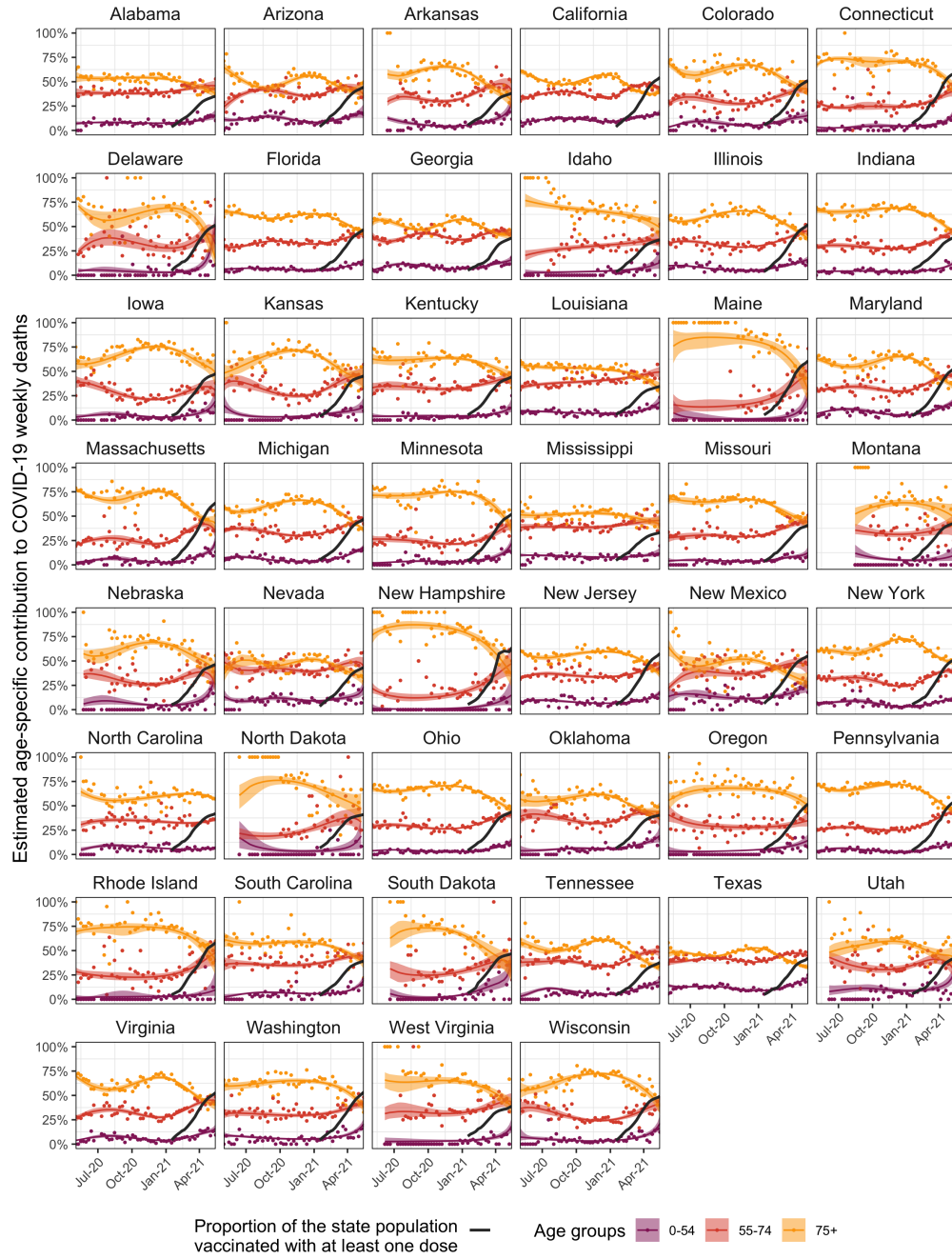


Figure 8: **Estimated time trends in the age composition of weekly COVID-19 attributable deaths.** Shown are in color the posterior median estimate (line) in the age composition of weekly COVID-19 attributable deaths for three age groups, along with 95% credible intervals (ribbon), and empirical estimates from the CDC data (dots). The proportion of the state population vaccinated with at least one dose is shown as a black line.

responding to a 88.42% (87.84%-89.01%) decrease. The drop was heterogeneous across states, with Delaware showing the fastest decline of COVID-19 weekly deaths among 75+, amounting to 97.62% (89.74%-100.00%), and Michigan showing the slowest decline, representing 61.83% (54.23%-68.65%). Similar trends were observed in the CDC data without calibrating predictions to the number of weekly COVID-19 attributable deaths to those reported in the JHU data. The weekly COVID-19 attributable deaths among 75+ in the US reported by the CDC fell from 7,558 to 2,155, corresponding to a 71.49% decrease. For comparison, the predicted, weekly COVID-19 attributable deaths among individuals aged 55-74 and individuals aged 0-54 decreased by 77.85% (76.66%-79.00%) and 52.26% (46.64%-57.47%) over the same period, respectively.

Figure 8 shows the corresponding, estimated contributions of ages 0-54, 55-74 and 75+ to COVID-19 weekly deaths over time, along with the empirical data. Since vaccinations began, we find significant shifts in the proportion of deaths by age. On January 16, 2021, the estimated contribution of individuals aged 75+ to weekly deaths was 63.13% (61.14%-65.12%). As of May 01, 2021, this has dropped to 43.25% (37.64%-48.93%). Overall, from May 01, 2021 to January 16, 2021, for every percent of the population vaccinated with at least one dose, we find across the US a population-level reduction of 0.41% (0.38%-0.45%) in the share of individuals aged 75+ among deaths. However this reduction is not homogeneous. New Hampshire, Maine, Delaware, Massachusetts and Maryland exhibited a faster drop in the contribution of older individuals to deaths than the US average, while North Carolina, Mississippi, Idaho, Oregon and Alabama showed a slower one. In recent weeks, from May 01, 2021 to May 15, 2021, we find evidence that the predicted, weekly COVID-19 attributable deaths of individuals aged 55-74 decreased more rapidly than those among individuals aged 75+ in some states, Arizona, California, Georgia and Oklahoma, and correspondingly the contribution to weekly deaths from individuals aged 75+ is increasing again in these states.

## 7 Discussion

We present a Bayesian non-parametric modelling approach to estimate and report longitudinal trends in the age composition of COVID-19 attributable deaths before and since vaccine roll-out in the United States. We find that, as of May 15, 2021, more than 4% of the population aged 85+ lost their life to COVID-19 in Massachusetts, Rhode Island, New York and Connecticut, of similar magnitude as in many metropolitan areas in Brazil, such as Sao Paulo (SRAG, 2021). These mortality figures are lower in other states that also reported early spread COVID-19, such as California (2.23% (2.19%-2.28%) mortality rate among individuals aged 85+) and Washington (1.50% (1.40%-1.59%) mortality rate among individuals aged 85+).

The estimated heterogeneity in mortality rates is in part a result of large individual state epidemics (Institute for Health Metrics and Evaluation, 2020; Unwin et al., 2020), but also in part a consequence of differences in the age composition of COVID-19 attributable deaths across US states during the first months of the epidemic, even when populations are age-standardised. High COVID-19 related mortality has been in particular reported in nursing homes (The New York Times, 2021; Centers for Disease

[Control and Prevention, 2021b](#)). Five states, Massachusetts, Connecticut, North Dakota, Minnesota, Rhode Island and New Hampshire reported that at least half of all COVID-19 attributable deaths occurred in nursing homes. Here we also find these states among those that are associated with a higher than average share of individuals aged 85+ among COVID-19 attributable deaths. Other factors, such as ethnic or racial differences in the populations affected could also play a key role, since the non-White or Hispanic populations in the US are disproportionately affected by COVID-19 ([Hooper et al., 2020](#); [Wadhera et al., 2020](#); [Millett et al., 2020](#)), and are also younger when compared to the non-Hispanic White population ([Katherine Schaeffer, 2019](#)). It is also possible that COVID-19 transmission dynamics differed by age across states, with previous analyses indicating that higher proportions of cases originated from adults aged 20-49 in the Southern, South-western, and Western regions of the US ([Monod et al., 2021](#)).

Since vaccination roll-out data started to be reported on January 16, 2021 in the US, we find that the number of weekly COVID-19 attributable deaths has substantially declined in the populations aged 75+ in almost all states, although from the end of March, increases are found for Michigan and from the end of April for Arizona, Colorado, Illinois, Missouri and Oregon. Similar, albeit less pronounced decreases in weekly COVID-19 attributable deaths are also seen for individuals aged 0 – 54 and 55-74. The precipitous declines in mortality in higher age groups have occurred in large part due to the nation wide vaccine roll-out. Similarly, subsequent rises are likely due to the emergence of vaccine/immune evading SARS-CoV-2 variants. The decreases in weekly COVID-19 attributable deaths were also accompanied by substantial and significant shifts the age profile of COVID-19 attributable deaths, with 0.41% (0.38%-0.45%) population-level reduction in the share of individuals aged 75 among deaths for every percent of the population vaccinated with at least one dose.

Our estimates are based on a fully Bayesian, non-parametric model that describes time trends in the age profile of COVID-19 deaths through a 2D random surface that is regularised with B-splines projected Gaussian process priors. We find on simulations and a benchmark data set of deviations in land surface temperatures ([Ton et al., 2018](#)) that the model is associated with favourable predictive accuracy as compared to a standard B-splines prior ([d. Boor, 1978](#)), a standard GP prior ([Rasmussen and Williams, 2005](#)) and low rank Gaussian Markov random field prior ([Lindgren et al., 2011](#); [Rue et al., 2009](#)), and substantially faster than a GP prior ([Rasmussen and Williams, 2005](#)). Intuitively, placing a GP prior on the B-splines coefficients enables the model to learn the number of B-splines functions needed to describe the target surface. Theoretically, we show that the model is again a GP, and derive the B-splines projected kernel function of the GP. We also show that the model can be interpreted as regularised B-splines, and find that the negative determinant of the covariance matrix in the log-likelihood, often referred to as Occam’s factor ([MacKay \(2003\), chap. 28](#)), plays the same role as the penalty of smoothing splines and P-splines ([O’Sullivan, 1986](#); [Eilers and Marx, 1996](#)). We can also bound the computational complexity to compute the covariance matrix of the low-rank GP prior to  $\mathcal{O}(2(P_1 \times P_2)^{3/2})$ , where  $P_1$  and  $P_2$  are the number of B-splines on the  $x$  and  $y$  axes, as compared to a standard 2D GP with computational complexity  $\mathcal{O}(2(n \times m)^{3/2})$ , where  $n$  and  $m$  are the number of points on the  $x$  and  $y$  axes. For example, in the simulation analysis the 2D surface is of size  $n = 50$  and  $m = 50$ . Using

a regularised B-splines projected GP with  $P_1 = P_2 = 32$  gave an equivalent predictive performance as a standard 2D GP, for all simulation scenarios, while computational complexity decreases from  $25 \times 10^4$  for a standard 2D GP to  $6.5 \times 10^4$  for the regularised through B-spline projected GP.

This study has several limitations. First, it is likely that the COVID-19 attributable deaths that we predict for each age group remain an underestimate, considering in particular that US excess deaths exceed the COVID-19 attributable deaths reported by the CDC, state DoH, and JHU ([Centers for Disease and Prevention, 2021](#)). Second, there are instances of unusually large weekly COVID-19 attributable deaths in the JHU data, which are likely reflecting unresolved reporting delays. Since we use the JHU data as a reference to mitigate reporting delays in the CDC data, our inferences remain affected by these anomalies in the JHU data. Third, it is not possible to attribute the significant shifts in the age profile of COVID-19 attributable deaths directly and causally increasing vaccination coverage. In several states the COVID-19 epidemics were in decline prior to vaccination roll-out, and so the reduction in COVID-19 attributable deaths is in part a result of changes in disease dynamics regardless of vaccination. Further, some emerging SARS-CoV-2 variants are associated with higher case fatality rates among younger individuals ([de Oliveira et al., 2021](#)), and could also, potentially in part, account for the observed shifts in the age profile of COVID-19 attributable deaths. Considering our statistical approach, we note fourth that the regularised B-splines projected GP prior is twice continuously differentiable, and so cannot be recommended for modelling discontinuous surfaces observed in physical or industrial processes.

Here, we find that the age profile of COVID-19 attributable deaths has changed substantially since COVID-19 vaccinations began in the US, across all US states. The recent changes in the age composition of COVID-19 deaths that we characterise are substantially larger than historic fluctuations in the age profile of COVID-19 deaths, and indicate the substantive benefit that vaccination has on preventing fatal disease outcomes. Yet, it is not possible to attribute the entire reduction in COVID-19 attributable deaths over the past months to vaccination, since overall epidemics are in decline across US states and new SARS-CoV-2 variants with potentially different infection profiles are emerging. The high cumulative mortality rates that we report for several US states demonstrate the continued urgency to offer vaccines to everyone, not only in the US, but globally.

## Supplementary Material

### Supplementary Figures and Tables.

**Modelling COVID-19 weekly deaths.** 2 parts: (1) Finding weekly death count from censored and missing cumulative death count from the CDC data and, (2) specifying the likelihood form.

**B-splines and properties of the regularised B-splines projected Gaussian Process prior.** 2 parts: (1) Construction of a B-spline curve and a B-spline surface and, (2) Proof that a baseline kernel function projected with cubic B-splines is a  $\mathcal{C}^2$  function.

**State level summary.** Detailed fit summary for every US state

## References

- Baden, L. R., Sahly, H. M. E., Essink, B., Kotloff, K., Frey, S., Novak, R., Diemert, D., Spector, S. A., Roupheal, N., Creech, C. B., McGettigan, J., Khetan, S., Segall, N., Solis, J., Brosz, A., Fierro, C., Schwartz, H., Neuzil, K., Corey, L., Gilbert, P., Janes, H., Follmann, D., Marovich, M., Mascola, J., Polakowski, L., Ledgerwood, J., Graham, B. S., Bennett, H., Pajon, R., Knightly, C., Leav, B., Deng, W., Zhou, H., Han, S., Ivarsson, M., Miller, J., and Zaks, T. (2021). “Efficacy and Safety of the mRNA-1273 SARS-CoV-2 Vaccine.” *New England Journal of Medicine*, 384(5): 403–416. [17](#)
- Baguelin, M., Flasche, S., Camacho, A., Demiris, N., Miller, E., and Edmunds, W. J. (2013). “Assessing Optimal Target Populations for Influenza Vaccination Programmes: An Evidence Synthesis and Modelling Study.” *PLoS Medicine*, 10(10): e1001527. [2](#)
- Boehmer, T. K., DeVies, J., Caruso, E., van Santen, K. L., Tang, S., Black, C. L., Hartnett, K. P., Kite-Powell, A., Dietz, S., Lozier, M., and Gundlapalli, A. V. (2020). “Changing Age Distribution of the COVID-19 Pandemic — United States, May–August 2020.” *MMWR. Morbidity and Mortality Weekly Report*, 69(39): 1404–1409. [2](#)
- Brazeau, N. F., Verity, R., Jenks, S., Fu, H., Whittaker, C., Winskill, P., Dorigatti, I., Walker, P., Riley, S., Schnekenberg, R. P., Hoeltgebaum, H., Mellan, T. A., Mishra, S., Whittles, L., Bhatt, S., Ghani, A. C., Ferguson, N. M., and Okell, L. C. (2020). “Report 34 - COVID-19 Infection Fatality Ratio Estimates from Seroprevalence.” *Imperial College London*. [2](#)
- Centers for Disease and Prevention (2021). “Excess Deaths Associated with COVID-19.” [https://www.cdc.gov/nchs/nvss/vsrr/covid19/excess\\_deaths.htm](https://www.cdc.gov/nchs/nvss/vsrr/covid19/excess_deaths.htm). [23](#)
- Centers for Disease Control and Prevention (2021a). “COVID-19 Vaccinations in the United States.” <https://covid.cdc.gov/covid-data-tracker/#vaccinations>. [4](#)



- (2021b). “Interim Infection Prevention and Control Recommendations to Prevent SARS-CoV-2 Spread in Nursing Homes”. <https://www.cdc.gov/coronavirus/2019-ncov/hcp/long-term-care.html#print>. 21
- (2021c). “Weekly Updates by Select Demographic and Geographic Characteristics”. <https://www.cdc.gov/nchs/nvss/vsrr/covid-weekly/index.htm>. 2, 3, 5
- Cortis, D. (2020). “On Determining the Age Distribution of COVID-19 Pandemic.” *Frontiers in Public Health*, 8. 2
- d. Boor, C. (1978). *A Practical Guide to Splines*. New York: Springer Verlag. 22, 43
- de Oliveira, M. H. S., Lippi, G., and Henry, B. M. (2021). “Sudden rise in COVID-19 case fatality among young and middle-aged adults in the south of Brazil after identification of the novel B.1.1.28.1 (P.1) SARS-CoV-2 strain: analysis of data from the state of Parana.” *medRxiv*. 23
- Eilers, P. H., Currie, I. D., and Durbán, M. (2006). “Fast and compact smoothing on large multidimensional grids.” *Computational Statistics & Data Analysis*, 50(1): 61–76. 2, 9
- Eilers, P. H. C. and Marx, B. D. (1996). “Flexible smoothing with B-splines and penalties.” *Statistical Science*, 11(2). 2, 9, 22
- Goldman, R. (2002). *Pyramid Algorithms*. Morgan Kaufmann. 8, 43
- Gönen, M. and Alpaydin, E. (2011). “Multiple Kernel Learning Algorithms.” *Journal of Machine Learning Research*, 12(64): 2211–2268. 7
- Haas, E. J., Angulo, F. J., McLaughlin, J. M., Anis, E., Singer, S. R., Khan, F., Brooks, N., Smaja, M., Mircus, G., Pan, K., Southern, J., Swerdlow, D. L., Jodar, L., Levy, Y., and Alroy-Preis, S. (2021). “Impact and effectiveness of mRNA BNT162b2 vaccine against SARS-CoV-2 infections and COVID-19 cases, hospitalisations, and deaths following a nationwide vaccination campaign in Israel: an observational study using national surveillance data.” *The Lancet*, 397(10287): 1819–1829. 17
- Hooper, M. W., Nápoles, A. M., and Pérez-Stable, E. J. (2020). “COVID-19 and Racial/Ethnic Disparities.” *JAMA*, 323(24): 2466. 22
- Institute for Health Metrics and Evaluation (2020). “Modeling COVID-19 scenarios for the United States.” *Nature Medicine*, 27(1): 94–105. 21
- Islam, N., Shkolnikov, V. M., Acosta, R. J., Klimkin, I., Kawachi, I., Irizarry, R. A., Alicandro, G., Khunti, K., Yates, T., Jdanov, D. A., White, M., Lewington, S., and Lacey, B. (2021). “Excess deaths associated with covid-19 pandemic in 2020: age and sex disaggregated time series analysis in 29 high income countries.” *BMJ*, n1137. 3
- John Hopkins University of Medicine (2020). “Coronavirus Resource Center.” Available at <https://coronavirus.jhu.edu/data>. 3, 4
- Katherine Schaeffer (2019). “The most common age among whites in U.S. is 58 – more than double that of racial and ethnic minorities”. <https://www.pewresearch.org/fact-tank/2019/07/30/most-common-age-among-us-racial-ethnic-groups/>. 22



- King, A. A., de Cellès, M. D., Magpantay, F. M. G., and Rohani, P. (2015). “Avoidable errors in the modelling of outbreaks of emerging pathogens, with special reference to Ebola.” *Proceedings of the Royal Society B: Biological Sciences*, 282(1806): 20150347. [3](#)
- Lax, P. D. and Terrell, M. S. (2017). *Multivariable Calculus with Applications*. Springer International Publishing. [45](#), [46](#)
- Levin, A. T., Hanage, W. P., Owusu-Boaitey, N., Cochran, K. B., Walsh, S. P., and Meyerowitz-Katz, G. (2020). “Assessing the age specificity of infection fatality rates for COVID-19: systematic review, meta-analysis, and public policy implications.” *European Journal of Epidemiology*, 35(12): 1123–1138. [2](#)
- Lindgren, F., Rue, H., and Lindström, J. (2011). “An explicit link between Gaussian fields and Gaussian Markov random fields: the stochastic partial differential equation approach.” *Journal of the Royal Statistical Society: Series B (Statistical Methodology)*, 73(4): 423–498. [22](#)
- MacKay, D. J. C. (2003). *Information Theory, Inference and Learning Algorithms*. Cambridge University Press, 1st edition. [22](#)
- Meyerowitz-Katz, G. and Merone, L. (2020). “A systematic review and meta-analysis of published research data on COVID-19 infection fatality rates.” *International Journal of Infectious Diseases*, 101: 138–148. [2](#)
- Millett, G. A., Jones, A. T., Benkeser, D., Baral, S., Mercer, L., Beyrer, C., Honermann, B., Lankiewicz, E., Mena, L., Crowley, J. S., Sherwood, J., and Sullivan, P. S. (2020). “Assessing differential impacts of COVID-19 on black communities.” *Annals of Epidemiology*, 47: 37–44. [22](#)
- Mishra, S., Flaxman, S., Zhu, H., and Bhatt, S. (2020). “ $\pi$ VAE: Encoding stochastic process priors with variational autoencoders.” *arXiv*. [13](#), [32](#)
- Monod, M., Blenkinsop, A., Xi, X., Hebert, D., Bershan, S., Tietze, S., Baguelin, M., Bradley, V. C., Chen, Y., Coupland, H., Filippi, S., Ish-Horowicz, J., McManus, M., Mellan, T., Gandy, A., Hutchinson, M., Unwin, H. J. T., van Elsland, S. L., Vollmer, M. A. C., Weber, S., Zhu, H., Bezancon, A., Ferguson, N. M., Mishra, S., Flaxman, S., Bhatt, S., and Ratmann, O. (2021). “Age groups that sustain resurging COVID-19 epidemics in the United States.” *Science*, 371(6536): eabe8372. [22](#)
- O’Sullivan, F. (1986). “A Statistical Perspective on Ill-Posed Inverse Problems.” *Statistical Science*, 1(4): 502–518. [2](#), [9](#), [22](#)
- (1988). “Fast Computation of Fully Automated Log-Density and Log-Hazard Estimators.” *SIAM Journal on Scientific and Statistical Computing*, 9(2): 363–379. [2](#), [9](#)
- Papoulis, A. and Pillai, S. U. (2002). *Probability, Random Variables, and Stochastic Processes*. McGraw-Hill Higher Education. [8](#)
- Perperoglou, A., Sauerbrei, W., Abrahamowicz, M., and Schmid, M. (2019). “A review

- of spline function procedures in R.” *BMC Medical Research Methodology*, 19(1).  
URL <https://doi.org/10.1186/s12874-019-0666-3> 43
- Rasmussen, C. E. and Williams, C. K. I. (2005). *Gaussian Processes for Machine Learning*. The MIT Press. 2, 22
- Rearc (2021). “Provisional COVID-19 Death Counts by Sex, Age, and State — CDC / NCHS”. <https://github.com/rearc-data/covid-19-death-counts-sex-age-state>. 3
- Rue, H., Martino, S., and Chopin, N. (2009). “Approximate Bayesian inference for latent Gaussian models by using integrated nested Laplace approximations.” *Journal of the Royal Statistical Society: Series B (Statistical Methodology)*, 71(2): 319–392. 22
- Saatçi, Y. (2011). “Scalable Inference for Structured Gaussian Process Models.” *PhD thesis, University of Cambridge*. 2, 7
- SRAG (2021). “Banco de Dados de Síndrome Respiratória Aguda Grave.” <https://opendatasus.saude.gov.br/dataset/bd-srag-2021>. 21
- Stan Development Team (2020). “RStan: the R interface to Stan.” R package version 2.21.2.  
URL <http://mc-stan.org/> 10
- The New York Times (2021). “Nearly One-Third of U.S. Coronavirus Deaths Are Linked to Nursing Homes”. <https://www.nytimes.com/interactive/2020/us/coronavirus-nursing-homes.html>. 21
- Ton, J.-F., Flaxman, S., Sejdinovic, D., and Bhatt, S. (2018). “Spatial mapping with Gaussian processes and nonstationary Fourier features.” *Spatial Statistics*, 28: 59–78. 13, 22, 32
- Townes, F. W. (2020). “Review of Probability Distributions for Modeling Count Data.” *arXiv*. 6
- United States Census Bureau (2018). “Age and Sex American Community Survey by U.S States, 2018 Census.” Available at <https://www.census.gov/data.html>. 4
- Unwin, H. J. T., Mishra, S., Bradley, V. C., Gandy, A., Mellan, T. A., Coupland, H., Ish-Horowicz, J., Vollmer, M. A. C., Whittaker, C., Filippi, S. L., Xi, X., Monod, M., Ratmann, O., Hutchinson, M., Valka, F., Zhu, H., Hawryluk, I., Milton, P., Ainslie, K. E. C., Baguelin, M., Boonyasiri, A., Brazeau, N. F., Cattarino, L., Cucunuba, Z., Cuomo-Dannenburg, G., Dorigatti, I., Eales, O. D., Eaton, J. W., van Elsland, S. L., FitzJohn, R. G., Gaythorpe, K. A. M., Green, W., Hinsley, W., Jeffrey, B., Knock, E., Laydon, D. J., Lees, J., Nedjati-Gilani, G., Nouvellet, P., Okell, L., Parag, K. V., Siveroni, I., Thompson, H. A., Walker, P., Walters, C. E., Watson, O. J., Whittles, L. K., Ghani, A. C., Ferguson, N. M., Riley, S., Donnelly, C. A., Bhatt, S., and Flaxman, S. (2020). “State-level tracking of COVID-19 in the United States.” *Nature Communications*, 11(1). 21
- Vehtari, A., Gelman, A., and Gabry, J. (2016). “Practical Bayesian model evaluation

using leave-one-out cross-validation and WAIC.” *Statistics and Computing*, 27(5): 1413–1432. [12](#)

Wadhera, R. K., Wadhera, P., Gaba, P., Figueroa, J. F., Maddox, K. E. J., Yeh, R. W., and Shen, C. (2020). “Variation in COVID-19 Hospitalizations and Deaths Across New York City Boroughs.” *JAMA*, 323(21): 2192. [22](#)

Wilson, A. G., Gilboa, E., Nehorai, A., and Cunningham, J. P. (2014). “Fast Kernel Learning for Multidimensional Pattern Extrapolation.” *Proceedings of the 27th International Conference on Neural Information Processing Systems - Volume 2*, 3626–3634. [2](#), [7](#)

### **Acknowledgments**

We acknowledge funding from the Imperial College COVID-19 Response Fund and the EPSRC through the EPSRC Centre for Doctoral Training in Modern Statistics and Statistical Machine Learning and EP/V002910/1. S. Bhatt acknowledges The UK Research and Innovation (MR/V038109/1), the Academy of Medical Sciences Springboard Award (SBF004/1080), The MRC (MR/R015600/1), The BMGF (OPP1197730), Imperial College Healthcare NHS Trust-BRC Funding (RDA02), The Novo Nordisk Young Investigator Award (NNF20OC0059309) and The NIHR Health Protection Research Unit in Modelling Methodology. O. Ratmann acknowledges the Bill & Melinda Gates Foundation (OPP1175094).

# Supplementary Materials

Supplementary Materials to Regularised B-splines projected Gaussian Process priors to estimate the age profile of COVID-19 deaths before and after vaccine roll-out by Monod et al.

## Contents

|  |    |
|--|----|
| S1 Supplementary Figures and Tables . . . . .  | 30 |
| S2 Modelling COVID-19 weekly deaths . . . . .  | 39 |
| S2.1 Finding weekly death count from censored and missing cumulative death<br>count . . . . .                    | 39 |
| S2.2 Likelihood form . . . . .   | 41 |
| S3 B-splines and properties of the regularised B-splines projected Gaussian Pro-<br>cess prior . . . . .         | 43 |
| S3.1 Construction of a B-spline curve and a B-spline surface . . . . .   | 43 |
| S3.2 Proof that a base kernel function projected with cubic B-splines is a $\mathcal{C}^2$<br>function . . . . . | 44 |
| S4 State level summary . . . . .   | 47 |

## S1 Supplementary Figures and Tables

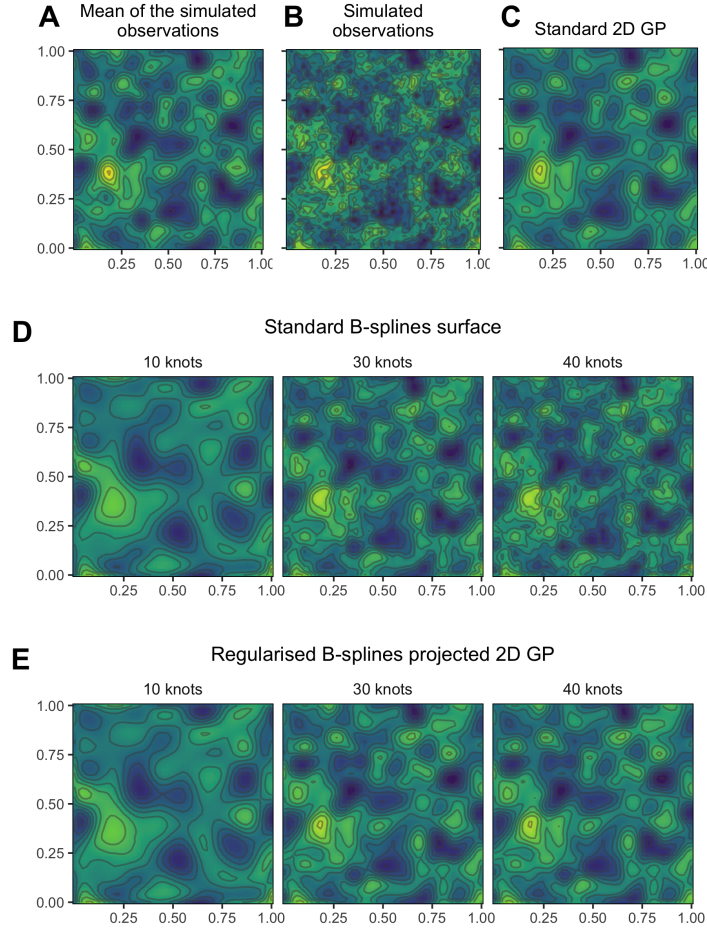


Figure S1: **Simulated 2D observations and posterior mean estimated by three spatial models.** (A) Observations were simulated using a 2D Gaussian process with a squared exponential kernel implying a weak correlation ( $\gamma = 0.01$ ) perturbed with Gaussian noise on the top. The posterior mean of the surface estimated by three models is compared, (B) Standard 2D Gaussian Process (C) Standard B-splines surface (D) low-rank 2D Gaussian Process projected with regularised B-splines.

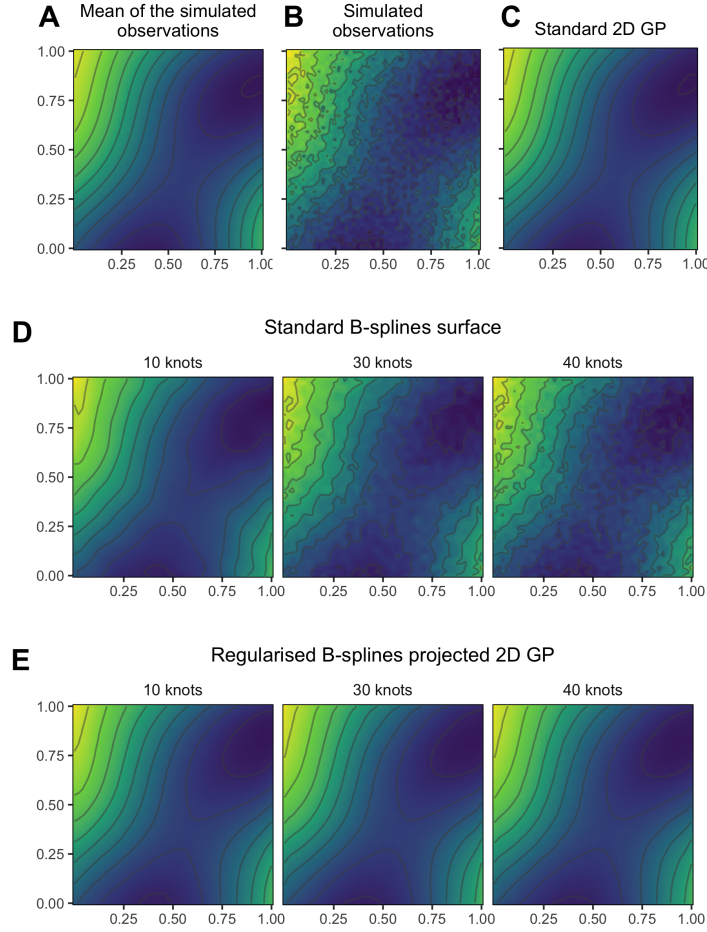


Figure S2: **Simulated 2D observations and posterior mean estimated by three spatial models.** (A) Observations were simulated using a 2D Gaussian process with a squared exponential kernel implying a strong correlation ( $\gamma = 1$ ) perturbed with Gaussian noise on the top. The posterior mean of the surface estimated by three models is compared, (B) Standard 2D Gaussian Process (C) Standard B-splines surface (D) low-rank 2D Gaussian Process projected with regularised B-splines.

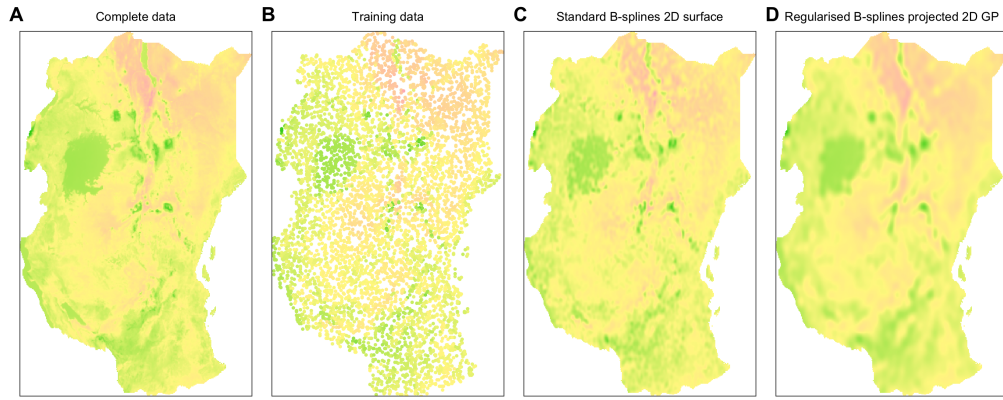


Figure S3: **Deviation in land surface temperature for East Africa trained on 6000 random uniformly chosen locations.** (A) Complete data (Ton et al., 2018). (B) Training data, similar as the one used in Mishra et al. (2020). The remaining subfigures show the estimated posterior mean surface, obtained by two models, (C) a standard B-splines surface, and (D) a regularised B-splines projected 2D GP.



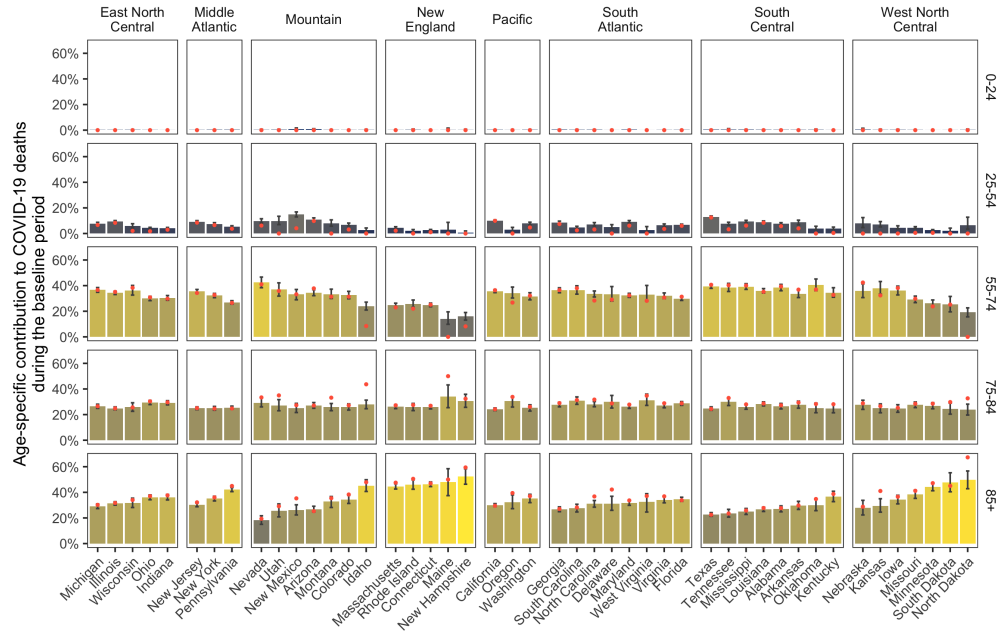


Figure S4: **Estimated and empirical contribution of age groups to COVID-19 attributable deaths in the first 3 months of state epidemics.** Posterior median estimates of each age group to COVID-19 attributable deaths are shown for each state (barplot), along with 95% credible intervals (error bars). Estimates are for the 3 months after the 10th cumulative death in each state, and are not adjusted for differences in the age composition of state populations. Brighter colors indicate higher values of the baseline contribution and darker colors indicate lower values. The empirical estimates (cyan points) of contribution are calculated by setting the non-retrievable weekly deaths to zero. Notice that the contribution from individuals aged 85+ estimated by the model is always lower or equal than the empirical contribution while the one in 50-84 is always greater or equal. This is because the empirical contributions were computed considering that unretrievable weekly deaths were null while they could, in fact, be positive. In particular, we see the benefit of taking our approach for the contribution from individuals aged 55 – 74 in Maine and North Dakota. They were empirically computed to be null, because the weekly deaths were non-retrievable, but they are estimated to be positive with our model. And the estimated values are consistent with the values of the other states, while the empirical values were not.

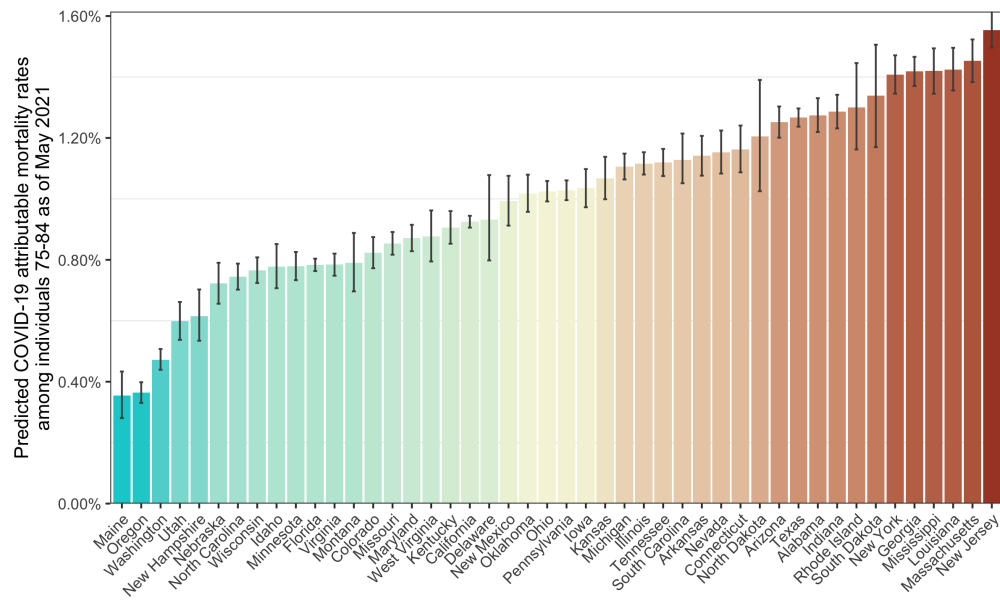


Figure S5: **Predicted, COVID-19 attributable mortality rates among individuals aged 75-84.** Posterior median estimates of the mortality rate (barplot) and 95% credible intervals (error bars) are presented.

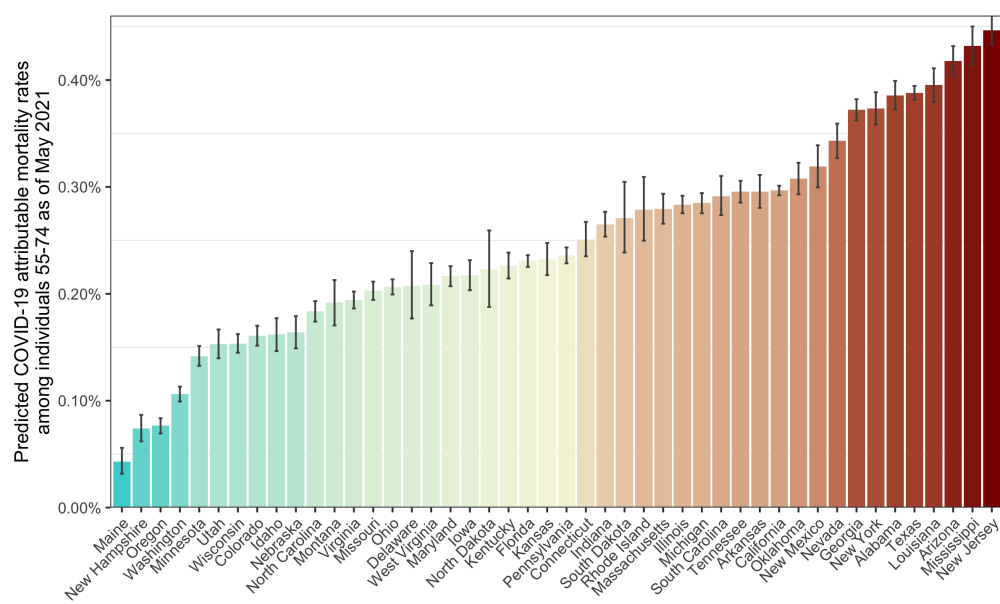


Figure S6: **Predicted, COVID-19 attributable mortality rates among individuals aged 55-74.** Posterior median estimates of the mortality rate (barplot) and 95% credible intervals (error bars) are presented.

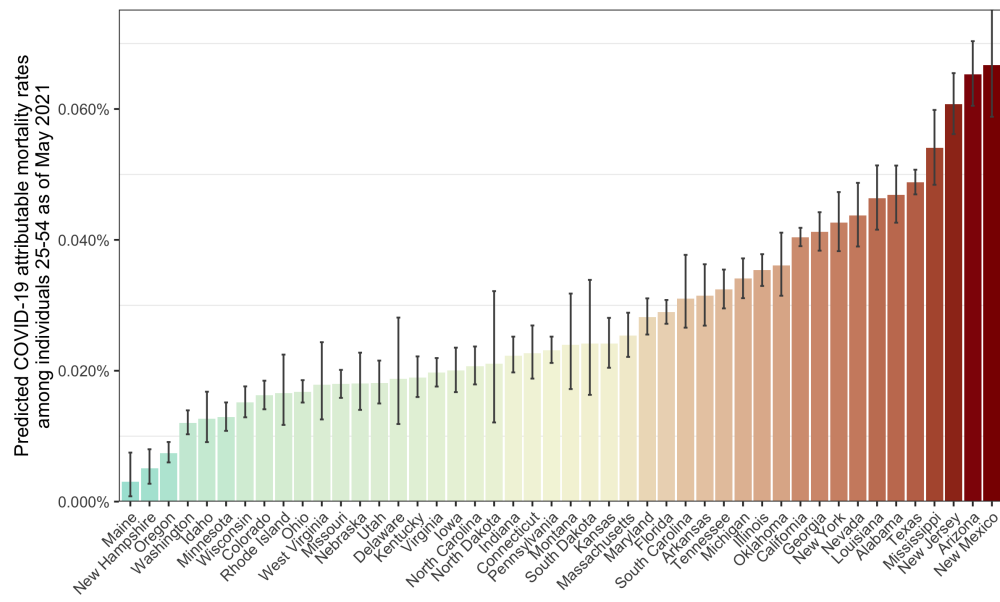
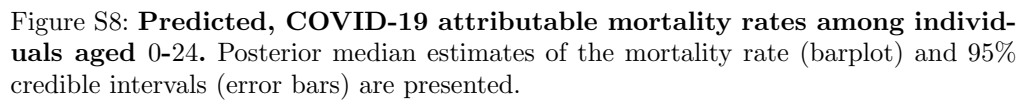


Figure S7: **Predicted, COVID-19 attributable mortality rates among individuals aged 25-54.** Posterior median estimates of the mortality rate (barplot) and 95% credible intervals (error bars) are presented.



| State          | Prior                       |                             |                                       |
|----------------|-----------------------------|-----------------------------|---------------------------------------|
|                | Standard 2D GP              | Standard B-splines surface  | Regularised B-splines projected 2D GP |
|                | %DoH observations inside CI | %DoH observations inside CI | %DoH observations inside CI           |
| Alabama        | 90.74%                      | 91.48%                      | 91.11%                                |
| Arizona        | 96.36%                      | 95.00%                      | 95.91%                                |
| Arkansas       | 91.45%                      | 92.11%                      | 91.45%                                |
| California     | 84.09%                      | 84.66%                      | 84.66%                                |
| Colorado       | 88.65%                      | 91.06%                      | 87.68%                                |
| Connecticut    | 90.37%                      | 93.09%                      | 91.11%                                |
| Delaware       | 95.83%                      | 96.59%                      | 94.70%                                |
| Florida        | 94.35%                      | 95.00%                      | 93.70%                                |
| Georgia        | 92.59%                      | 95.56%                      | 92.10%                                |
| Idaho          | 96.15%                      | 97.76%                      | 96.15%                                |
| Illinois       | 94.32%                      | 96.88%                      | 92.90%                                |
| Indiana        | 93.18%                      | 95.74%                      | 92.33%                                |
| Iowa           | 89.30%                      | 93.02%                      | 87.44%                                |
| Kansas         | 93.75%                      | 95.00%                      | 93.50%                                |
| Kentucky       | 97.22%                      | 96.72%                      | 95.45%                                |
| Louisiana      | 98.05%                      | 99.35%                      | 96.43%                                |
| Maine          | 95.24%                      | 95.83%                      | 95.83%                                |
| Maryland       | 95.71%                      | 97.98%                      | 95.96%                                |
| Massachusetts  | 91.11%                      | 94.17%                      | 90.56%                                |
| Michigan       | 92.39%                      | 95.65%                      | 90.22%                                |
| Minnesota      | 92.31%                      | 98.90%                      | 95.60%                                |
| Mississippi    | 97.52%                      | 98.14%                      | 98.14%                                |
| Missouri       | 90.91%                      | 94.03%                      | 90.34%                                |
| Nevada         | 92.81%                      | 93.75%                      | 92.50%                                |
| New Hampshire  | 97.78%                      | 98.06%                      | 97.78%                                |
| New Jersey     | 93.38%                      | 96.52%                      | 93.03%                                |
| New Mexico     | 98.06%                      | 98.06%                      | 97.50%                                |
| North Carolina | 93.02%                      | 92.64%                      | 91.86%                                |
| North Dakota   | 95.68%                      | 96.91%                      | 95.68%                                |
| Oklahoma       | 90.70%                      | 90.31%                      | 89.15%                                |
| Oregon         | 97.02%                      | 97.83%                      | 96.48%                                |
| Pennsylvania   | 83.68%                      | 97.20%                      | 85.55%                                |
| Rhode Island   | 94.36%                      | 97.18%                      | 94.36%                                |
| South Carolina | 97.22%                      | 98.48%                      | 96.46%                                |
| Tennessee      | 95.80%                      | 97.28%                      | 94.32%                                |
| Texas          | 96.61%                      | 97.92%                      | 96.09%                                |
| Utah           | 97.44%                      | 96.70%                      | 97.07%                                |
| Virginia       | 95.65%                      | 97.10%                      | 94.93%                                |
| Washington     | 92.80%                      | 93.18%                      | 91.29%                                |
| Wisconsin      | 95.43%                      | 98.26%                      | 94.35%                                |
| Average        | 93.73%                      | 95.53%                      | 93.29%                                |

Table S1: **Percent of empirical age-specific contribution to COVID-19 weekly deaths reported by DoH inside the credible interval of the observational age-specific contribution estimated by our model under three priors.** Estimated observational age-specific contribution is calculated from the proportions of the predicted weekly counts.

## S2 Modelling COVID-19 weekly deaths

### S2.1 Finding weekly death count from censored and missing cumulative death count

We denote by  $\mathcal{W}^{\text{cum}} = \{1, \dots, W^{\text{cum}}\}$  the set of week indices from the first to the last reported cumulative deaths by the CDC. The reports span from May 2 2020 to May 22 2021 such that  $W^{\text{cum}} = 56$ . We denote by  $D_{m,b,w}$  the reported cumulative deaths by the CDC in state  $m$  for age group  $b$  in week  $w$ . The cumulative deaths count  $D_{m,b,w}$  is reported if the count is 0 or strictly greater than 9, and otherwise it is censored. For simplicity we suppress the state index in what follows, with all equations being analogous. We denote by  $\mathcal{W}_b^{\text{censored}}$  the set of weeks where  $D_{b,w}$  has been censored.

For a given age group  $b$ , if  $D_{b,w}$  is reported on weeks  $w$  and  $w+1$ , we find the weekly deaths among age group  $b$  in week  $w$   $d_{b,w}$  with the first order difference,

$$d_{b,w} = D_{b,(w+1)} - D_{b,w} \quad (\text{S2.1})$$

The weekly deaths that are retrievable from the first order difference are defined as “retrievable” and the set of week indices for which we can retrieve the weekly deaths is denoted by  $\mathcal{W}_b^{\text{WR}}$  (WR := Week Retrievable). However, if  $D_{b,w}$  is not reported for  $w$  or  $w+1$ , the first-order difference is not obtainable and the weekly deaths is said to be “non-retrievable”. We denote by  $\mathcal{W}_b^{\text{WNR}}$  the set of week indices for which we cannot retrieve the weekly deaths (WNR := Week non-retrievable), with  $\mathcal{W}_b^{\text{WR}} \cap \mathcal{W}_b^{\text{WNR}} = \emptyset$ . Notice that for a fixed age group  $b$ , weekly deaths are non-retrievable for a joint sequence of weeks over time, and importantly this period can happen only once (because the cumulative deaths are strictly increasing). Therefore, we consider the sequence of non-retrievable weekly deaths for a fixed age group together. Because the boundaries of the censored cumulative death are known, we can obtain the boundaries of the sum of the non-retrievable weekly deaths sequence. Let us denote by  $w_b^{\text{FC}}$  the first week when the cumulative death count is censored (FC := First Censored). Such that,

$$w_b^{\text{FC}} = \begin{cases} \min(\mathcal{W}_b^{\text{censored}}) & \text{if } \mathcal{W}_b^{\text{censored}} \neq \emptyset \\ \text{does not exist} & \text{otherwise.} \end{cases} \quad (\text{S2.2})$$

Similarly, we denote by  $w_b^{\text{FNC}}$  the first week when the cumulative death count is observed after being censored (FNC := First Non Censored). Such that,

$$w_b^{\text{FNC}} = \begin{cases} \max(\mathcal{W}_b^{\text{censored}}) + 1 & \text{if } \max(\mathcal{W}_b^{\text{censored}}) < W^{\text{cum}} \\ \text{does not exist} & \text{otherwise.} \end{cases} \quad (\text{S2.3})$$

Four different scenarios may apply.

1. If  $D_{b,w}$  is censored for some weeks  $w \in \mathcal{W}^{\text{cum}}$  but is observed on the first and the last weeks (i.e.,  $w = 1$  and  $w = W^{\text{cum}}$ ), the non-retrievable weekly deaths must sum to the first positive cumulative deaths, such that,

$$\sum_{w \in \mathcal{W}_b^{\text{WNR}}} d_{b,w} = D_{b,w_b^{\text{FNC}}}. \quad (\text{S2.4})$$



where  $\mathcal{W}_b^{\text{WNR}} = \{(w_b^{\text{FC}} - 1), \mathcal{W}_b^{\text{censored}}\}$ . In this case,  $\mathcal{W}_b^{\text{WR}} = \{1, \dots, (w_b^{\text{FC}} - 2), w_b^{\text{FNC}}, \dots, (W^{\text{cum}} - 1)\}$ . We show an example of this scenario in Table S2.

2. If  $D_{b,w}$  is censored for some weeks  $w \in \mathcal{W}^{\text{cum}}$ , including the first week (i.e.,  $w = 1$ ), but is observed for the last week (i.e.,  $w = W^{\text{cum}}$ ), the sum of non-retrievable weekly deaths must be between,

$$D_{b,w_b^{\text{FNC}}} - 9 \leq \sum_{w \in \mathcal{W}_b^{\text{WNR}}} d_{b,w} \leq D_{b,w_b^{\text{FNC}}} - 1. \quad (\text{S2.5})$$

where  $\mathcal{W}_b^{\text{WNR}} = \mathcal{W}_b^{\text{censored}}$ . In this case,  $\mathcal{W}_b^{\text{WR}} = \{w_b^{\text{FNC}}, \dots, (W^{\text{cum}} - 1)\}$ . We show an example of this scenario in Table S3.

3. If  $D_{b,w}$  is censored for some weeks  $w \in \mathcal{W}^{\text{cum}}$ , including the last week (i.e.,  $w = W^{\text{cum}}$ ), but is observed for the first week (i.e.,  $w = 1$ ), the sum of the non-retrievable weekly deaths must be between,

$$1 \leq \sum_{w \in \mathcal{W}_b^{\text{WNR}}} d_{b,w} \leq 9 \quad (\text{S2.6})$$

where  $\mathcal{W}_b^{\text{WNR}} = \{(w_b^{\text{FC}} - 1), \mathcal{W}_b^{\text{censored}} \setminus W^{\text{cum}}\}$ . In this case,  $\mathcal{W}_b^{\text{WR}} = \{1, \dots, (w_b^{\text{FC}} - 2)\}$ . Notice that  $D_{b,w_b^{\text{FNC}}}$  does not exist. We show an example of this scenario in Table S4.

4. Lastly, if  $D_{b,w}$  is censored for all weeks  $w \in \mathcal{W}^{\text{cum}}$ , including the first week (i.e.,  $w = 1$ ) and the last week (i.e.,  $w = W^{\text{cum}}$ ), the sum of the non-retrievable weekly deaths must be between,

$$0 \leq \sum_{w \in \mathcal{W}_b^{\text{WNR}}} d_{b,w} \leq 8 \quad (\text{S2.7})$$

where  $\mathcal{W}_b^{\text{WNR}} = \{\mathcal{W}_b^{\text{censored}} \setminus W^{\text{cum}}\}$ . In this case,  $\mathcal{W}_b^{\text{WR}} = \emptyset$ . Notice that  $D_{b,w_b^{\text{FNC}}}$  does not exist. We show an example of this scenario in Table S5.

The CDC did not publish a report on July 4 2020, such that the cumulative deaths in the corresponding week are not available. We denote this week by  $w^{\text{missing}}$ . The weekly deaths could not be obtained for the missing week or the week before, such that,  $\mathcal{W}_b^{\text{WR}} \cup \mathcal{W}_b^{\text{WNR}} = \mathcal{W}^{\text{cum}} \setminus \{w^{\text{missing}} - 1, w^{\text{missing}}, W^{\text{cum}}\}$ . Weekly deaths that occurred on those  $w^{\text{missing}}$  and  $w^{\text{missing}} - 1$  are defined to be missing. It is important to note the difference between non-retrievable weekly deaths, for which we have information through the censoring of cumulative deaths, and missing weekly deaths for which no information has been provided. Note that if the index of the missing week  $w^{\text{missing}}$  and the week before  $w^{\text{missing}} - 1$ , are in between the range of  $\mathcal{W}_b^{\text{censored}}$ , or are before or after the set's limits, they are included in  $\mathcal{W}_b^{\text{censored}}$ , with all inequations still holding.

| $w$   | 1 | 2 | 3  | 4  | 5  |
|-------|---|---|----|----|----|
| $D_w$ | 0 | 0 | NA | NA | 11 |
| $d_w$ | 0 |   | 11 |    | -  |

Table S2: **Finding weekly death when  $D_w$  is censored as in scenario 1.** In this example  $\mathcal{W}^{\text{censored}} = \{3, 4\}$ ,  $w^{\text{FC}} = 3$ ,  $w^{\text{FNC}} = 5$ ,  $\mathcal{W}^{\text{WNR}} = \{2, 3, 4\}$  and  $\mathcal{W}^{\text{WR}} = \{1\}$ . From (S2.4), we know that  $\sum_{w \in \mathcal{W}^{\text{WNR}}} d_w = 11$ .

| $w$   | 1  | 2      | 3  | 4  | 5  |
|-------|----|--------|----|----|----|
| $D_w$ | NA | NA     | NA | 11 | 11 |
| $d_w$ |    | [2-10] |    | 0  | -  |

Table S3: **Finding weekly death when  $D_w$  is censored as in scenario 2.** In this example  $\mathcal{W}^{\text{censored}} = \{1, 2, 3\}$ ,  $w^{\text{FC}} = 1$ ,  $w^{\text{FNC}} = 4$ ,  $\mathcal{W}^{\text{WNR}} = \{1, 2, 3\}$  and  $\mathcal{W}^{\text{WR}} = \{4\}$ . From (S2.5), we know that  $2 \leq \sum_{w \in \mathcal{W}^{\text{WNR}}} d_w \leq 10$ .

| $w$   | 1 | 2 | 3     | 4  | 5  |
|-------|---|---|-------|----|----|
| $D_w$ | 0 | 0 | NA    | NA | NA |
| $d_w$ | 0 |   | [1-9] |    | -  |

Table S4: **Finding weekly death when  $D_w$  is censored as in scenario 3.** In this example  $\mathcal{W}^{\text{censored}} = \{3, 4, 5\}$ ,  $w^{\text{FC}} = 3$ ,  $w^{\text{FNC}}$  does not exist,  $\mathcal{W}^{\text{WNR}} = \{2, 3, 4\}$  and  $\mathcal{W}^{\text{WR}} = \{1\}$ . From (S2.6), we know that  $1 \leq \sum_{w \in \mathcal{W}^{\text{WNR}}} d_w \leq 9$ .

| $w$   | 1  | 2  | 3     | 4  | 5  |
|-------|----|----|-------|----|----|
| $D_w$ | NA | NA | NA    | NA | NA |
| $d_w$ |    |    | [0-8] |    | -  |

Table S5: **Finding weekly death when  $D_w$  is censored as in scenario 4.** In this example  $\mathcal{W}^{\text{censored}} = \{1, 2, 3, 4, 5\}$ ,  $w^{\text{FC}} = 1$ ,  $w^{\text{FNC}}$  does not exist,  $\mathcal{W}^{\text{WNR}} = \{1, 2, 3, 4\}$  and  $\mathcal{W}^{\text{WR}} = \emptyset$ . From (S2.7), we know that  $0 \leq \sum_{w \in \mathcal{W}^{\text{WNR}}} d_w \leq 8$ .

## S2.2 Likelihood form

The log likelihood is,

$$\log \mathcal{L} = \sum_{b \in \mathcal{B}} \sum_{w \in \mathcal{W}_b^{\text{WR}}} \log p(d_{b,w} ; \alpha_{b,w}, \theta) \quad (\text{S2.8a})$$

$$+ \sum_{b \in \mathcal{B}} \log p(\{d_{b,w}\}_{w \in \mathcal{W}_b^{\text{WNR}}} ; \{\alpha_{b,w}\}_{w \in \mathcal{W}_b^{\text{WNR}}}, \theta), \quad (\text{S2.8b})$$

The log likelihood for the retrievable weekly deaths in (S2.8a) is

$$\log p(d_{b,w} ; \alpha_{b,w}, \theta) = \log \text{NegBin}(d_{b,w} ; \alpha_{b,w}, \theta). \quad (\text{S2.9})$$

The log likelihood for the non-retrievable weekly deaths in (S2.8b) is

$$p(\{d_{b,w}\}_{w \in \mathcal{W}_b^{\text{WNR}}} ; \{\alpha_{b,w}\}_{w \in \mathcal{W}_b^{\text{WNR}}}, \theta) = p\left(\sum_{w \in \mathcal{W}_b^{\text{WNR}}} d_{b,w} ; \sum_{w \in \mathcal{W}_b^{\text{WNR}}} \alpha_{b,w}, \theta\right)$$

$$\left\{ \begin{array}{ll}
\text{NegBin}\left(D_{b,w_b^{\text{FNC}}} ; \sum_{w \in \mathcal{W}_b^{\text{WNR}}} \alpha_{b,w}, \theta\right) & \text{if } 1, W^{\text{cum}} \notin \mathcal{W}_b^{\text{censored}} \\
\text{Cdf NegBin}\left(D_{bw_b^{\text{FNC}}} - 1 ; \sum_{w \in \mathcal{W}_b^{\text{WNR}}} \alpha_{b,w}, \theta\right) & \text{if } 1 \in \mathcal{W}_b^{\text{censored}} \\
-\text{Cdf NegBin}\left(D_{bw_b^{\text{FNC}}} - 9 ; \sum_{w \in \mathcal{W}_b^{\text{WNR}}} \alpha_{b,w}, \theta\right) & \text{and } W^{\text{cum}} \notin \mathcal{W}_b^{\text{censored}} \\
\text{Cdf NegBin}\left(9 ; \sum_{w \in \mathcal{W}_b^{\text{WNR}}} \alpha_{b,w}, \theta\right) & \text{if } 1 \notin \mathcal{W}_b^{\text{censored}} \\
-\text{Cdf NegBin}\left(1 ; \sum_{w \in \mathcal{W}_b^{\text{WNR}}} \alpha_{b,w}, \theta\right) & \text{and } W^{\text{cum}} \in \mathcal{W}_b^{\text{censored}} \\
\text{Cdf NegBin}\left(8 ; \sum_{w \in \mathcal{W}_b^{\text{WNR}}} \alpha_{b,w}, \theta\right) & \text{if } 1, W^{\text{cum}} \in \mathcal{W}_b^{\text{censored}} \\
-\text{Cdf NegBin}\left(0 ; \sum_{w \in \mathcal{W}_b^{\text{WNR}}} \alpha_{b,w}, \theta\right) & 
\end{array} \right. \quad (\text{S2.10})$$

where the boundaries for the different scenarios have been discussed in Section S2.1. Note that to find (S2.10), we used the fact that the sum of independent negative-binomially distributed random variables with shape parameter  $\alpha_1$  and  $\alpha_2$ , and with the same scale parameter  $\theta$  is negative-binomially distributed with a scale parameter  $\theta$  and with a shape parameter  $\alpha_1 + \alpha_2$ .

## S3 B-splines and properties of the regularised B-splines projected Gaussian Process prior

### S3.1 Construction of a B-spline curve and a B-spline surface

We start this section by constructing a B-spline basis function, also called B-spline segment, which we refer to as B-spline. A B-spline is entirely defined by a polynomial degree,  $d$ , and a non-decreasing sequence of knots  $(t_1 \leq \dots \leq t_K)$  spanning in  $\mathcal{X}^* \subseteq \mathbb{R}$ , where  $K$  is the number of knots. For the B-spline to cover the entire span of knots, the sequence of knots has to be extended on the left ( $d$  times) and on the right ( $d$  times),  $(\xi_1 \leq \dots \leq \xi_d \leq \xi_{d+1} \leq \dots \leq \xi_{d+K} \leq \xi_{d+K+1} \leq \dots \leq \xi_{2d+K+1})$ , where  $\xi_{d+1} := t_1, \dots, \xi_{d+K} := t_K$ . The value of the additional knots is generally set to the boundary knots (Perperoglou et al., 2019). The order of a B-spline, denoted by  $o$ , is equal to  $d+1$ . A B-spline of order  $o$ , written  $B_{p,o}(x)$ , is defined by the recursive formula,

$$B_{p,0}(x) = \begin{cases} 1 & \text{if } \xi_p \leq x < \xi_{p+1}, \\ 0 & \text{otherwise} \end{cases} \quad (\text{S3.1})$$

$$B_{p,o}(x) = \frac{x - \xi_p}{\xi_{p+o} - \xi_p} B_{p,o-1}(x) + \frac{\xi_{p+o+1} - x}{\xi_{p+o+1} - \xi_{p+1}} B_{p+1,o-1}(x) \quad (\text{S3.2})$$

and  $B_{p,0}(x) = 0$  if  $\xi_p = \xi_{p+1}$  for  $x \in \mathcal{X}^* \subseteq \mathbb{R}$  and  $p = 1, \dots, P$  with  $P = K + d - 1$ . The above is usually referred to as the Cox-de Boor recursion formula (d. Boor, 1978). We define the ensemble of B-spline indices by  $\tilde{\mathbf{X}} \triangleq (\tilde{x}^1, \dots, \tilde{x}^P) = (1, \dots, P)$ .

Let us define  $\mathcal{C}^k(A; B)$  as the set of  $\mathcal{C}^k$  functions from  $A$  to  $B$ .

**Proposition 1.** *Let a B-spline of degree  $d$ , constructed in (S3.1) given a vector of strictly increasing sequence knots (no knot occurs more than 1 time), spanning over  $\mathcal{X}^*$ . Then, the B-spline is a  $C^{d-1}(\mathcal{X}^*; \mathbb{R}^+)$ .*

*Proof.* Recall from Goldman (2002) that a B-spline of degree  $d$ , constructed in (S3.1) given a vector of strictly increasing sequence knots, spanning over  $\mathcal{X}^*$  is of continuity  $C^\infty(\mathcal{X}^*; \mathbb{R}^+)$  piecewise, and of continuity  $C^{d-1}(\mathcal{X}^*; \mathbb{R}^+)$  on the knots. Therefore, the same B-spline is  $C^{d-1}(\mathcal{X}^*; \mathbb{R}^+)$  everywhere.  $\square$

Next, we construct a B-splines curve of degree  $d$ , a linear combination of control points and B-splines of degree  $d$ , given by,

$$\sum_{\tilde{x} \in \tilde{\mathbf{X}}} \beta_{\tilde{x}} B_{\tilde{x},d-1}(x) \quad (\text{S3.3})$$

where  $\beta = [\beta_{\tilde{x}}]_{\tilde{x} \in \tilde{\mathbf{X}}}$  are the associated B-spline coefficients, also referred to as control points or de Boor points.

The surface analogue to the B-spline curve is the B-spline surface. The surface is defined on the space  $\mathcal{X}_1^* \times \mathcal{X}_2^*$  with  $\mathcal{X}_1^* \subseteq \mathbb{R}$  and  $\mathcal{X}_2^* \subseteq \mathbb{R}$ . We start by defining two

non decreasing sequences of knots,  $(t_{1,1} \leq \dots \leq t_{1,K_1})$  and  $(t_{2,1} \leq \dots \leq t_{2,K_2})$  placed respectively on the space  $\mathcal{X}_1^*$  and  $\mathcal{X}_2^*$ , where  $K_1$  is the number of knots along the first axis, and  $K_2$  along the second axis. The total number of B-splines on the first axis is  $P_1 = K_1 + d_1 - 1$  and on the second axis it is  $P_2 = K_2 + d_2 - 1$ . We define the ensemble of pairs of B-spline's indices by  $\tilde{\mathbf{X}} \triangleq (\tilde{\mathbf{x}}^1, \dots, \tilde{\mathbf{x}}^P) = ((\tilde{x}_1^1, \tilde{x}_2^1), \dots, (\tilde{x}_1^{P_1}, \tilde{x}_2^{P_2})) = ((1, 1), \dots, (P_1, P_2))$ . The surface is a tensor product defined by a topologically rectangular set of control points  $\beta_{\tilde{\mathbf{x}}} = \beta_{(\tilde{x}_1, \tilde{x}_2)}$  for all  $\tilde{\mathbf{x}} \in \tilde{\mathbf{X}}$ . The corresponding integral of the B-spline surface evaluated at  $x_1 \in \mathcal{X}_1^*$  and,  $x_2 \in \mathcal{X}_2^*$  is given by,

$$\sum_{(\tilde{x}_1, \tilde{x}_2) \in \tilde{\mathbf{X}}} \beta_{(\tilde{x}_1, \tilde{x}_2)} B_{\tilde{x}_1, d_1-1}^1(x_1) B_{\tilde{x}_2, d_2-1}^2(x_2), \quad (\text{S3.4})$$

where  $B_{\tilde{x}_1, d_1-1}^1(\cdot)$  and  $B_{\tilde{x}_2, d_2-1}^2(\cdot)$  are the  $\tilde{x}_1$ th and  $\tilde{x}_2$ th B-splines of degree  $d_1$  and  $d_2$  defined on the space  $\mathcal{X}_1^*$  and  $\mathcal{X}_2^*$ , respectively.

### S3.2 Proof that a base kernel function projected with cubic B-splines is a $\mathcal{C}^2$ function

We follow the notations introduced in Section S3.1 and denote the  $\tilde{x}_1$ th and  $\tilde{x}_2$ th cubic B-spline by  $B_{\tilde{x}_1}^1(x_1)$  and  $B_{\tilde{x}_2}^2(x_2)$ <sup>1</sup> where  $x_1 \in \mathcal{X}_1^* \subseteq \mathbb{R}$  and  $x_2 \in \mathcal{X}_2^* \subseteq \mathbb{R}$ . They are respectively defined by two vectors of strictly increasing knots of lengths  $K_1$  and  $K_2$ . For ease of notation, we define the ensemble of B-spline indices by

$$\tilde{\mathbf{X}} \triangleq ((\tilde{x}_1^1, \tilde{x}_2^1), \dots, (\tilde{x}_1^{P_1}, \tilde{x}_2^{P_2})) = ((1, 1), \dots, (P_1, P_2)), \quad (\text{S3.5})$$

where  $P_1 = K_1 + 2$  and  $P_2 = K_2 + 2$ .

Let us define a covariance matrix  $\mathbf{K}_\beta$  of size  $P_1 P_2 \times P_1 P_2$  obtained by evaluating at every pair of points in  $\tilde{\mathbf{X}}$  a base kernel function  $k_\beta$ ,

$$(\mathbf{K}_\beta)_{(\tilde{x}_1, \tilde{x}_2), (\tilde{x}'_1, \tilde{x}'_2)} = k_\beta((\tilde{x}_1, \tilde{x}_2), (\tilde{x}'_1, \tilde{x}'_2)). \quad (\text{S3.6})$$

We define a covariance matrix projected by cubic B-splines by the linear transformation

$$\mathbf{W} = (\mathbf{B}^2 \otimes \mathbf{B}^1)^T \mathbf{K}_\beta (\mathbf{B}^2 \otimes \mathbf{B}^1) \quad (\text{S3.7})$$

where  $\mathbf{B}^1$  and  $\mathbf{B}^2$  are an ensemble of B-splines evaluated at some points on  $x_1 \in \mathcal{X}_1^*$  and  $x_2 \in \mathcal{X}_2^*$ , respectively. The covariance matrix (S3.7) is obtained by evaluating at every pair of points a kernel function  $w$ ,  $\mathbf{W}_{(x_1, x_2), (x'_1, x'_2)} = w(x_1, x_2, x'_1, x'_2)$  with,

$$w(x_1, x_2, x'_1, x'_2) = \sum_{(\tilde{x}_1, \tilde{x}_2) \in \tilde{\mathbf{X}}} \sum_{(\tilde{x}'_1, \tilde{x}'_2) \in \tilde{\mathbf{X}}} D(x_1, x_2, \tilde{x}_1, \tilde{x}_2) k_\beta(\tilde{x}_1, \tilde{x}_2, \tilde{x}'_1, \tilde{x}'_2) D(x'_1, x'_2, \tilde{x}'_1, \tilde{x}'_2). \quad (\text{S3.8})$$

<sup>1</sup>Notice that we dropped the polynomial degree index as it is fixed to 3.

where  $(x_1, x_2), (x'_1, x'_2) \in \mathcal{X}_1^* \times \mathcal{X}_2^*$ , and

$$D(x_1, x_2, \tilde{x}_1, \tilde{x}_2) = B_{\tilde{x}_2}^2(x_2) B_{\tilde{x}_1}^1(x_1). \quad (\text{S3.9})$$

We repeat here the definition presented in S3.1: we define  $\mathcal{C}^k(A; B)$  as the set of  $\mathcal{C}^k$  functions from  $A$  to  $B$ .

**Proposition 2.** *Let  $w(\cdot)$  be defined as in (S3.8) and  $\mathcal{S} = \mathcal{X}_1^* \times \mathcal{X}_2^* \times \mathcal{X}_1^* \times \mathcal{X}_2^* \subseteq \mathbb{R}^4$ . Then,  $w(\cdot)$  is a  $\mathcal{C}^2(\mathcal{S}; \mathbb{R})$  function.*

*Proof.* In order to show that  $w(x_1, x_2, x'_1, x'_2) \in \mathcal{C}^2(\mathcal{S}; \mathbb{R})$  it is sufficient to show that all its second partial derivatives are continuous functions on  $\mathcal{S}$ . We show this for the case of the partial derivative  $\frac{\partial^2 w}{\partial x_1^2}$  and the mixed derivative  $\frac{\partial^2 w}{\partial x_1 \partial x_2}$ , as the proof for the remaining second partial derivatives is identical. The proof is constructed as follows: (1) we compute  $\frac{\partial^2 w}{\partial x_1^2}$  and  $\frac{\partial^2 w}{\partial x_1 \partial x_2}$  and (2) we show that  $\frac{\partial^2 w}{\partial x_1^2}$  and  $\frac{\partial^2 w}{\partial x_1 \partial x_2}$  are continuous.

*Step (1):* A direct computation shows,

$$\begin{aligned} \frac{\partial^2 w}{\partial x_1^2} = & \sum_{(\tilde{x}_1, \tilde{x}_2) \in \tilde{\mathcal{X}}} \sum_{(x'_1, x'_2) \in \tilde{\mathcal{X}}} B_{\tilde{x}_2}^2(x_2) \frac{\partial^2 B_{\tilde{x}_1}^1}{\partial x_1^2}(x_1) k_\beta(\tilde{x}_1, \tilde{x}_2, \tilde{x}'_1, \tilde{x}'_2) D(x'_1, x'_2, \tilde{x}'_1, \tilde{x}'_2), \quad (\text{S3.10}) \end{aligned}$$

$$\begin{aligned} \frac{\partial w}{\partial x_1 \partial x_2} = & \sum_{(\tilde{x}_1, \tilde{x}_2) \in \tilde{\mathcal{X}}} \sum_{(x'_1, x'_2) \in \tilde{\mathcal{X}}} \frac{\partial B_{\tilde{x}_2}^2}{\partial x_2}(x_2) \frac{\partial B_{\tilde{x}_1}^1}{\partial x_1}(x_1) k_\beta(\tilde{x}_1, \tilde{x}_2, \tilde{x}'_1, \tilde{x}'_2) D(x'_1, x'_2, \tilde{x}'_1, \tilde{x}'_2), \quad (\text{S3.11}) \end{aligned}$$

where we have used the expression of  $D$  as stated in (S3.9) and  $\tilde{\mathcal{X}}$  is defined in (S3.5).

*Step (2):* We show that (S3.10) is a continuous function on  $\mathcal{S}$ . As stated in Proposition 1, the functions  $B_{\tilde{x}_1}^1(\cdot)$  and  $B_{\tilde{x}_2}^2(\cdot)$  are  $\mathcal{C}^2(\mathcal{X}_1^*; \mathbb{R}^+)$  and  $\mathcal{C}^2(\mathcal{X}_2^*; \mathbb{R}^+)$  functions, respectively. Therefore,  $\frac{\partial^2 B_{\tilde{x}_1}^1}{\partial x_1^2}(\cdot)$  and  $B_{\tilde{x}_2}^2(x_2)$  are continuous function on  $\mathcal{X}_1^*$  and  $\mathcal{X}_2^*$ , respectively. Moreover, recall that  $k_\beta$  is a kernel function, so for any fixed  $(\tilde{x}_1, \tilde{x}_2), (\tilde{x}'_1, \tilde{x}'_2) \in \tilde{\mathcal{X}}$ ,  $k_\beta(\tilde{x}_1, \tilde{x}_2, \tilde{x}'_1, \tilde{x}'_2) \in \mathbb{R}$ . By standard results of Multivariate Calculus (Lax and Terrell (2017) Theorem 2.5), for any fixed  $\tilde{x}_1, \tilde{x}_2, \tilde{x}'_1, \tilde{x}'_2$  the term

$$B_{\tilde{x}_2}^2(x_2) \frac{\partial^2 B_{\tilde{x}_1}^1}{\partial x_1^2}(x_1) k_\beta(\tilde{x}_1, \tilde{x}_2, \tilde{x}'_1, \tilde{x}'_2) B_{\tilde{x}_2}^2(x'_2) B_{\tilde{x}'_1}^1(x'_1)$$

is a continuous function from  $\mathcal{S}$  to  $\mathbb{R}$ . Moreover, the RHS of (S3.10) is a linear combination of continuous function from  $\mathcal{S}$  to  $\mathbb{R}$ , therefore it is continuous from  $\mathcal{S}$  to  $\mathbb{R}$ . Hence,  $\frac{\partial^2 w}{\partial x_1^2}$  is a continuous function from  $\mathcal{S}$  to  $\mathbb{R}$ .

Now, we show that (S3.11) is a continuous function on  $\mathcal{S}$ . As stated in Proposition 1, the functions  $B_{\tilde{x}_1}^1(\cdot)$  and  $B_{\tilde{x}_2}^2(\cdot)$  are  $\mathcal{C}^2(\mathcal{X}_1; \mathbb{R}^+)$  and  $\mathcal{C}^2(\mathcal{X}_2; \mathbb{R}^+)$  functions, respectively. Therefore,  $\frac{\partial B_{\tilde{x}_1}^1}{\partial x_1}(\cdot)$  and  $\frac{\partial B_{\tilde{x}_2}^2}{\partial x_2}(\cdot)$  are continuous functions on  $\mathcal{X}_1^*$  and  $\mathcal{X}_2^*$ , respectively. Moreover, recall that  $k_\beta$  is a kernel function, so for any fixed  $(\tilde{x}_1, \tilde{x}_2), (\tilde{x}'_1, \tilde{x}'_2) \in \tilde{\mathbf{X}}$ ,  $k_\beta(\tilde{x}_1, \tilde{x}_2, \tilde{x}'_1, \tilde{x}'_2) \in \mathbb{R}$ . By standard results of Multivariate Calculus (Lax and Terrell (2017) Theorem 2.5), for any fixed  $\tilde{x}_1, \tilde{x}_2, \tilde{x}'_1, \tilde{x}'_2$  the term

$$\frac{\partial B_{\tilde{x}_2}^2}{\partial x_2}(x_2) \frac{\partial B_{\tilde{x}_1}^1}{\partial x_1}(x_1) k_\beta(\tilde{x}_1, \tilde{x}_2, \tilde{x}'_1, \tilde{x}'_2) B_{\tilde{x}_2}^2(x'_2) B_{\tilde{x}_1}^1(x'_1)$$

is a continuous function from  $\mathcal{S}$  to  $\mathbb{R}$ . Moreover, the RHS of (S3.11) is a linear combination of continuous functions on from  $\mathcal{S}$  to  $\mathbb{R}$ , therefore it is continuous from  $\mathcal{S}$  to  $\mathbb{R}$ . Hence,  $\frac{\partial w}{\partial x_1 \partial x_2}$  is a continuous function from  $\mathcal{S}$  to  $\mathbb{R}$ .

The proof for the other terms follows from a similar argument, with the necessary replacement of sets and functions. Therefore  $w(\cdot)$  is a  $\mathcal{C}^2(\mathcal{S}; \mathbb{R})$  function.  $\square$



## S4 State level summary

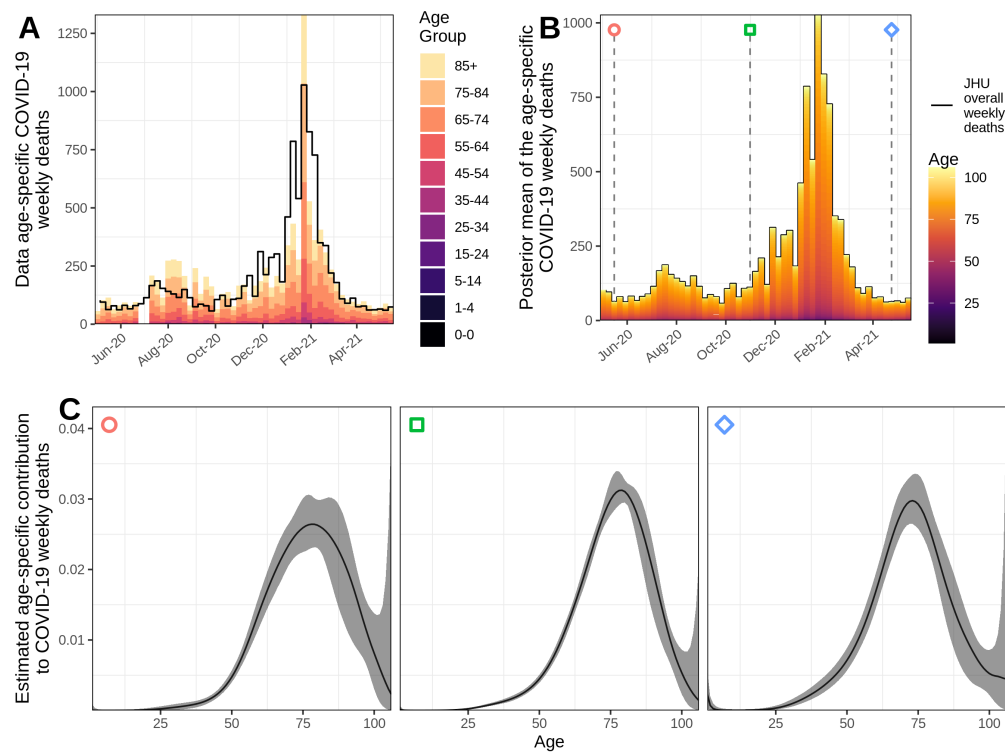


Figure S9: State summary for Alabama.

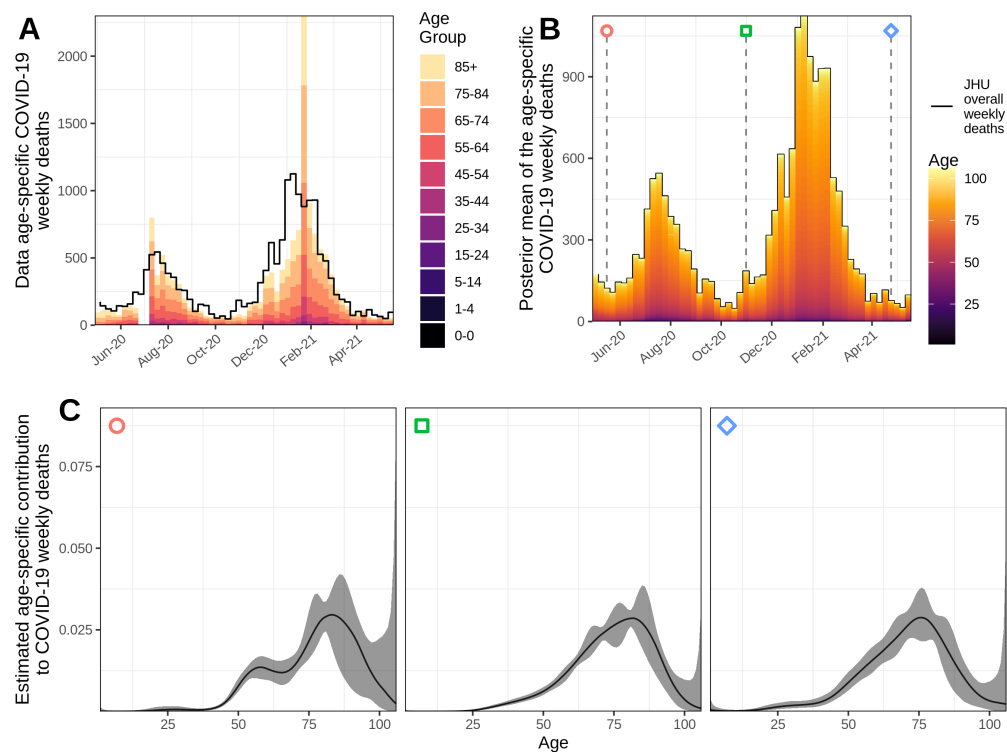


Figure S10: State summary for Arizona.

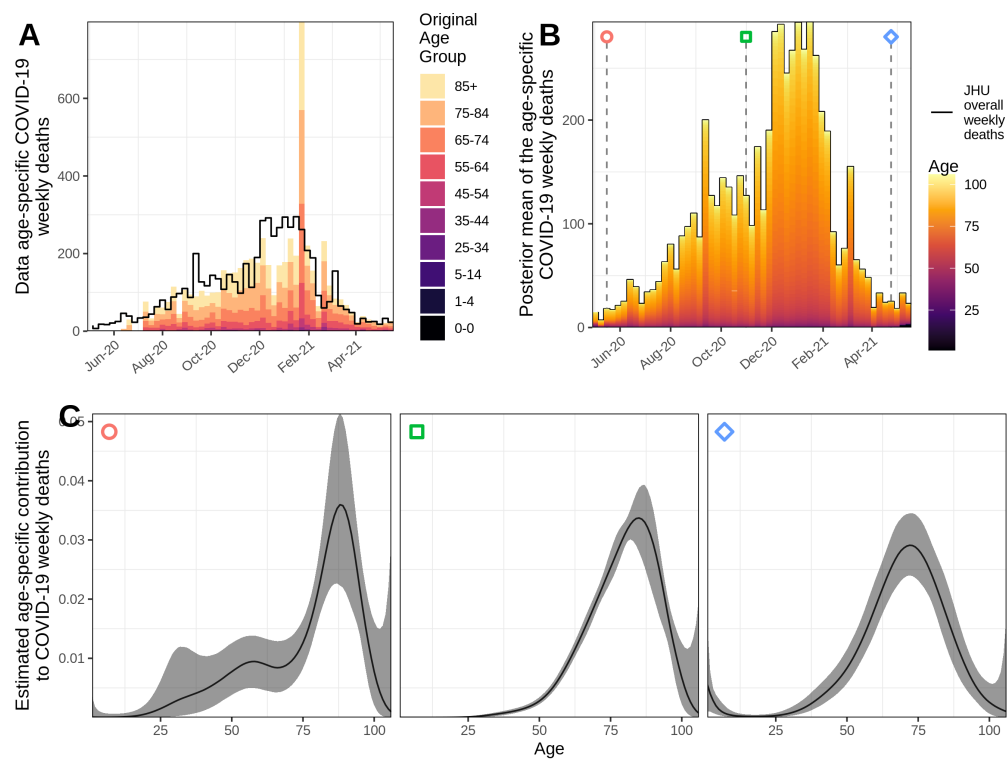
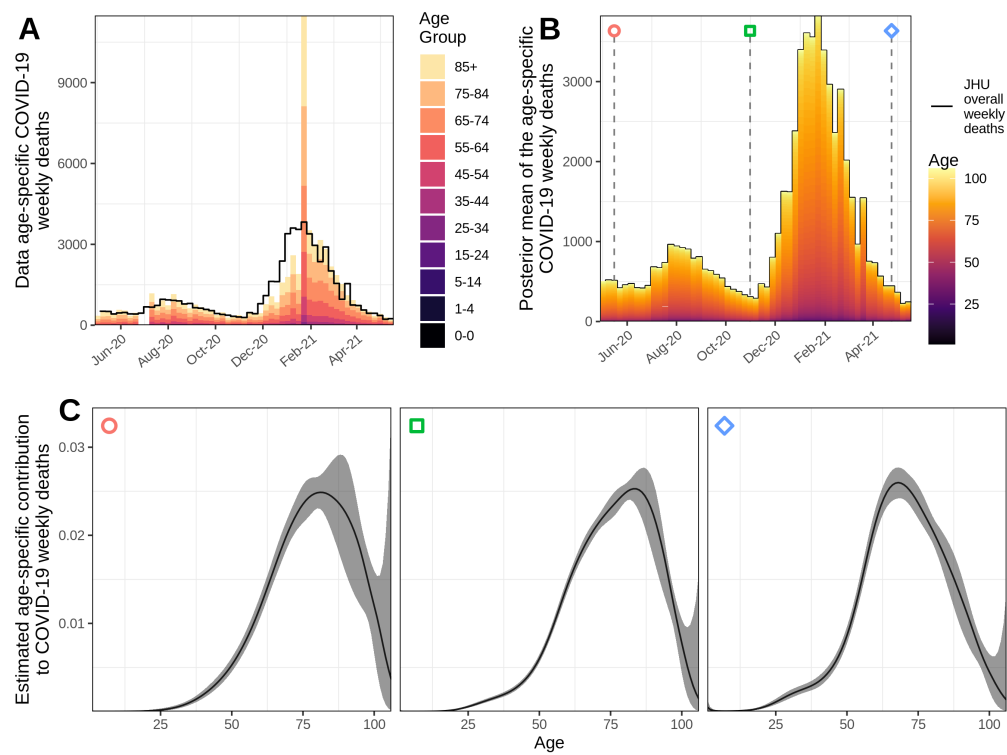


Figure S11: State summary for Arkansas.

Figure S12: **State summary for California.**

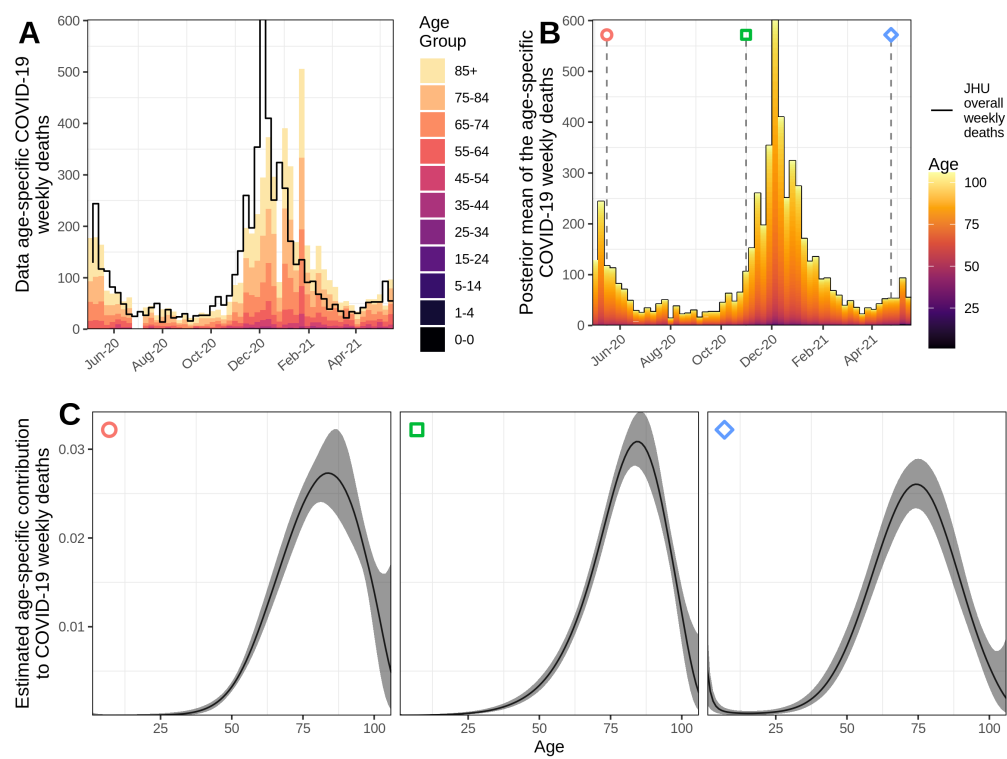


Figure S13: State summary for Colorado.

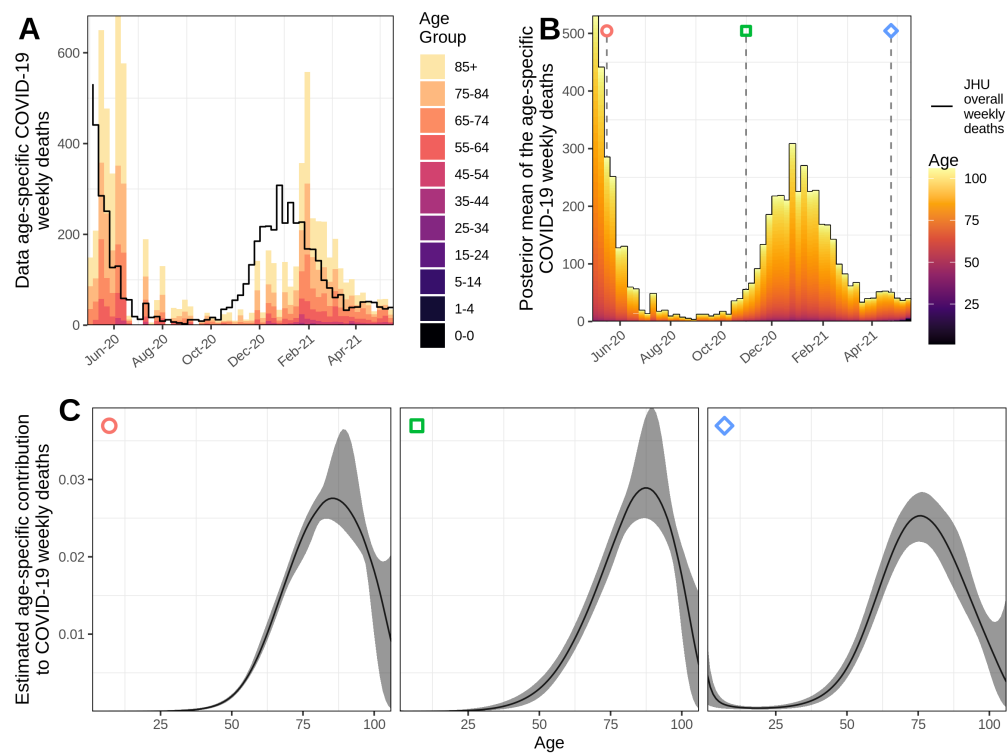


Figure S14: State summary for Connecticut.

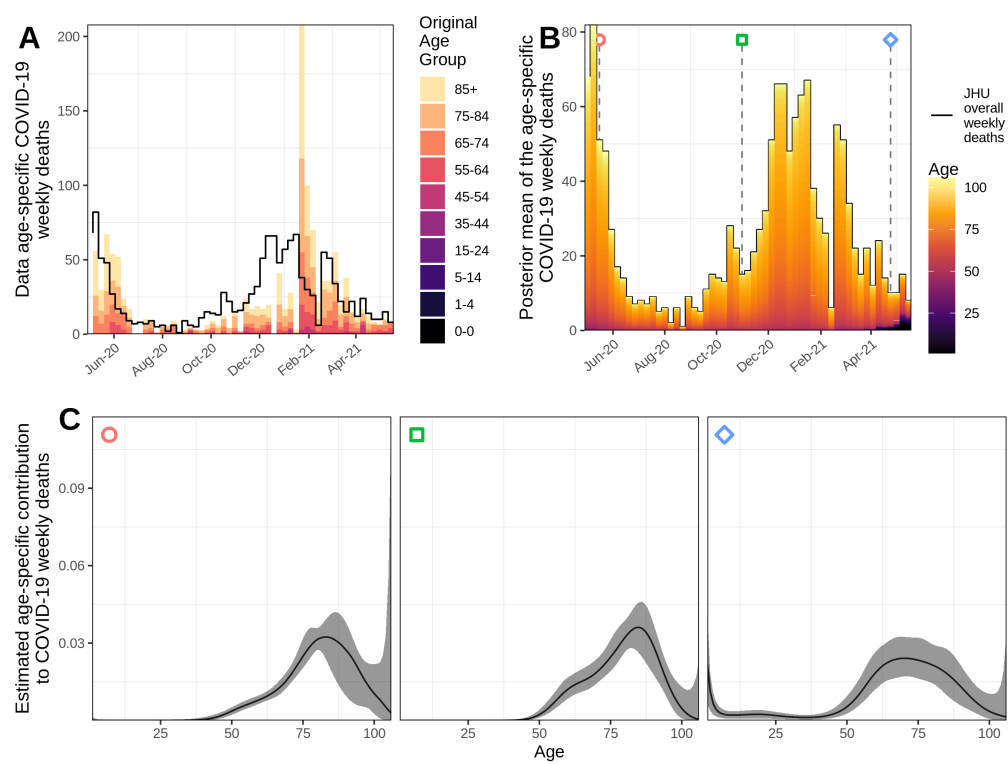


Figure S15: State summary for Delaware.



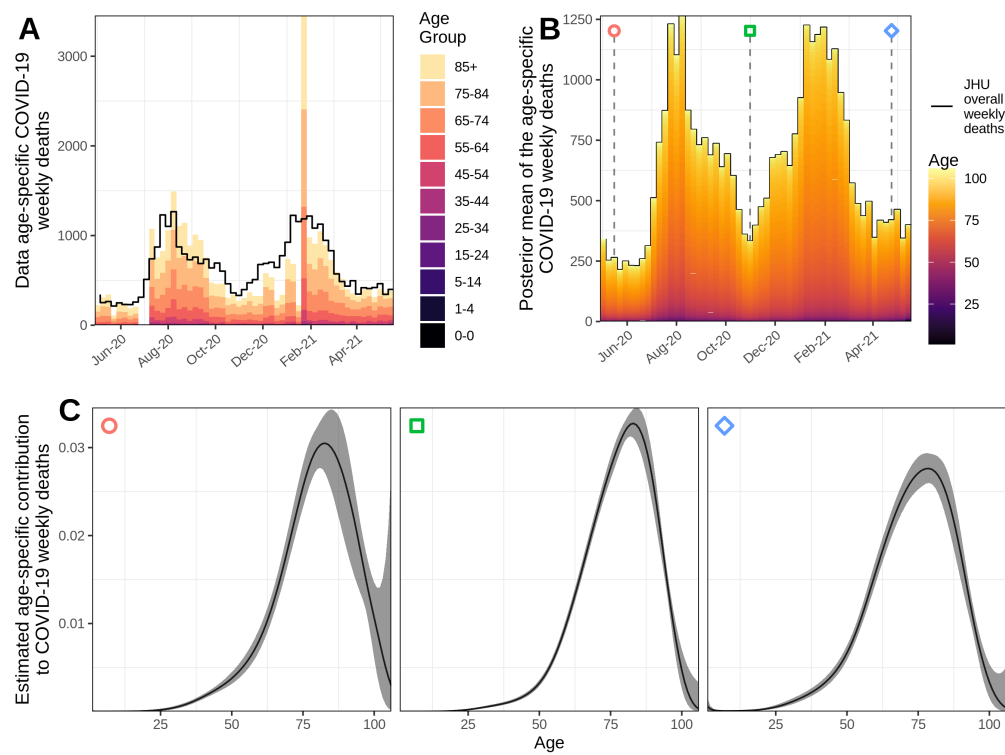


Figure S16: State summary for Florida.

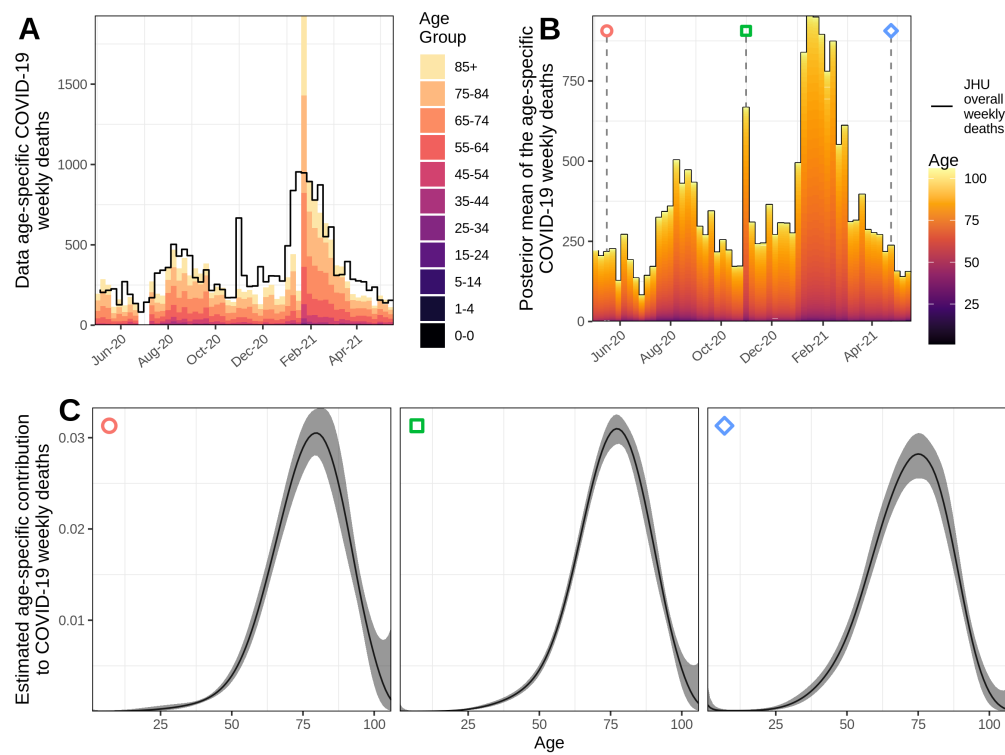


Figure S17: State summary for Georgia.

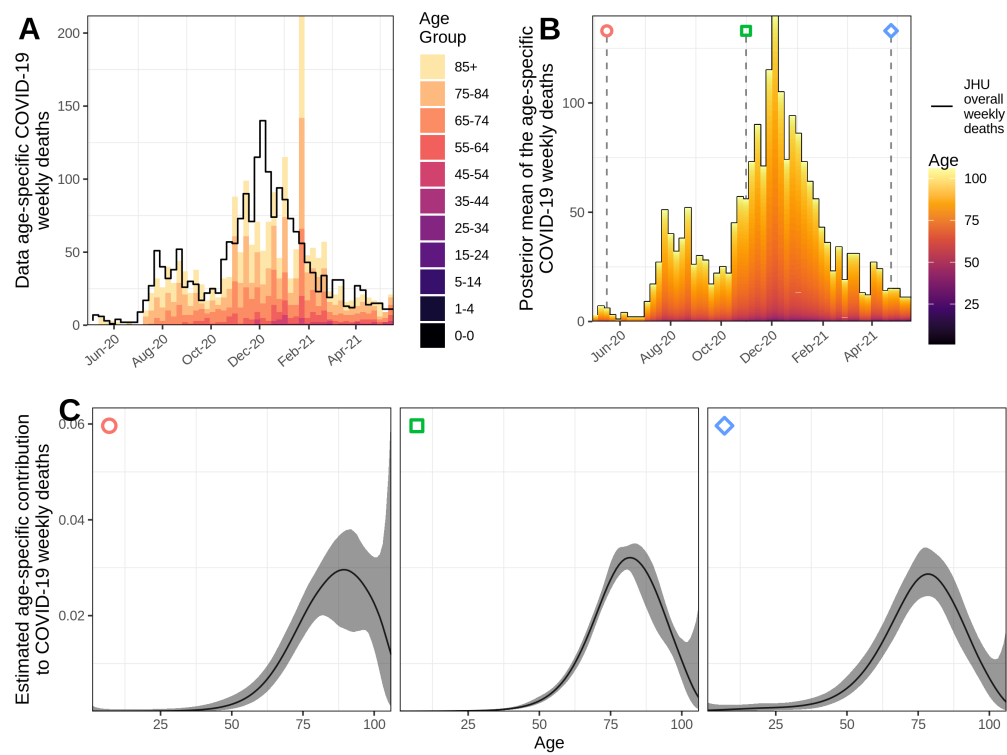


Figure S18: State summary for Idaho.

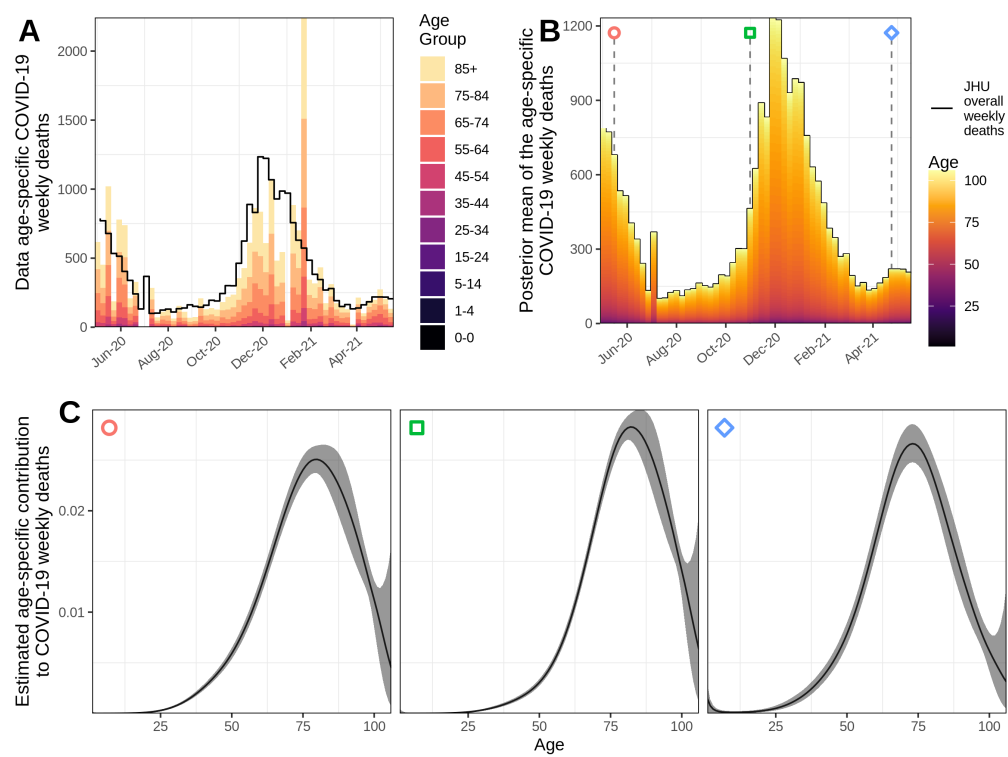
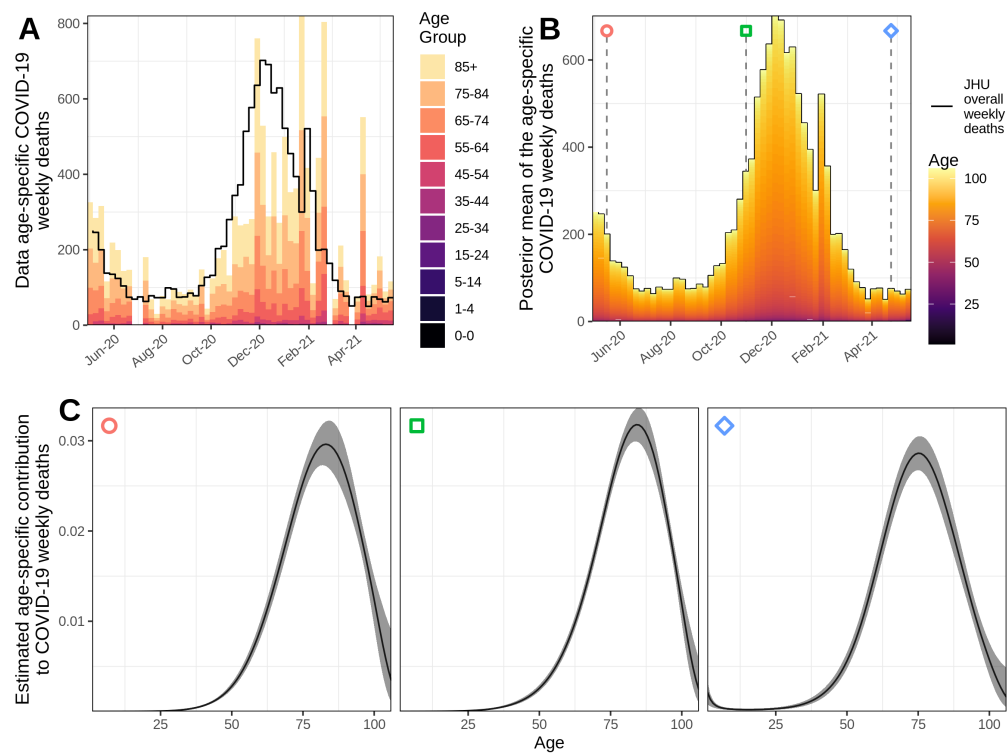


Figure S19: State summary for Illinois.

Figure S20: **State summary for Indiana.**

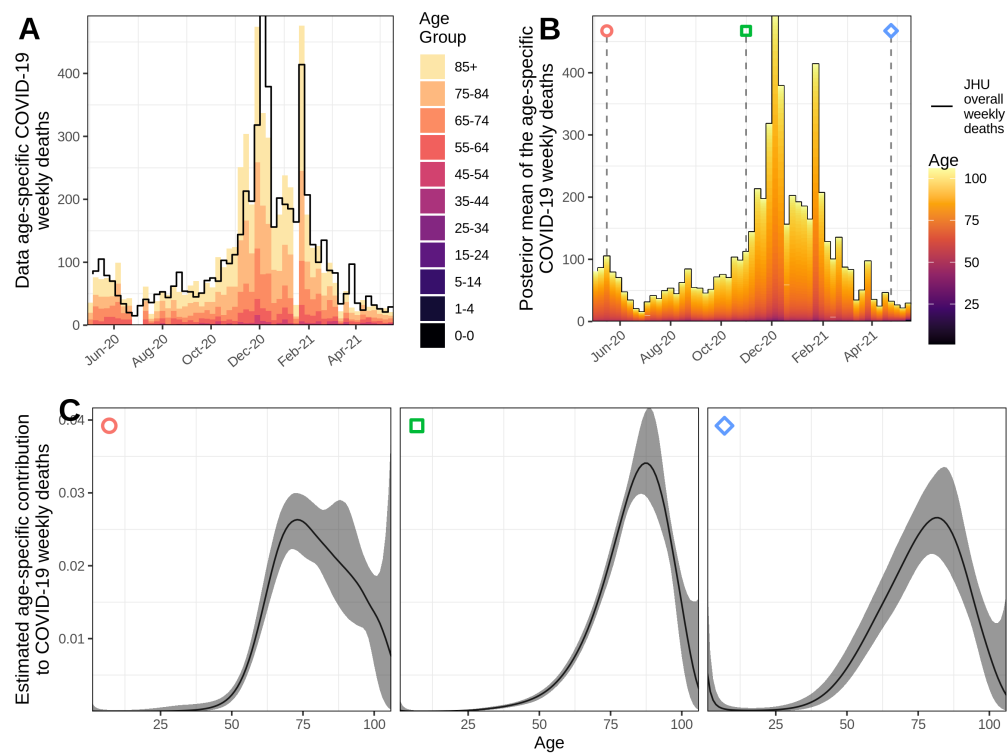


Figure S21: State summary for Iowa.

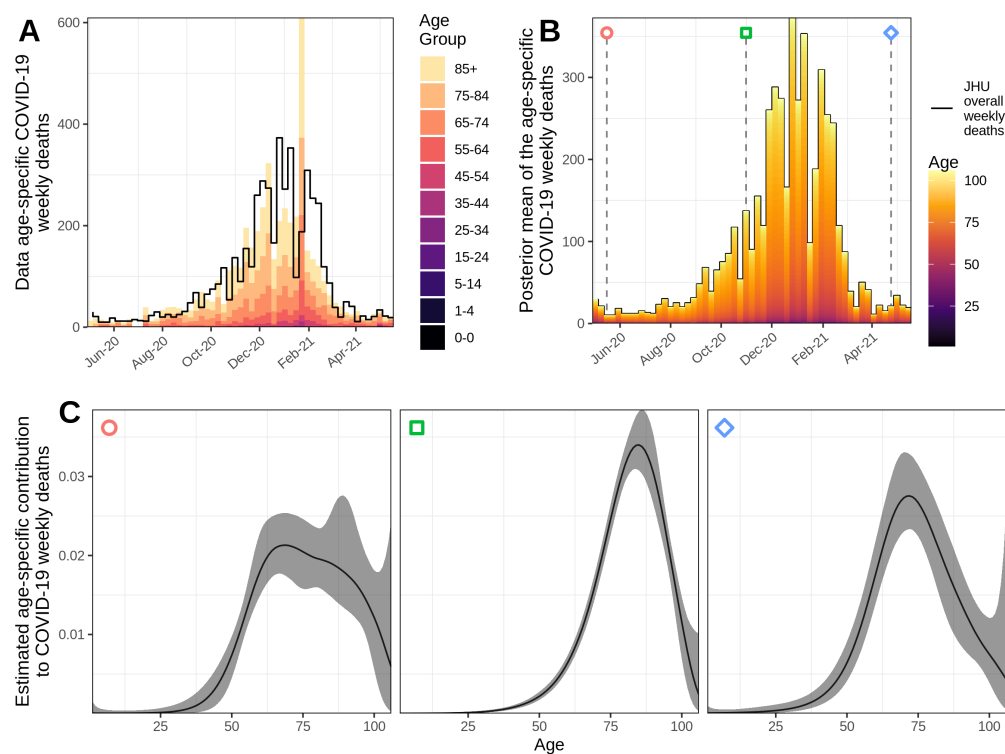


Figure S22: State summary for Kansas.



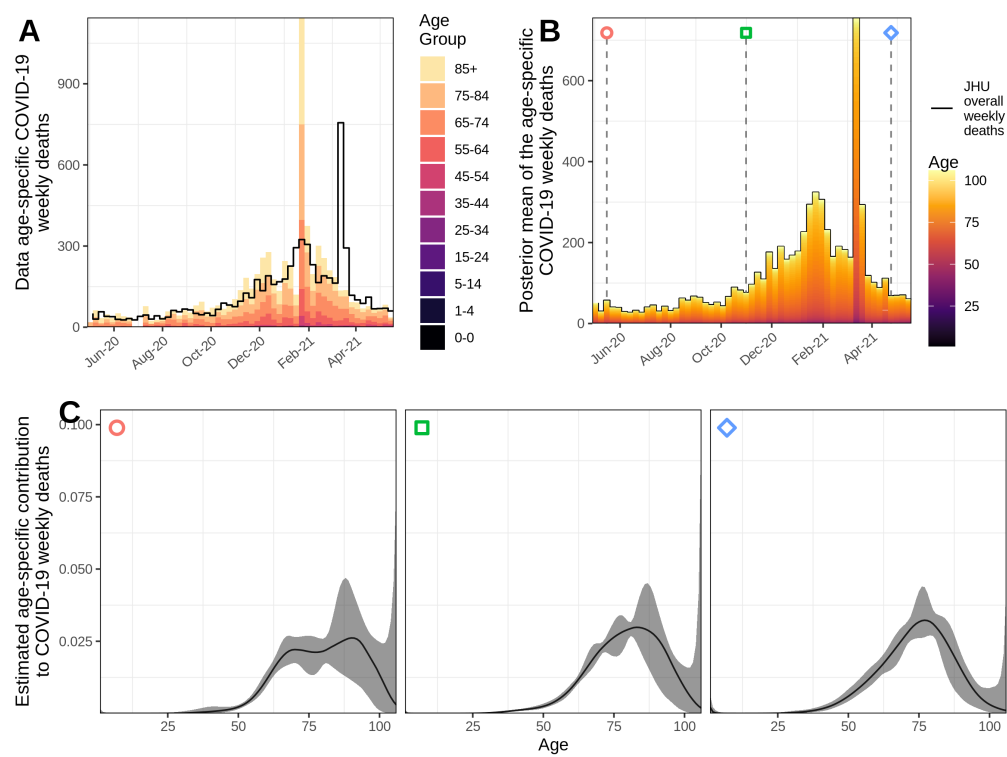


Figure S23: State summary for Kentucky.

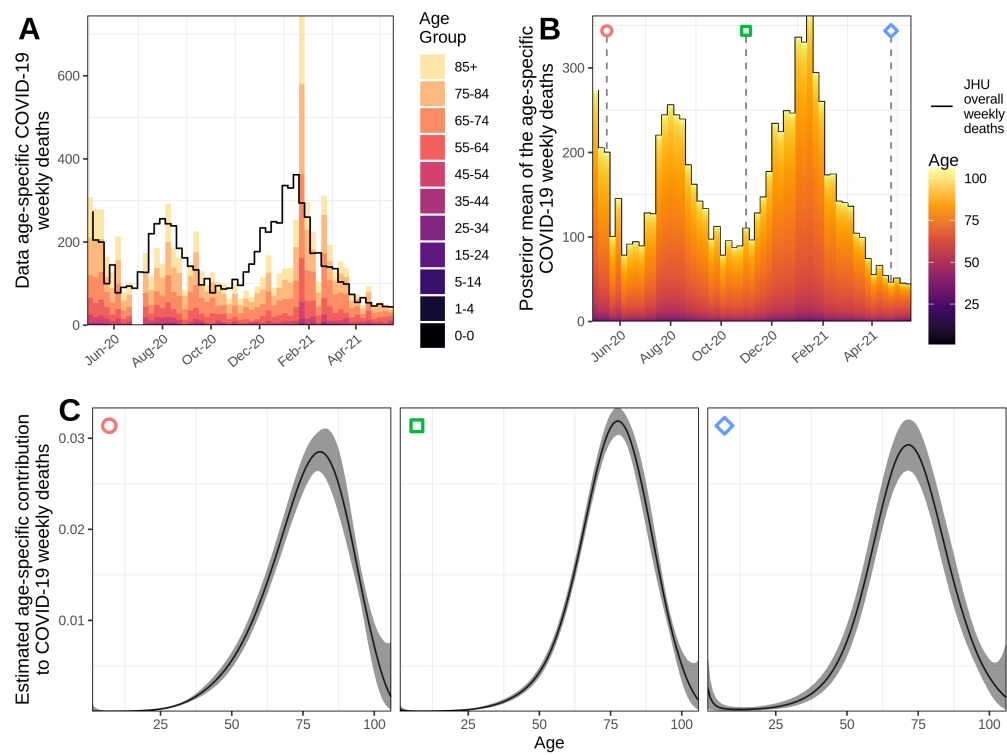


Figure S24: State summary for Louisiana.

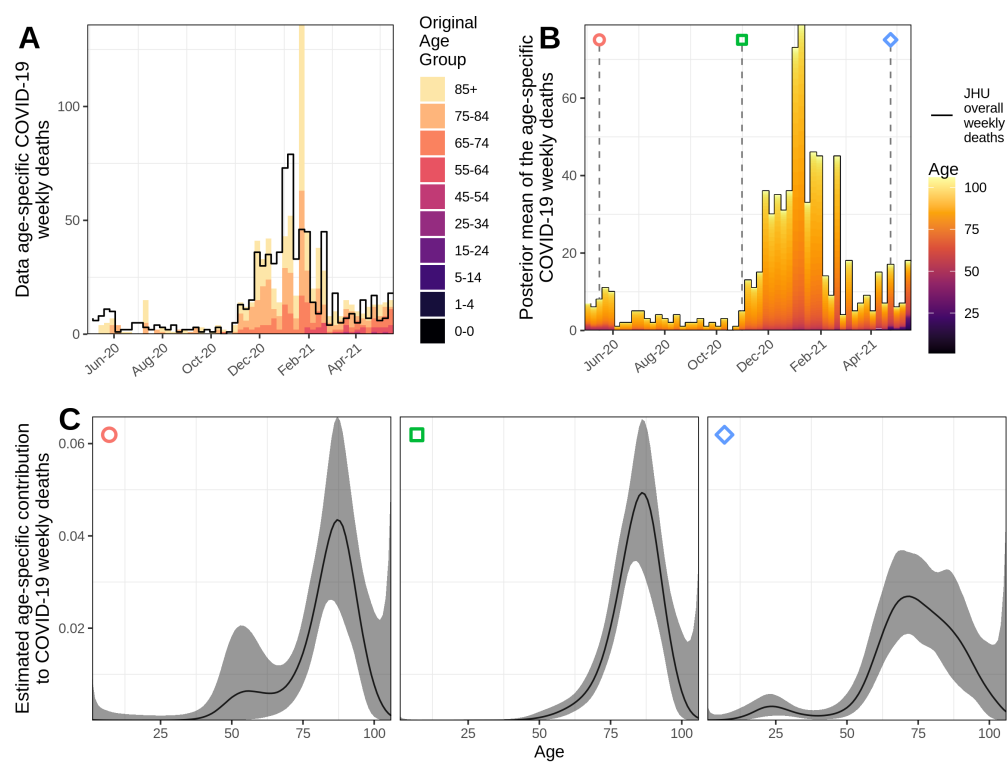


Figure S25: State summary for Maine.

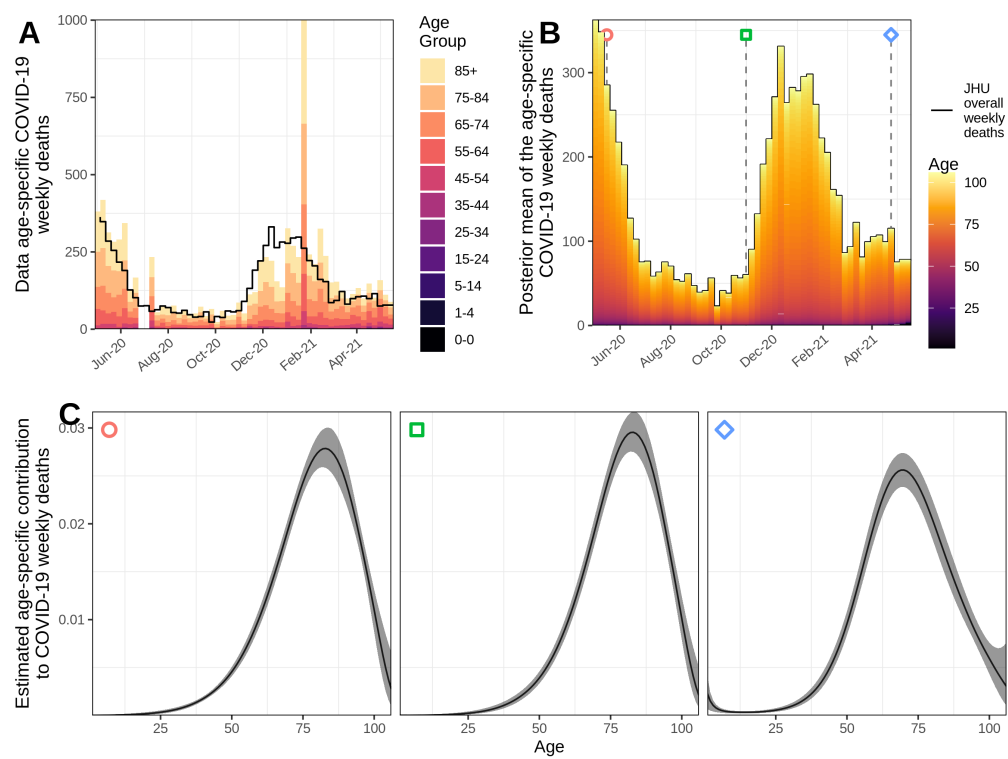


Figure S26: State summary for Maryland.

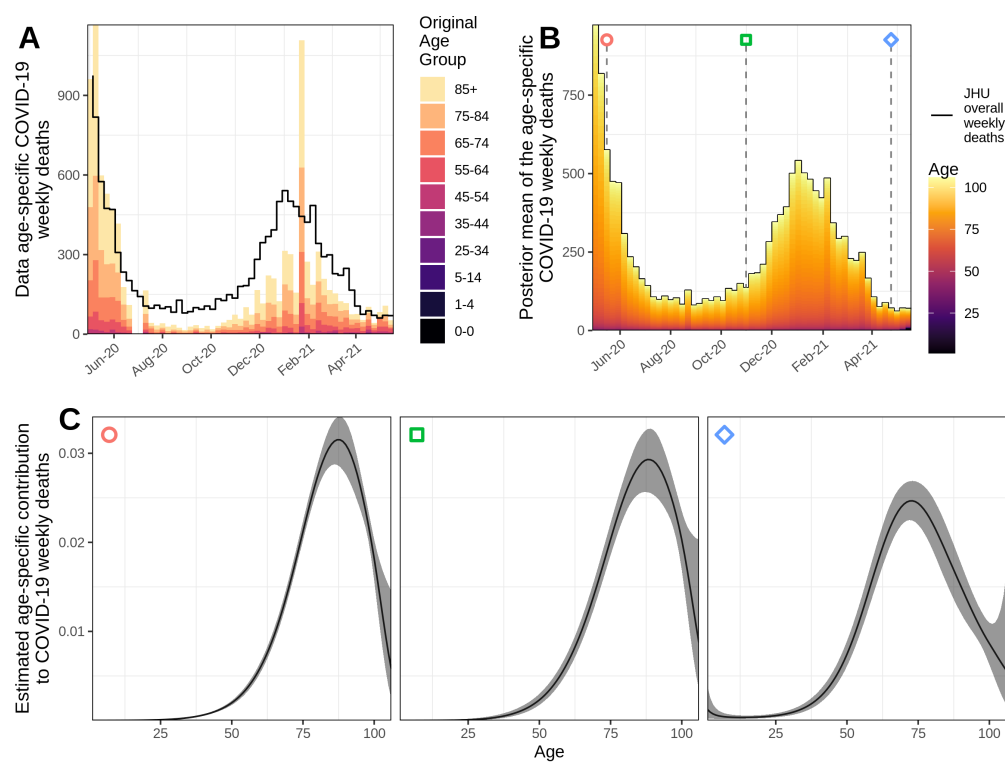


Figure S27: State summary for Massachusetts.

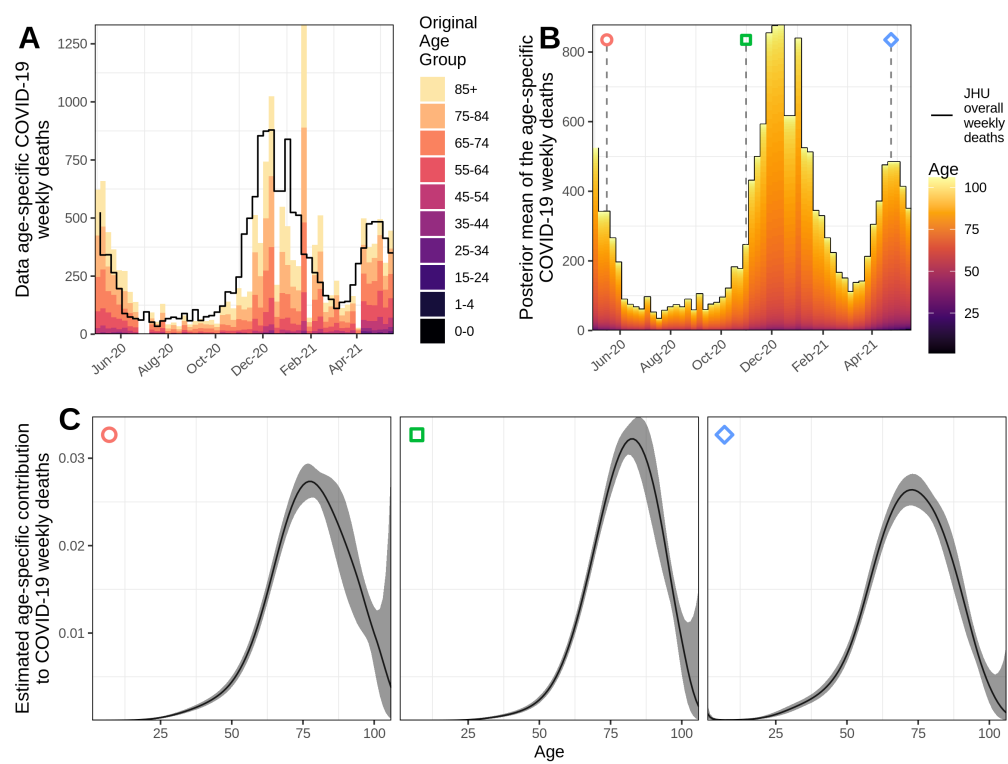


Figure S28: State summary for Michigan.

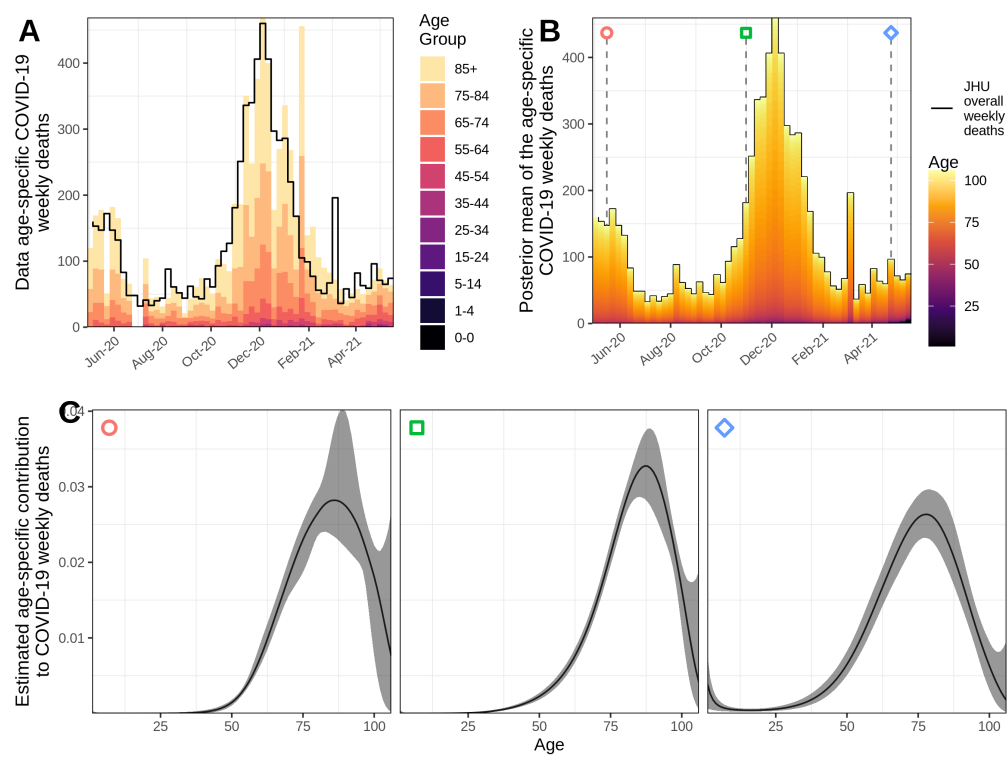


Figure S29: State summary for Minnesota.

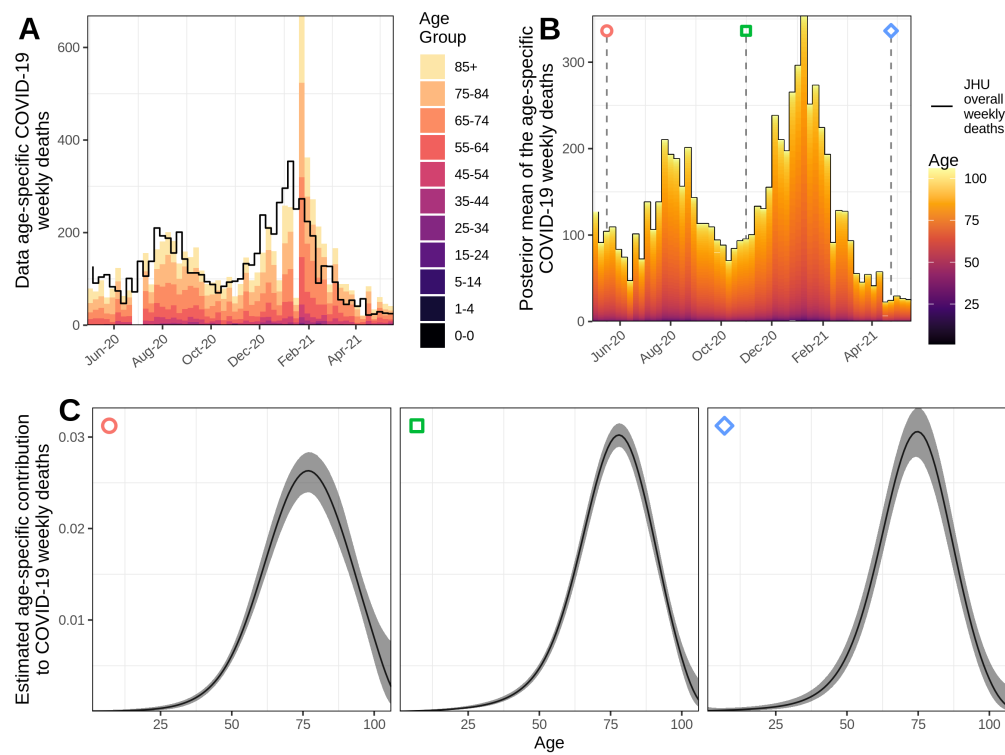


Figure S30: State summary for Mississippi.



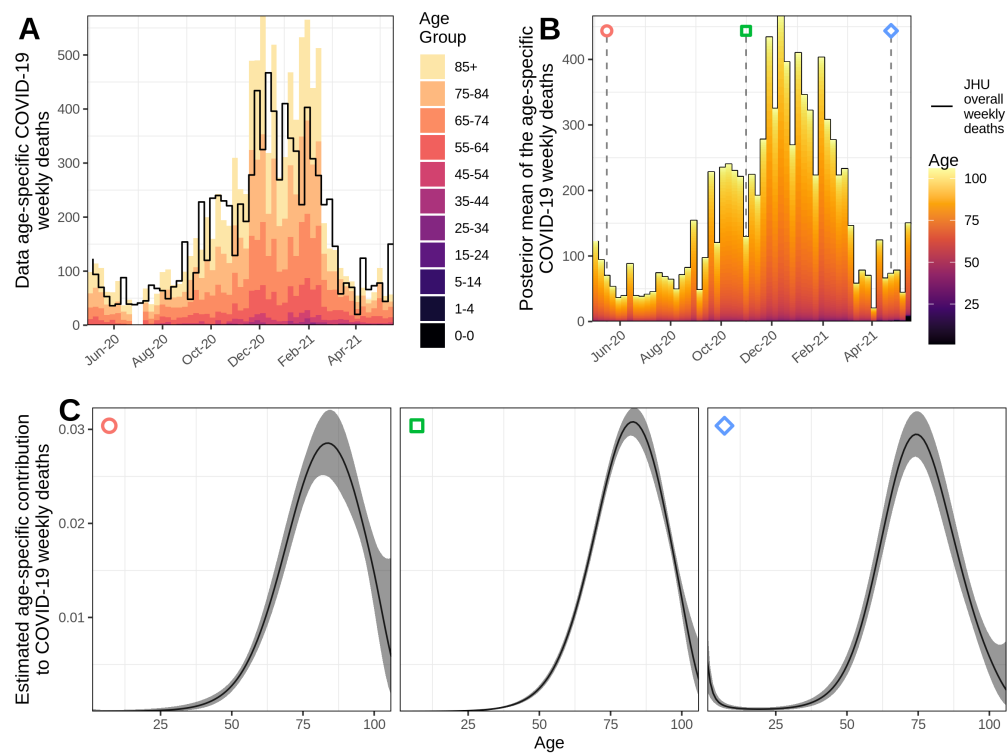


Figure S31: State summary for Missouri.

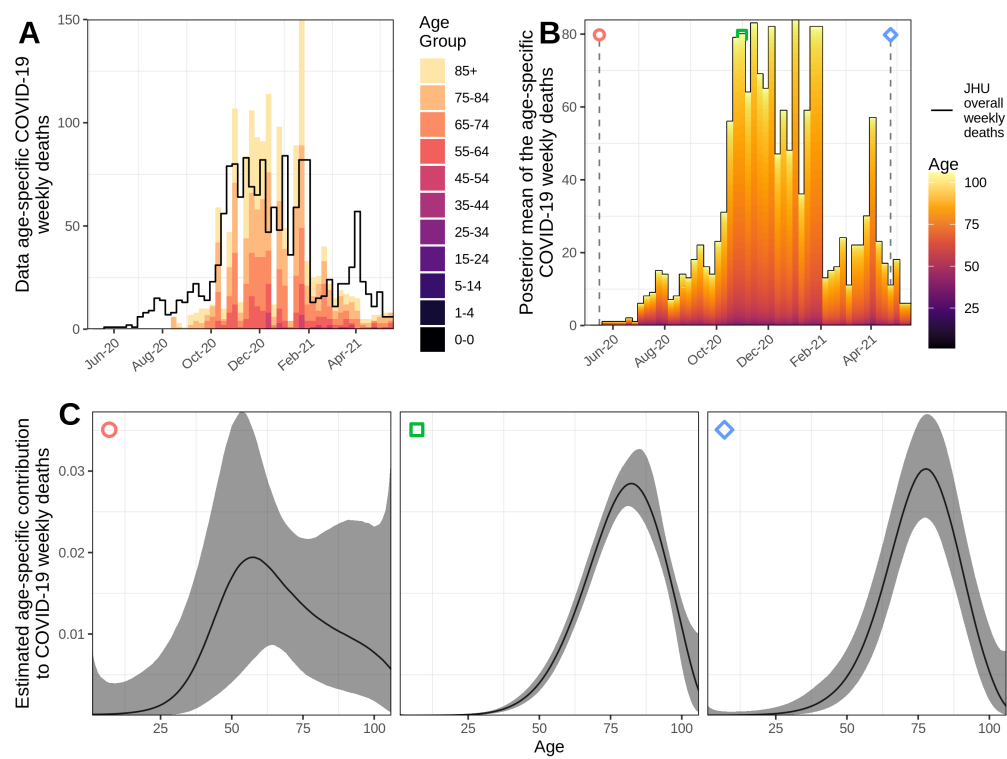


Figure S32: State summary for Montana.

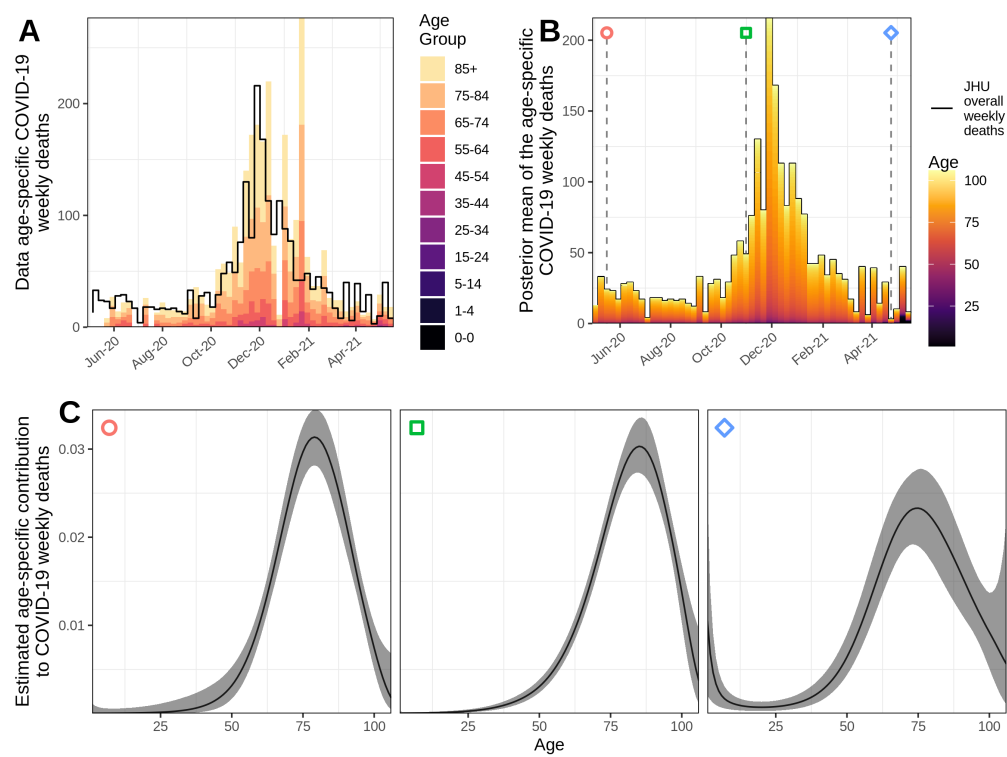


Figure S33: State summary for Nebraska.

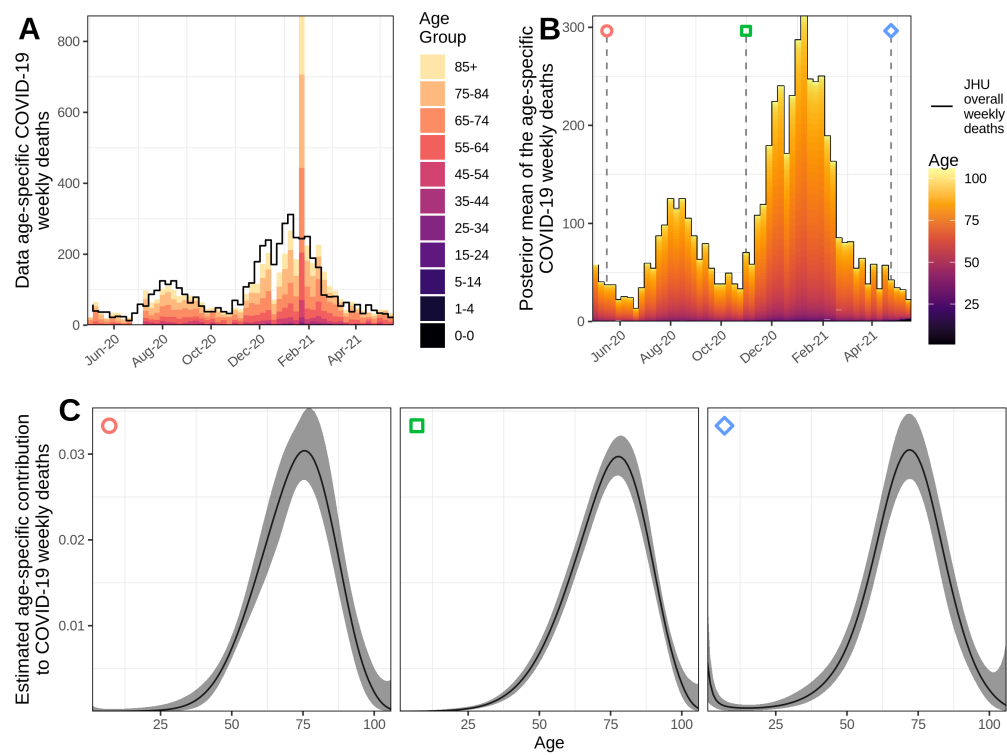


Figure S34: State summary for Nevada.

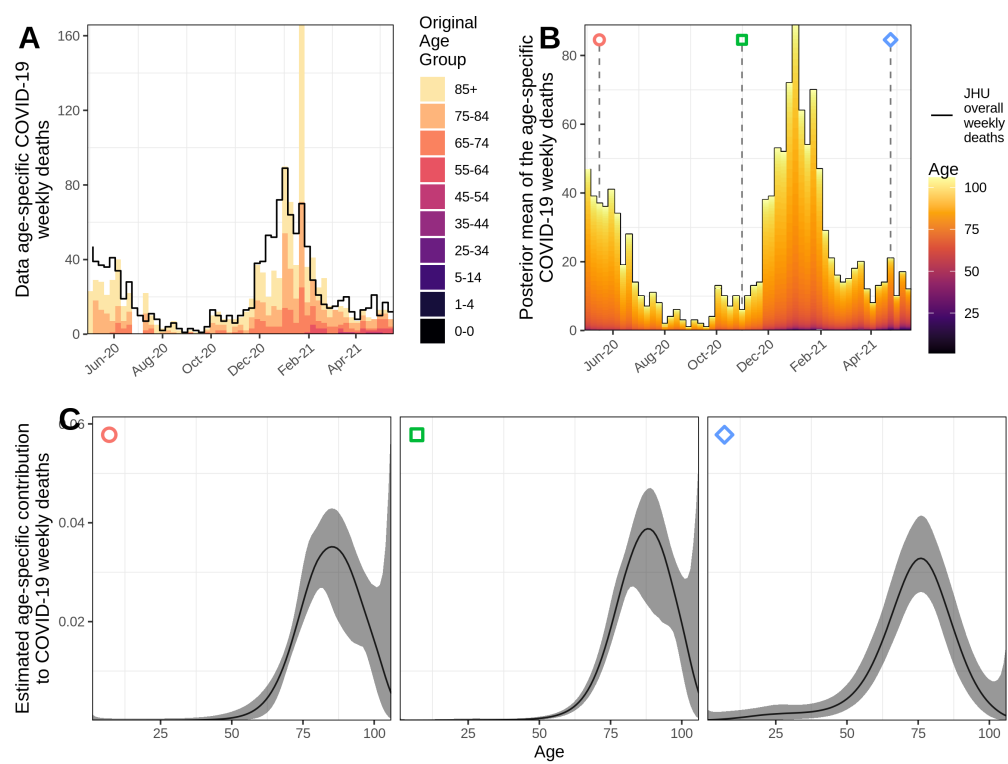


Figure S35: State summary for New Hampshire.

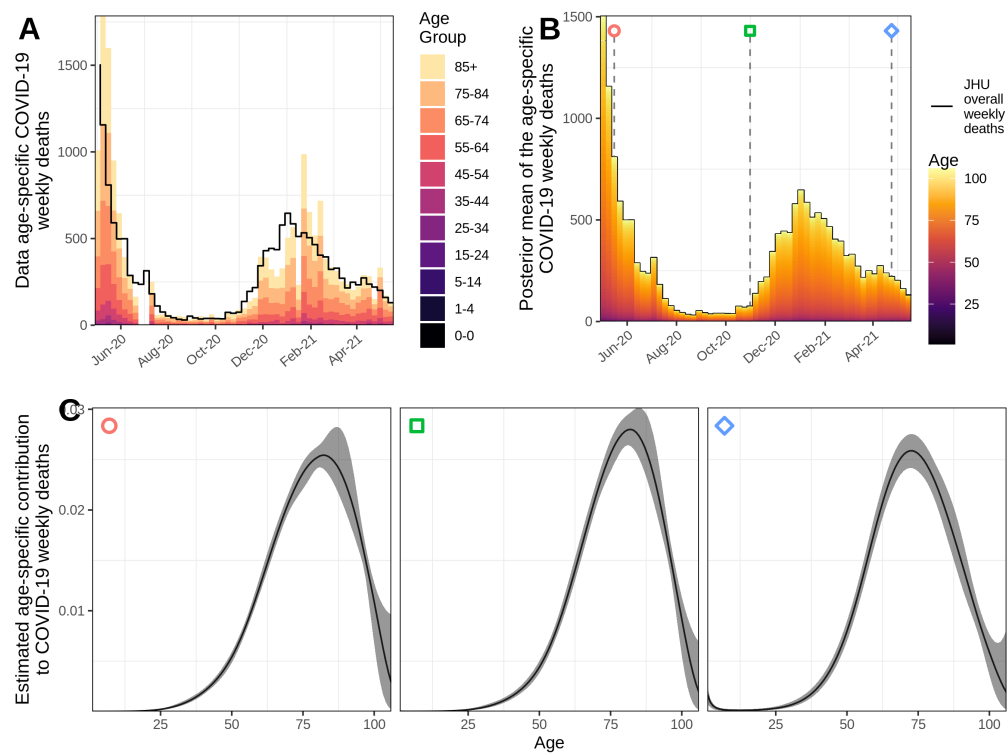
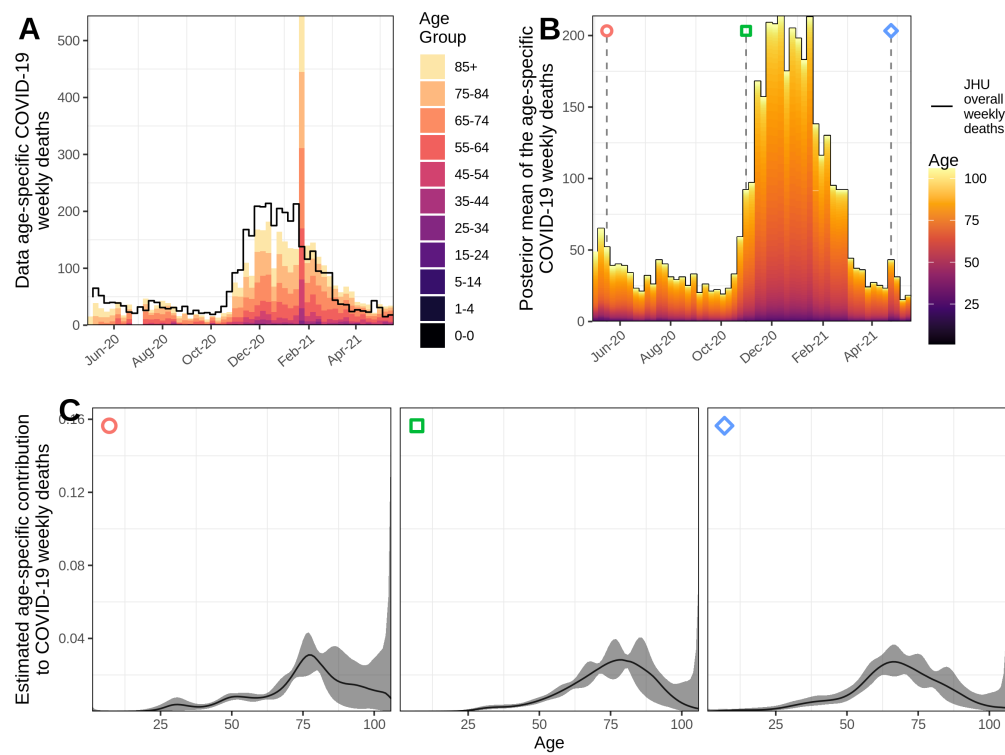


Figure S36: State summary for New Jersey.

Figure S37: **State summary for New Mexico.**

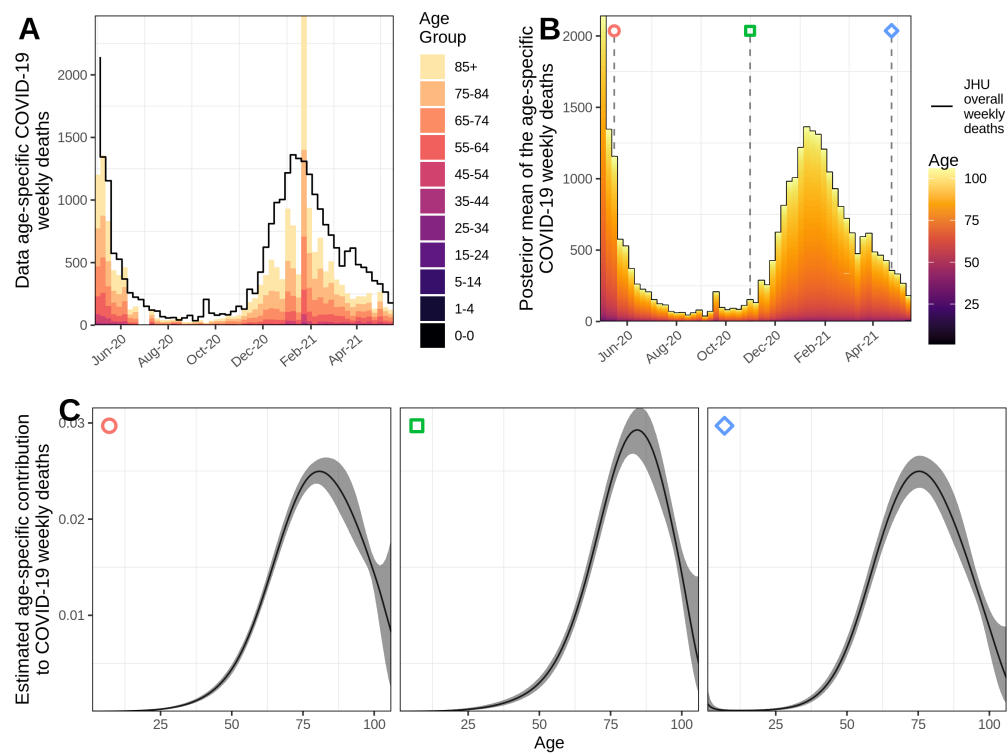


Figure S38: State summary for New York.



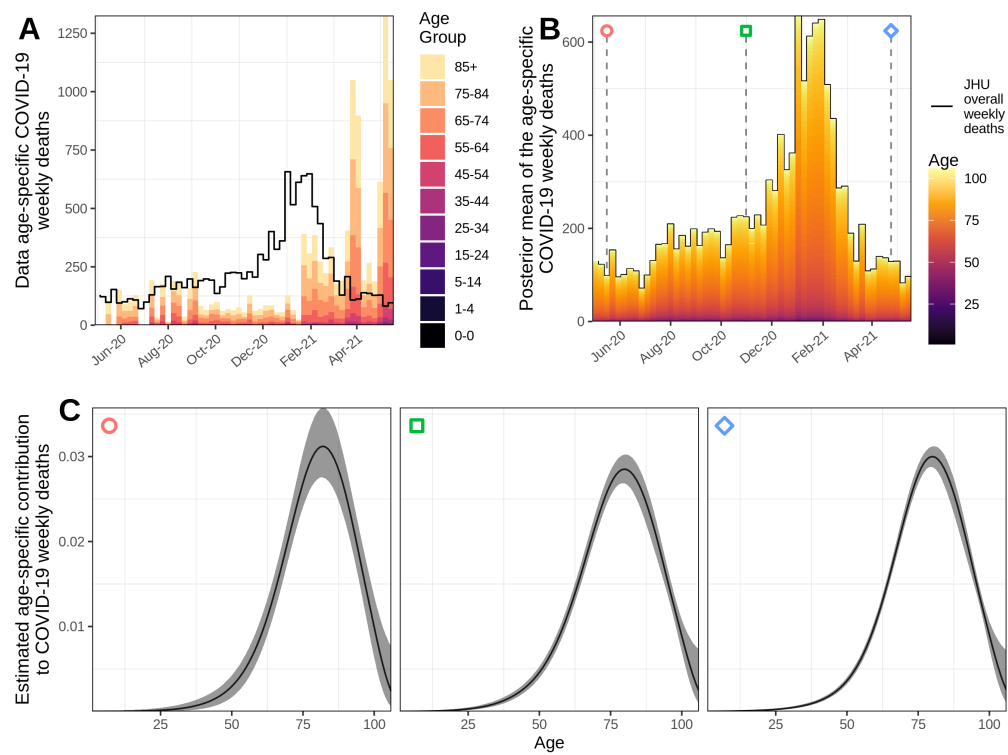


Figure S39: State summary for North Carolina.

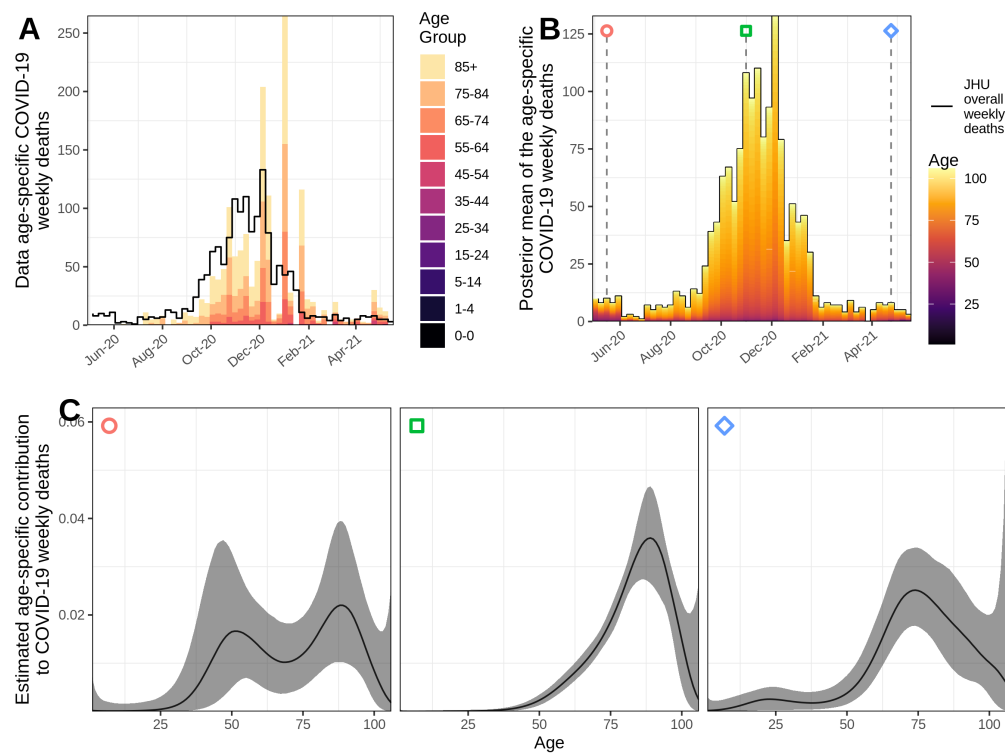


Figure S40: State summary for North Dakota.

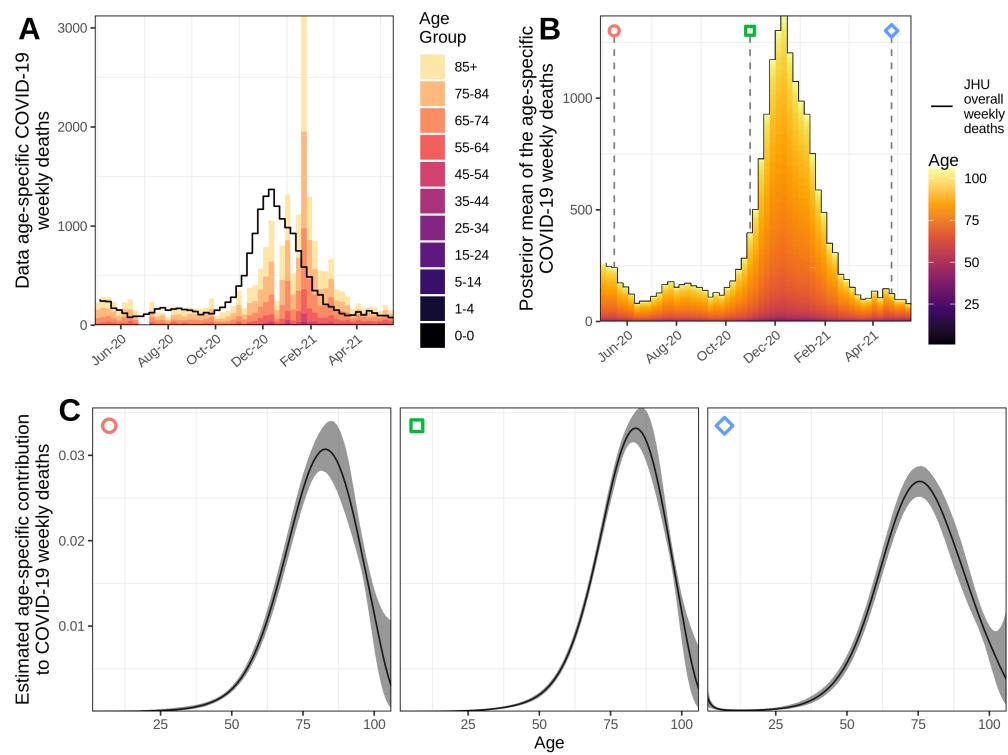


Figure S41: State summary for Ohio.

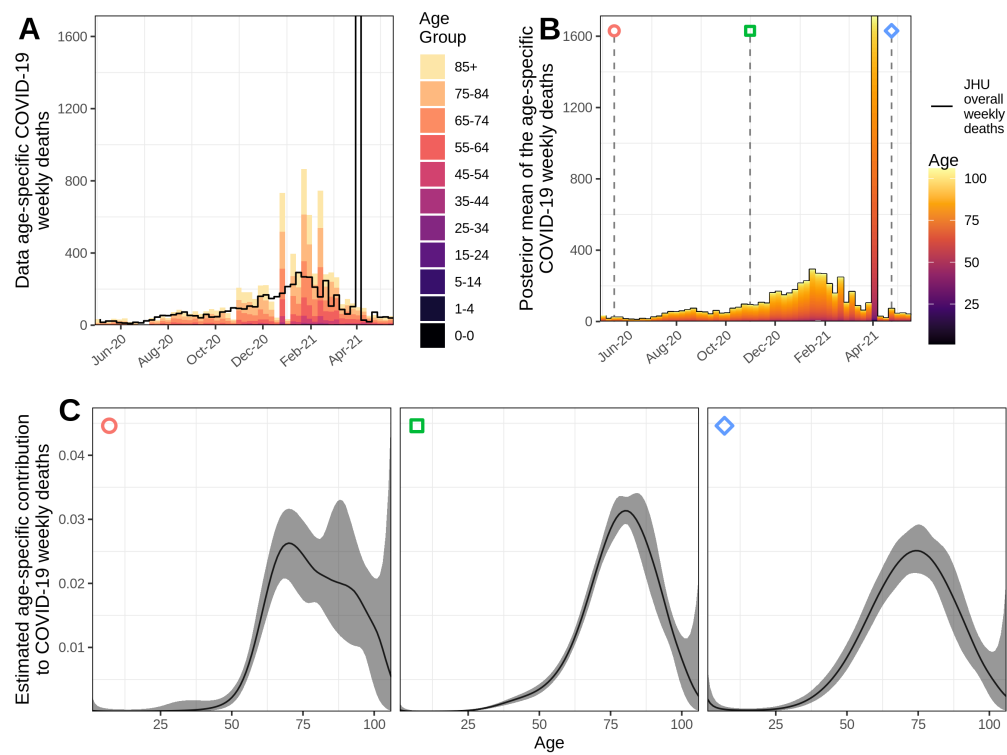


Figure S42: State summary for Oklahoma.

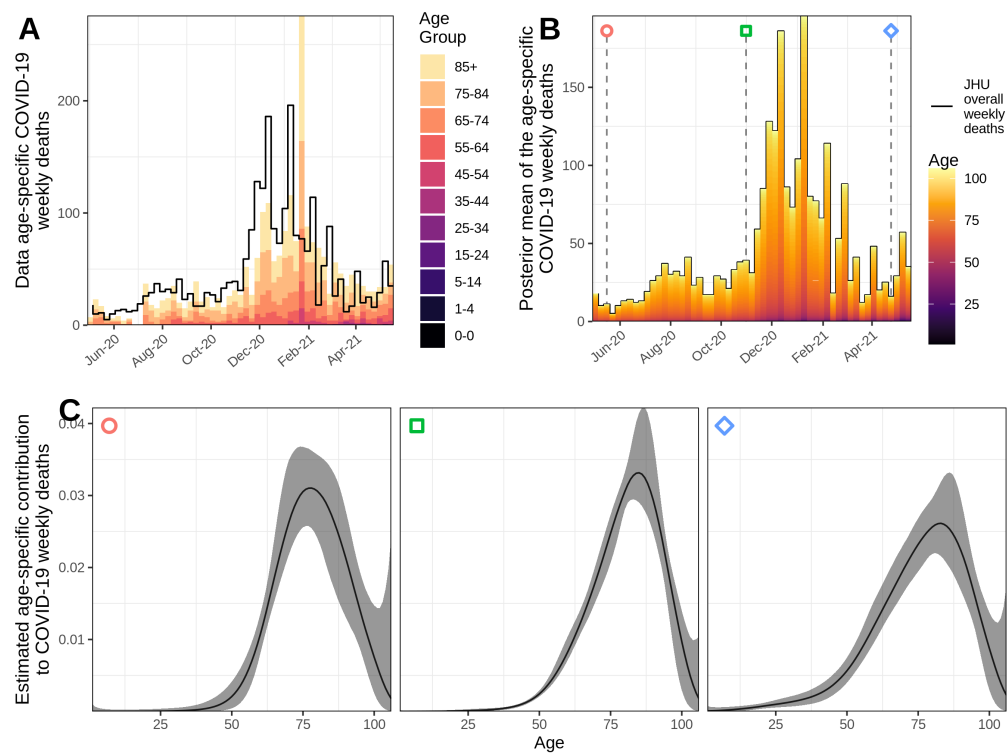


Figure S43: State summary for Oregon.

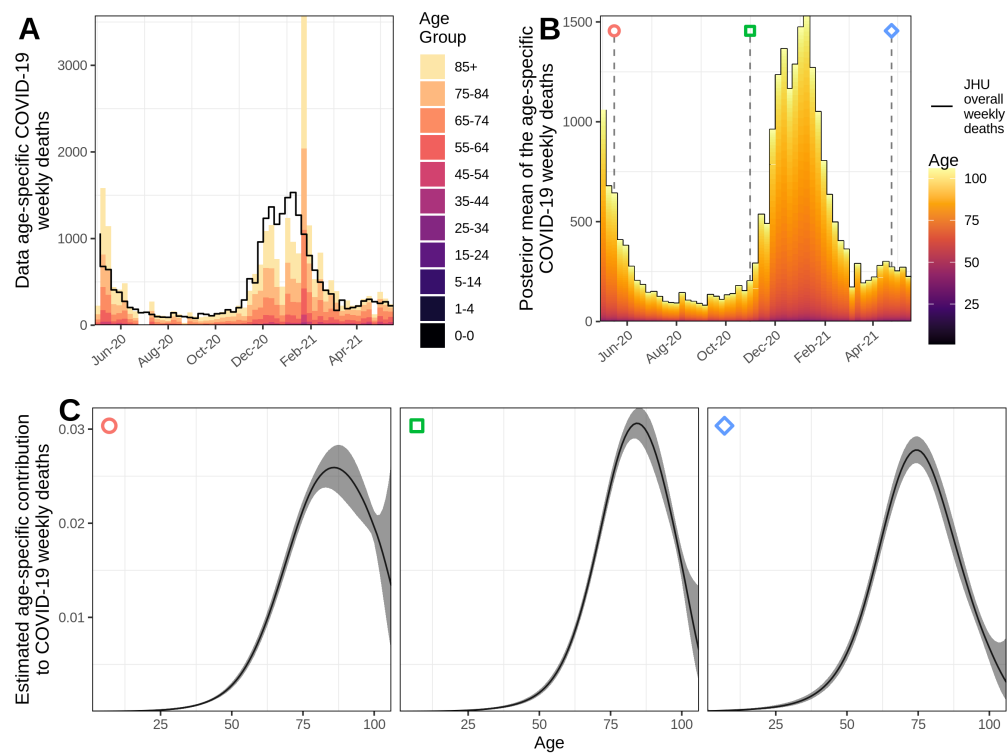


Figure S44: State summary for Pennsylvania.

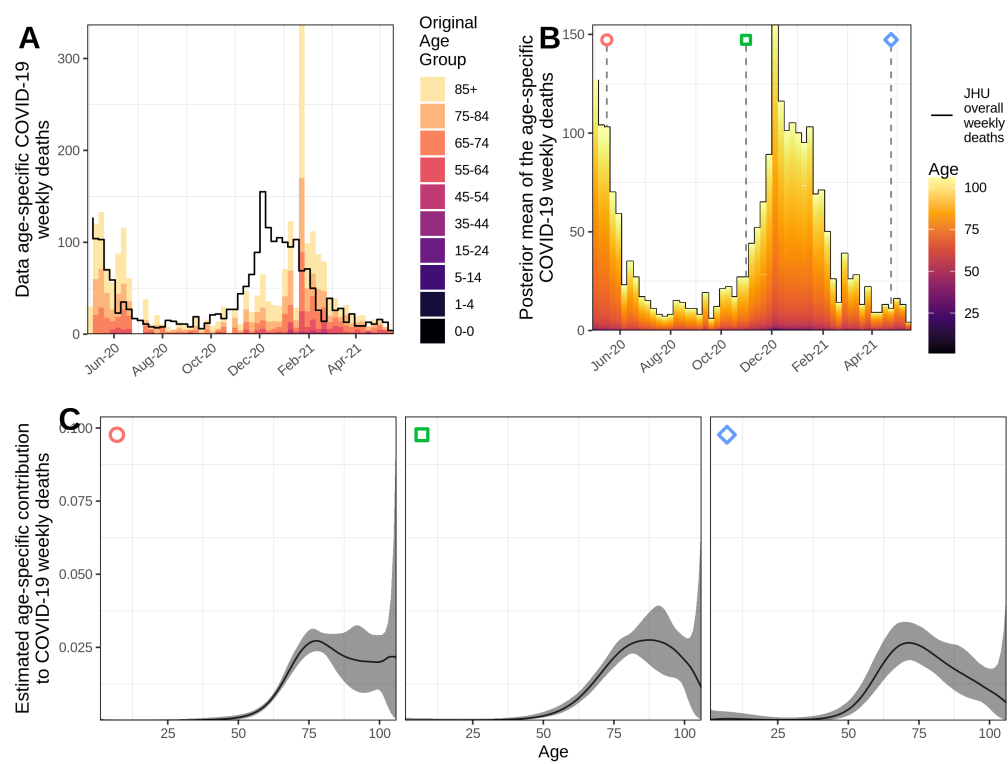


Figure S45: State summary for Rhode Island.

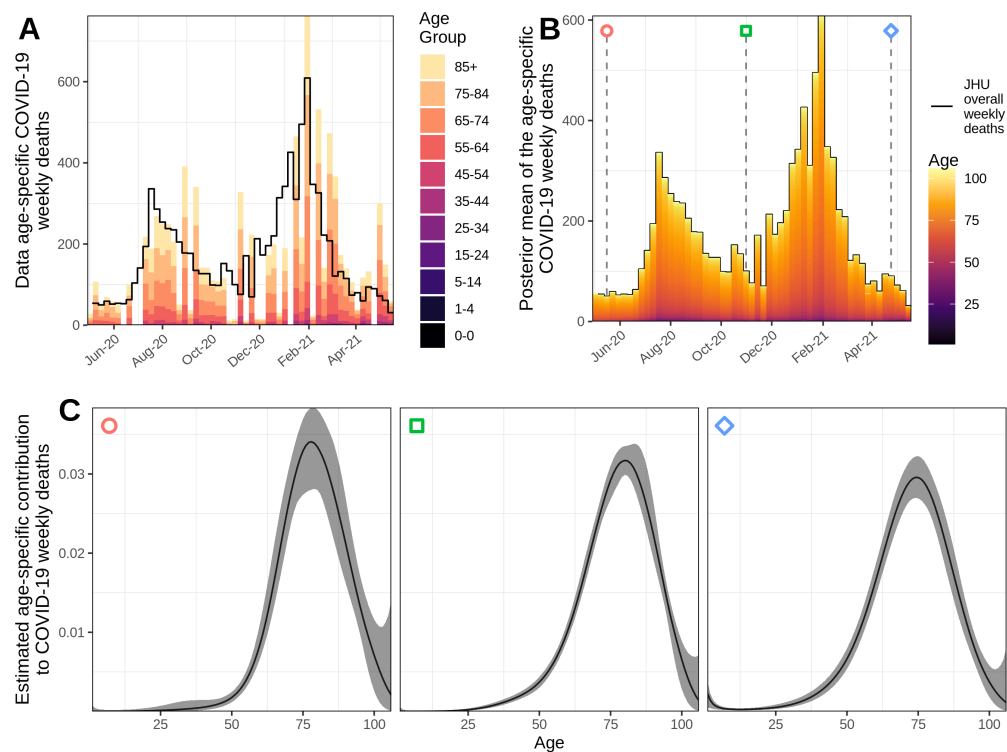


Figure S46: State summary for South Carolina.



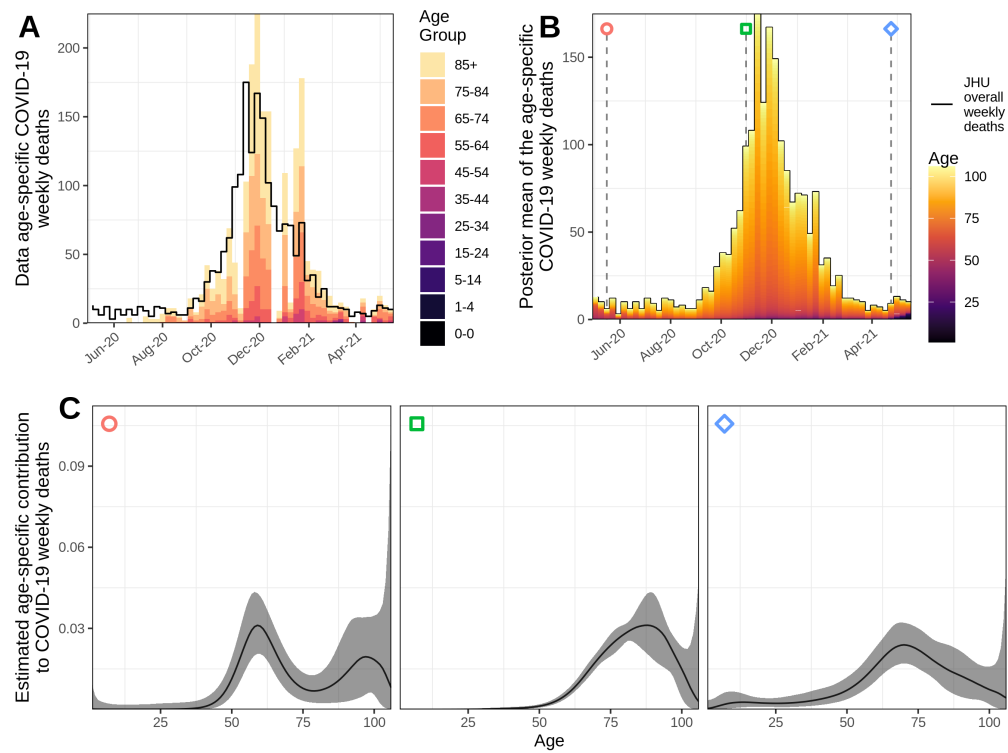
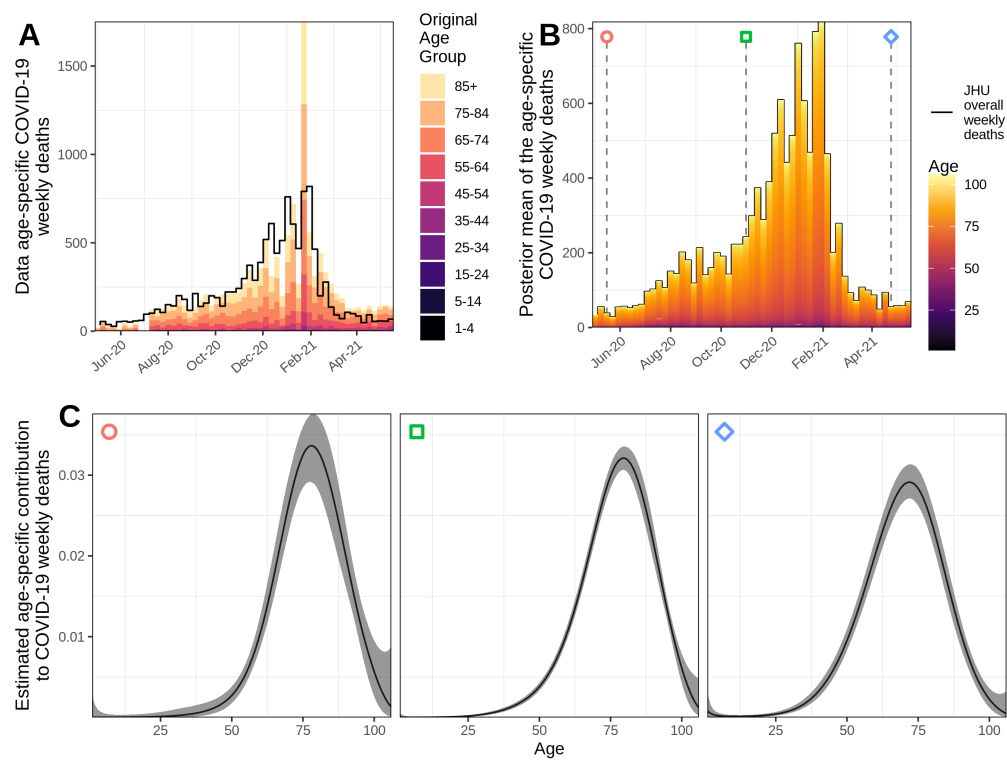


Figure S47: State summary for South Dakota.

Figure S48: **State summary for Tennessee.**

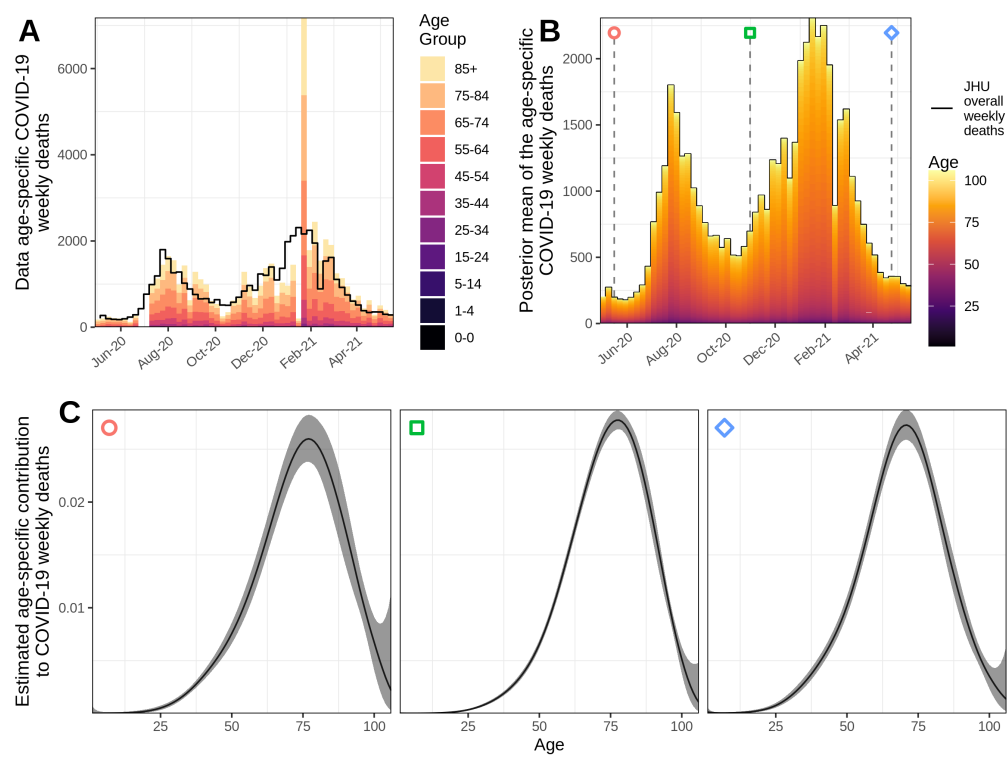


Figure S49: State summary for Texas.

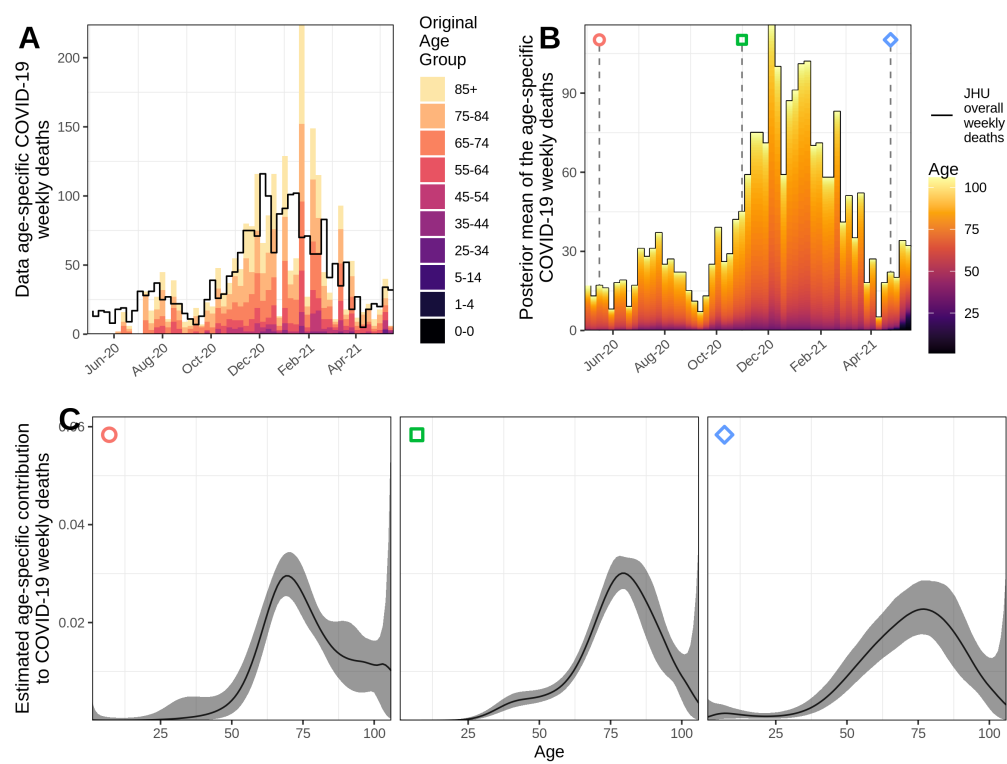


Figure S50: State summary for Utah.

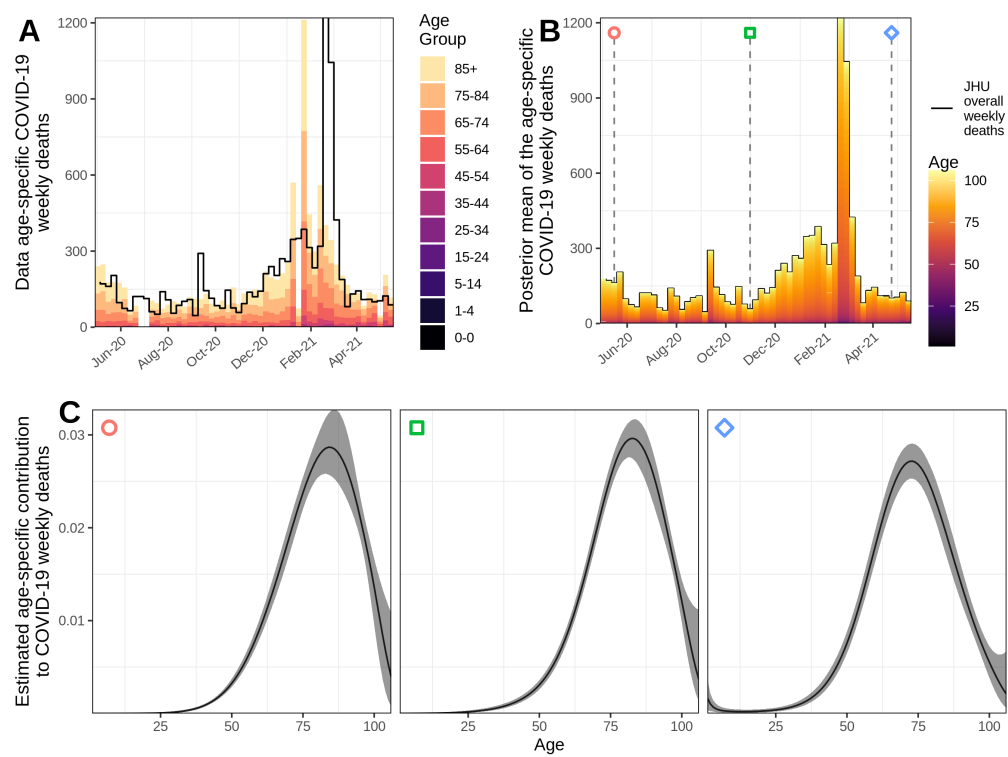


Figure S51: State summary for Virginia.

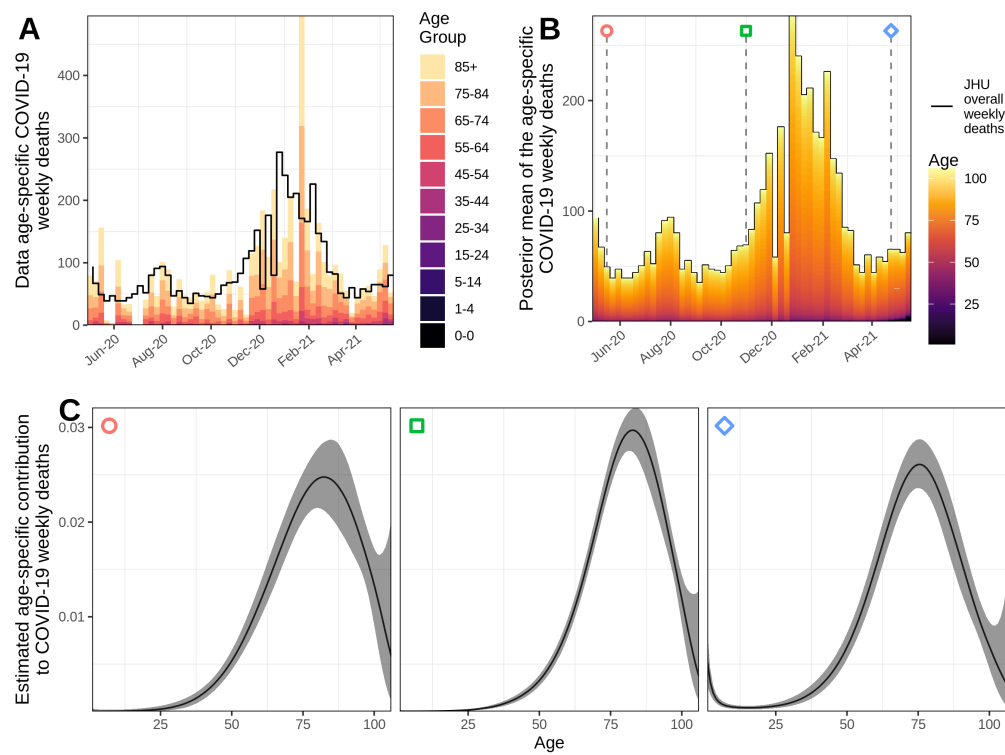


Figure S52: State summary for Washington.

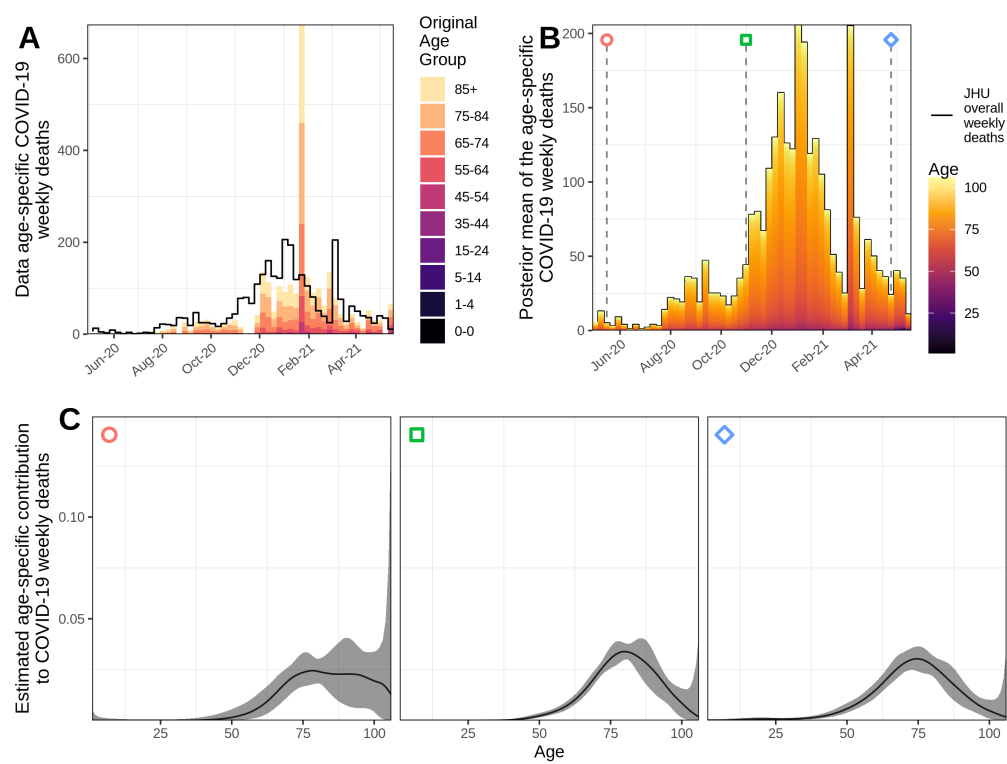


Figure S53: State summary for West Virginia.

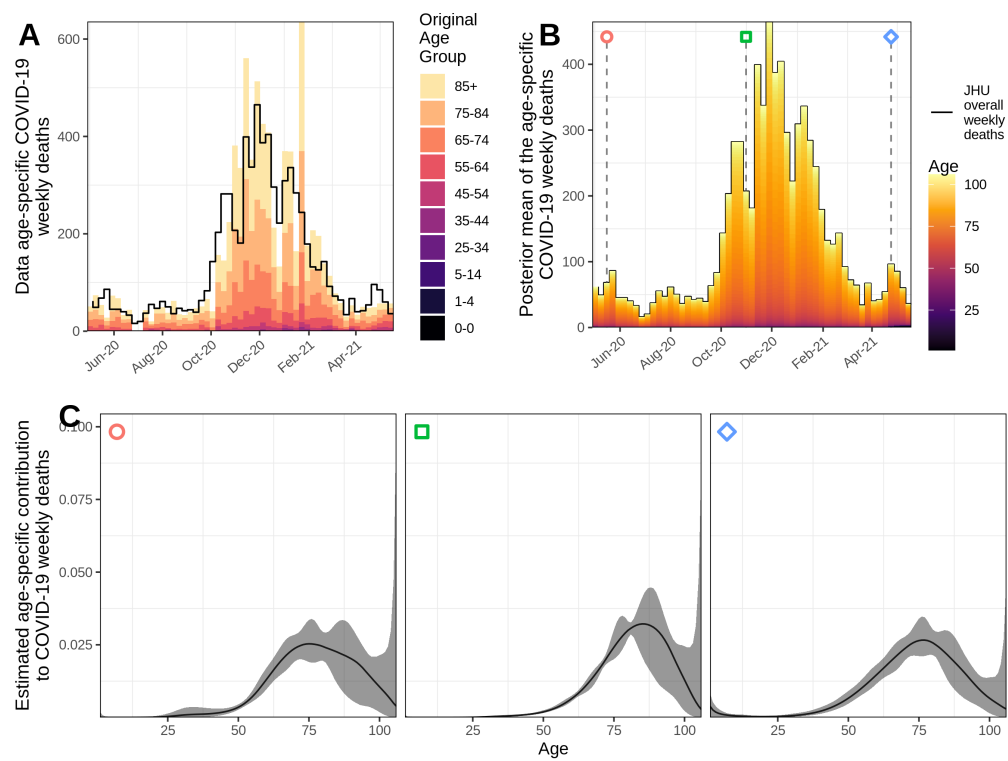


Figure S54: State summary for Wisconsin.